Université catholique de Louvain
Secteur des Sciences et Technologies
Institut de Recherche en Mathématique et Physique
Centre for Cosmology, Particle Physics and Phenomenology

CMS endcap tracker for the High-Luminosity LHC and search for Higgs pair production

Doctoral dissertation presented by

İzzeddin Suat Dönertaş

in fulfilment of the requirements for the degree of Doctor in Sciences

Thesis support committee

Dr. Nicolas Chanon	IP2I, France
Prof. Eduardo Cortina Gil (Secretary)	UCLouvain, Belgium
Prof. Christophe Delaere (Supervisor)	UCLouvain, Belgium
Prof. Fabio Maltoni (Chair)	UCLouvain, Belgium
Prof. Pascal Vanlaer	ULB, Belgium

September, 2023

Acknowledgements

I would like to start by expressing my gratitude to my supervisor, Christophe Delaere, for offering me the opportunity to work in such an amazing collaboration and always being there with his support and guidance throughout this work as well as the freedom I was given to define my path. It was a pleasure working with him.

Besides my advisor, I thank the rest of my thesis committee: Nicolas Chanon, Eduardo Cortina Gil, Fabio Maltoni, and Pascal Vanlaer for their comments and suggestions that definitely improved this thesis.

Canım ailem, bu tezi özellikle sizlere armağan ediyorum. Akademik kariyerimin her anında yanımda olduğunuz ve doktora sürecim boyunca da bu desteği eksik etmediğiniz için, bana sonsuz güven ve sevgi duyduğunuz için minnettarım. Annecim, babacım, Gizem, Şevket, ve canım yeğenim Deniz, bu tez sizin.

My brother, my forever best friend, Levi, I simply cannot thank you enough. You are the reason my physics journey started, you are the reason I got into the best physics department in the country and most of all, you are the reason for who I am today. I am extremely grateful for all the advice, brainstorming, fights, and discussions we had over these four years (and all that came before). I am thankful I have such a great brother.

My friends, who made my life abroad much more fun and much more belonging, I am grateful for the support and love I got from you. The down moments of doing a PhD were definitely much more bearable with you in my life. I cherish a lot of moments from these past four years where I was put back on my feet and I could keep going thanks to you people: Kerem, Aysu, Felix, Gizem, Özge, Sarah, and many others.

I next would like to thank my friends and colleagues at CP3. To Khawla, for being there as my peer, listening to my problems with attention and putting in the effort to get them resolved. To Sandhya, for being a friend and a colleague at the same time with such ease that it was a pleasure being office mates with her. To all other colleagues & friends I made at CP3, Marina, Rafael, Hesham, Ishan, Florian and many others, thank you all for your friendship and company throughout these past years.

Contents

Introduction

> “If we knew what it was we were doing, it would not be called research, would it?"
>
> — Albert Einstein

Seeking to find out about the universe and understand glimpses of its vast chaos is the most humane temptation. It is this urge that captivated the philosophers of the ancient Greece, likewise Galileo, and equally much Einstein and Planck. This human endeavour lasting since 650 BC - 480 BC have formed the scientific method, gave birth to a broad range of scientific fields all competing in a race to provide better understanding of the world around us.

Particle physics, having emerged from nuclear physics, aims to provide the most comprehensive understanding of fundamental particles and the laws & forces governing their interactions. Immense efforts by generations of physicists in the last century has brought forward the formulation that we now call the Standard Model of Particle Physics (SM) which serves as the Bible of the field. The model has been extremely successful in providing predictions and validated through extensive experiments in the last half-century. It, however, is falling short in providing answers for some missing pieces in our understanding of fundamental particles & interactions; one of the four fundamental interactions, gravity, is missing in the SM as well as an explanation for matter-antimatter asymmetry and dark matter. This is pushing the high energy community to look for and work on theories Beyond the Standard Model (BSM), proposing an explanation for new physics. The SM’s biggest success in predicting physics would be, without a doubt, the discovery of the Higgs boson in 2012 thanks to the most powerful accelerator ever built; the Large Hadron Collider (LHC). With Higgs discovered, the SM is now complete which does not mean that the exploration of this new boson is over -it’s the contrary.

The property and precision measurements of Higgs allows for characterization of its scalar potential that it assumes around its vacuum expectation value as the shape of this potential is defined by the self-coupling parameter λ. After measuring the Higgs mass, the value for λ was predicted but its measurement is still an ongoing effort. The most straightforward way to access this parameter experimentally is observing a Higgs pair (HH). This phenomenon, however, is manifesting at extremely rare rates at our current collisions. Namely, it’s thousand times more rare than observing a single Higgs. Therefore, a major upgrade was designed to maximize the physics reach of the LHC for the second half of its lifetime that would lead to an increase in luminosity by a factor of ten, compared to its original design value, called the High Luminosity LHC (HL-LHC) Upgrade.

This upgrade implies major installations for the experiments located at the LHC, including the Compact Muon Solenoid (CMS), to keep up with the increased rate of collisions in two fronts: the ability to maintain current efficiency and the ability to filter through interesting phenomena. The upgrade of the CMS detector, mainly of the strip tracker's, is the focus of this dissertation as the author was involved in all aspects of this upgrade effort. These efforts include commissioning a new cleanroom and developing a control system, making the services design with prototyping and validating, and developing quality assurance procedures and tests. This work lead to an internal engineering design report.

The second half of this dissertation reports on yet another upgrade effort, a prospective analysis searching for a Higgs pair in two channels: $WW\gamma\gamma$ and $\tau\tau\gamma\gamma$, in an attempt to prove the physics reach of the proposed upgrade. This search, documented also as an internal analysis note, was published as a physics analysis summary and was included in the White Paper summarizing physics expectations on a range of frontiers within the proposed upgrade.

This dissertation is devoted to the HL-LHC upgrade, describing the upgrade studies on detector level and outlining the expected performance. Chapter 1 will give a brief introduction to the SM while highlighting the Higgs mechanism and the Higgs pair production. Chapter 2 will overview the experimental apparatus starting with the LHC and moving on with a focus on the CMS detector which will be followed by a separate chapter on the current silicon tracker (chapter 3). Chapter 4 will summarize the implications of HL-LHC upgrade on the CMS detector, once again with a focus on its tracker system. The author's contribution in all fronts of the upgrade will be outlined in Chapter 5. The final chapter (chapter 6) will describe the prospective HH analysis.

Chapter

1. The Standard Model of particle physics

This chapter will give an overview of The Standard Model (SM) of particle physics, our current best understanding of the fundamental particles and their interactions, whose validity has been well established in the last half-century by extensive scientific programmes carried out worldwide.

We will start by describing the particle content of SM, followed by the Lagrangian density describing the interactions of the particles, and the Higgs mechanism and the electroweak symmetry breaking. A fourth section will describe the double Higgs production in the SM as it is the focus of the analysis reported in this work. Lastly, a review of open questions in the SM will be presented.

The idea that matter consisted of indivisible units leads back 2500 years to ancient Greece, to Democritus and Leucippus of Abdera. The proposition that all of matter is made of atoms, or $\alpha\tau o\mu o\sigma$ ("uncuttable" in Greek), came from them and survived through centuries growing into different scientific subjects. Particle physics however can be considered as the subdiscipline that pushes the atomic idea as far as possible.

What is known as the Standard Model of particle physics is the model that presently encompasses all of our empirical knowledge about the field of particle physics, or also referred as high energy physics (HEP). It is the study of the nature at the most reductionist level as it occupies itself with the ultimate building units of matter and the laws governing their interactions. Simply put, it emerged from two basic observations about our world:

1. Things exist, i.e., there is matter,
2. Things happen, i.e., interactions occur.

SM is a particular kind of quantum theory, a quantum field theory (QFT) that combines quantum mechanics and special relativity into a unified whole, that suggests a particular particle content along with a particular symmetry group. Its theory content will not be described at length, instead, its particle content and formalism governing the interactions between them will be summarized. The review in the following sections is based on Ref. [1], [2], and [3].

1.1. Fundamental particles and forces

Little more than 100 years ago, early 20th century, our understanding of the structure of the atom was far from well understood; the electron had been recently discovered with no comprehensive understanding of its properties and behavior, and theoretical frameworks such as quantum mechanics and special relativity were still unknown. However, fast forward to the end of the century, our current *tableau* of elementary particles were already formed following decades of discoveries.

As it stands, all matter around us is made up of particles called fermions which are spin-$\frac{1}{2}$ particles of two kinds: *quarks* and *leptons*. The distinction between these two subgroups of fermions is made such that the quarks are fermions with fractional electric charge while the leptons are fermions with neutral or integer electric charge. Integer spin particles called *gauge bosons* mediate the fundamental interactions between fermions. What is referred here as interaction is interchangebly used with the term force. As far as we know, four fundamental forces govern the universe around us: *the strong force*, *the weak force*, *the electromagnetic force*, and *gravity*. Standing today as the well established non-gravitational interactions, SM still does not account for gravity in its current formulation.

The strong force is described by the theory of quantum chromodynamics (QCD) and it acts on quarks binding them together and forming the nucleus and it is mediated by the *gluons*. The elecromagnetic and the weak forces are manifestations of one unified force called the electroweak (EW) force where the electromagnetic force is mediated between charged particles by the *photon* and the weak force is responsible for the β-decay of the nuclei, mediated by the W and Z bosons. Table 1.1 presents a summary of the forces and their mediators.

Table 1.1. List of fundamental interactions and their associated boson mediators in the SM, their masses and what they act on. The mass values are taken from Ref. [4]. The gluons, photon and graviton are supposed massless and the experimental upper limit is quoted between parentheses.

Interactions	Gravitational	Electromagnetic	Weak		Strong
Mediator particle	Graviton	Photon (γ)	W± bosons	Z boson	Gluons (g)
Mediator mass	$0\ (<6\times10^{-32}\,\mathrm{eV})$	$0\ (<1\times10^{-18}\,\mathrm{eV})$	80.4 GeV	91.2 GeV	$0\ (<1.3\,\mathrm{MeV})$
Acts on	Mass-energy	Electric charge	Flavour charge		Colour charge

Fermions are categorized under three generations of particles with two members in each generation. For the quarks, each generation consists of two quarks of electric charge $\frac{2}{3}$ and $-\frac{1}{3}$. Under the strong force, quarks manifest another charge called the colour charge that comes in three states: "red", "blue", and "green". Quarks bind together via strong force to form either a quark-antiquark pair, a meson, or a three-quark object, a baryon, which are all color-neutral particles. These three generations of quarks correspond to six flavours of quarks: up (u), down (d), charm (c), strange (s), top (t), and bottom (b). In the same convention, there exists three generations of leptons with two members in each generation: one with an electric charge of -1 and another with no electric charge. This corresponds to electron (e) and electron neutrino (ν_e), muon (μ) and muon neutrino (ν_μ), and tau (τ) and tau neutrino (ν_τ) which dont carry any colour charge. Table 1.2 presents a summary of fermions.

Table 1.2. List of fermions in the SM with their masses and charges, split per generation. The exact mass values and neutrino upper limits are taken from the particle data group [4].

Generation	Leptons			Quarks		
	Flavour	Mass	Electric charge	Flavour	Mass	Electric charge
First	electron neutrino (ν_e)	<1.1 eV	0	up (u)	$2.16^{+0.49}_{-0.26}$ MeV	$+2/3$
	electron (e)	511 keV	-1	down (d)	$4.67^{+0.48}_{-0.17}$ MeV	$-1/3$
Second	muon neutrino (ν_μ)	<0.19 MeV	0	charm (c)	1.27 ± 0.02 MeV	$+2/3$
	muon (μ)	106 MeV	-1	strange (s)	93^{+1}_{-5} MeV	$-1/3$
Third	tau neutrino (ν_τ)	<18.2 MeV	0	top (t)	172.9(4) GeV	$+2/3$
	tau (τ)	1.78 GeV	-1	bottom (b)	$4.18^{+0.03}_{-0.02}$ GeV	$-1/3$

Fermions are classified as right-handed singlets when the direction of their spin is the same as the direction of their motion and left-handed doublets if these two directions are opposite. The weak force has been shown to couple to pairs of fermions leading to a source of flavour violation, shedding light on why particles from the second and third generations decay into their first generation counterparts. These interactions were shown to act only on left-handed particles, leading to the following decomposition:

$$L^1 = \begin{pmatrix} \nu_{eL} \\ e_L \end{pmatrix} \quad L^2 = \begin{pmatrix} \nu_{\mu L} \\ \mu_L \end{pmatrix} \quad L^3 = \begin{pmatrix} \nu_{\tau L} \\ \tau_L \end{pmatrix} \tag{1.1.}$$

$$Q^1 = \begin{pmatrix} u_L \\ d_L \end{pmatrix} \quad Q^2 = \begin{pmatrix} c_L \\ s_L \end{pmatrix} \quad Q^3 = \begin{pmatrix} t_L \\ b_L \end{pmatrix} \tag{1.2.}$$

$$E^{1,2,3} = e_R, \mu_R, \tau_R \quad U^{1,2,3} = u_R, c_R, t_R \quad D^{1,2,3} = d_R, s_R, b_R. \tag{1.3.}$$

1.2. Standard Model Lagrangian

It is of utmost importance to provide a brief conceptual review leading up to the Lagrangian formalism before we define the SM Lagrangian. The Lagrangian of any physical system encompasses the complete information on the dynamics of the system. Its very basis is the Hamilton's stationary-action principle, or the principle of least action. The principle states that the action S of any physical system is defined as

$$S = \int \mathcal{L}_{t_0}^{t_f} dt, \tag{1.4.}$$

and that when the system evolves from t_0 to t_f, it must follow a path for which S is an extremum. This is expressed as $\delta S = 0$, yielding the Euler-Lagrange equation of motion. At this point of the formalism, the complete dynamics of the system is defined. What is crucial to remind the reader now is a theorem describing how conserved quantities are acquired from the symmetries of physical laws. Heavily benefiting from the Lagrangian formalism, the theorem states that every differentiable symmetry of the action of a physical system with conservative forces has a corresponding conservation law. This is known as the Noether's theorem [5].

The SM is a non-abelian gauge theory and is dictated by a symmetry principle. We can start deriving the Lagrangian density for all fundamental interactions by conserving this symmetry; local gauge symmetry. For free massive fermions, $\mathcal{L}$ can be written as

$$\mathcal{L}_{Dirac} = \overline{\psi}(i\not{\partial} - m)\psi, \tag{1.5.}$$

where the first part describes the kinetic term and the second decribes the mass term with ψ being the fermion field of mass m and $\not{\partial} = \gamma_\mu \partial^\mu$. In quantum electrodynamics (QED), requiring the Lagrangian to be invariant under a local $U(1)$ transformation of the field

$$\psi(x) \longrightarrow e^{i\alpha(x)}\psi, \tag{1.6.}$$

and of the spin-1 vector field $A_\mu(x)$

$$A_\mu(x) \longrightarrow A_\mu(x) - \frac{1}{g}\partial_\mu(x), \tag{1.7.}$$

allows defining the covariant derivative

$$D_\mu = \partial_\mu + igA_\mu(x). \tag{1.8.}$$

In addition, the field strength tensor

$$F_{\mu\nu} = \partial_\mu A_\nu - \partial_\nu A_\mu \tag{1.9.}$$

is also invariant under this transformation, and the interaction term for spin-1 particles can be added to the Lagrangian leading up to the following

$$\mathcal{L}_{QED} = -\frac{1}{4}F^{\mu\nu}F_{\mu\nu} + \overline{\psi}(i\not{D} - m)\psi,$$
$$= -\frac{1}{4}F^{\mu\nu}F_{\mu\nu} + \overline{\psi}i\gamma^{\mu}(\partial_{\mu} + igA_{\mu})\psi - m\overline{\psi}\psi, \quad (1.10.)$$

which is effectively invariant under $U(1)$ transformations. The SM Lagrangian is based on the very same gauge invariance by requiring local invariance on

$$SU(3)_C \otimes SU(2)_L \otimes U(1)_Y, \quad (1.11.)$$

where $SU(3)_C$ is the symmetry group of the strong interactions with C referring to the colour, $SU(2)_L \otimes U(1)_Y$ is the symmetry group of EW interactions with L referring to the left-handed fermions and Y referring to the hypercharge. Generalizing the derivation from Eq. 1.8 - 1.9, the covariant derivative and the gauge field tensor can be expressed as

$$D_{\mu} = \partial_{\mu} - igA^a_{\mu}T^a, \; igF^a_{\mu\nu}T^a = [D_{\mu}, D_{\nu}], \quad (1.12.)$$

where T^a is the group generator, A^a_{μ} is the connection term, and g is the gauge coupling. The index a runs over the number of generators of the group being considered, while the index μ takes values 0 for time-like components and 1, 2, 3 for space-like components. For the group $SU(3)_C$, the covariant derivative is then given by

$$D^{ij}_{\mu} = \partial_{\mu} - ig_s G^a_{\mu}\frac{\lambda^{ij}_a}{2}, \quad (1.13.)$$

where G^a_{μ} stands for the eight gauge bosons. Using Eq. 1.12 , the field tensor is found to be

$$G^a_{\mu\nu} = \partial_{\mu}G^a_{\nu} - \partial_{\nu}G^a_{\mu} - g_s f^{abc}G^b_{\mu}G^c_{\nu}, \quad (1.14.)$$

where f^{abc} is the structure constant of the group and g_s the coupling constant of the strong interaction. Then, the QCD Lagrangian can be written as

$$\mathcal{L}_{QCD} = -\frac{1}{4}G^a_{\mu\nu}G^{a\mu\nu} + \overline{\psi_i}\left(i\not{D}^{ij}\right)\psi_j. \quad (1.15.)$$

For the group $SU(2)_L \otimes U(1)_Y$, the covariant derivatives act differently for left-handed and right-handed fermions. They are defined as

$$D_{\mu} = \partial_{\mu} - ig\frac{\sigma_i}{2}W^{\mu i} - ig'\frac{Y}{2}B_{\mu} \quad (1.16.)$$

$$D'_{\mu} = \partial_{\mu} - ig'\frac{Y}{2}B_{\mu}, \quad (1.17.)$$

where σ_i the Pauli matrices generators of the $SU(2)$ group and $W^{\mu i}$ and B_{μ} are the three and one spin-1 bosons associated to the $SU(2)_L$ and $U(1)_Y$ groups, respectively. Then, following Eq. 1.12, their field tensors are expressed as the following

$$W^i_{\mu\nu} = \partial_\mu W^i_\nu - \partial_\nu W^i_\mu + g\epsilon^{ijk} W^j_\mu W^i_\nu \tag{1.18.}$$

$$B_{\mu\nu} = \partial_\mu B_\nu - \partial_\nu B_\mu, \tag{1.19.}$$

with ϵ^{ijk} being the fully antisymmetric structure constant of the $SU(2)$ group. The gauge and fermionic parts of the SM Lagrangian thus can be written as the following

$$\mathcal{L}_{gauge} = -\frac{1}{4} G^a_{\mu\nu} G^{\mu\nu}_a - \frac{1}{4} W^i_{\mu\nu} W^{\mu\nu}_i - \frac{1}{4} B_{\mu\nu} B^{\mu\nu} \tag{1.20.}$$

$$\mathcal{L}_{fermion} = \sum_{\psi,I} \overline{\psi^I} (i\overline{D}) \psi^I. \tag{1.21.}$$

where ψ stands for L, Q, E, U, D from Eq. 1.1 to 1.3 and I stands for the three generations of fermions as presented in 1.2.

So far, the gauge invariance we imposed requires gauge fields to be massless. While this holds true for the gauge bosons of the strong and electromagnatic interactions, g and γ respectively, it does not hold for the gauge bosons of the weak interaction; $W^\pm$ and Z bosons. They are empirically found to be massive. Moreover, the presence of the mass term breaking the gauge invariance of the EW interactions (fermions have far been found to be massive) requires all particles to be massless so far in this formalism. The solution to this problem will be explained in the following section.

1.3. Electroweak symmetry breaking and Higgs mechanism

Adding the mass term in the same manner as Eq. 1.5 would not be allowed as it breaks the gauge invariance of the group $SU(3)_C \otimes SU(2)_L \otimes U(1)_Y$. To allow for fermion and gauge boson masses while recovering the $U(1)$ symmetry, a solution was proposed by Brout, Englert, and Higgs [6–8] making them the naming fathers of the infamous mechanism that sheds light on how matter is attributed with mass.

A scalar doublet ϕ of hypercharge $Y = 1$ and no colour with a renormalizable potential conserving the gauge symmetry, $V(\phi^\dagger\phi)$ is introduced *ad-hoc*. Its Lagrangian is then given by

$$\mathcal{L}_{scalar} = D_\mu \phi^\dagger D^\mu \phi - V(\phi^\dagger\phi). \tag{1.22.}$$

where the potential term is

$$V(\phi^\dagger\phi) = -\mu^2(\phi^\dagger\phi) + \lambda(\phi^\dagger\phi)^2. \tag{1.23.}$$

The lowest energy state of this potential gives the vacuum expectation value (VEV) of the proposed doublet. For $\mu^2 > 0$, the $SU(2)_L \otimes U(1)_Y$ symmetry is not broken and the scalar potential has a minimum at 0. For $\mu^2 < 0$, however, the scalar potential acquires a non-trivial minimum with a non-zero VEV ($v^2 = -\mu^2/\lambda$) and the electroweak symmetry is spontenaously broken (EWSB). Expanding the field around the new non-zero VEV yields

$$\phi(x) = \frac{1}{\sqrt{2}} \exp\left(i\sigma^i \xi_i(x)\right) \begin{pmatrix} 0 \\ v + h(x) \end{pmatrix} \tag{1.24.}$$

where the $\xi_i(x)$ are Goldstone bosons. In the unitary gauge, they can be removed by performing an SU(2)$_L$ rotation yielding the following

$$\phi(x) = \frac{1}{\sqrt{2}} \begin{pmatrix} 0 \\ v + h(x) \end{pmatrix}, \tag{1.25.}$$

where what is denoted with h(x) is the Higgs boson. This term is then inserted back in the scalar Lagrangian yielding the following

$$\mathcal{L}_{scalar} = D_\mu \phi^\dagger D^\mu \phi + \mu^2 (\phi^\dagger \phi) - \lambda (\phi^\dagger \phi)^2 \tag{1.26.}$$

$$= \frac{v^2}{8} \left(g^2 W^i_\mu W^{i\mu} + g'^2 B_\mu B_\nu - 2g' g B_\mu W^{3\mu} \right) \left(1 + \frac{h}{v} \right)^2$$

$$+ \frac{1}{2} \left(\partial_\mu h \partial^\mu h \right) - \lambda v^2 h^2 - \lambda v h^3 - \frac{\lambda}{4} h^4 - \frac{\lambda v^4}{4}. \tag{1.27.}$$

As seen in Eq. 1.27, the $W^{1,2,3}$ and B gauge bosons have now a mass term and that the B field mixes with W^3. The field ϕ is next coupled to the fermions via Yukawa terms giving the Yukawa Lagrangian:

$$\mathcal{L}_{Yukawa} = -\sum_i Y_\ell^{ij} \left(\overline{L}^i . \phi \right) \ell^j + \text{h.c.} \qquad \text{(leptons)}$$

$$= -\sum_{ij} Y^{ij} \left(\overline{Q}^i . \phi^C \right)^j - \sum_{ij} Y^{ij} \left(\overline{Q}^i . \phi^C \right)^j + \text{h.c.} \quad \text{(quarks)}, \tag{1.28.}$$

with $\phi^C = i\sigma_2 \phi^*$. Y_ℓ, Y, Y being the Yukawa couplings of the leptons (electron, muon, and tau), the up-type quarks (up, charm, top) and down-type quarks (down, strange, bottom). The fermion masses and the coupling of fermions to Higgs (proportional to their masses) originate from this term in the SM Lagrangian.

The standard model Lagrangian can then finally be written in a complete way as:

$$\mathcal{L}_{SM} = \mathcal{L}_{fermions} + \mathcal{L}_{gauge} + \mathcal{L}_{scalar} + \mathcal{L}_{Yukawa}. \qquad (1.29.)$$

Therefore at this point we proved that adding the scalar field ϕ assigns mass terms to otherwise massless gauge bosons and fermions. Then, writing the Lagrangian in the unitary gauge gives

$$\mathcal{L}_{scalar} \ni \frac{1}{2}\left(\partial_\mu h \partial^\mu h\right) - \lambda v^2 h^2 - \lambda v h^3 - \frac{\lambda}{4} h^4 - \frac{\lambda v^4}{4}. \qquad (1.30.)$$

Eq. 1.30 provides the following terms:

- Higgs boson mass $m = \sqrt{2\lambda} v$
- Higgs trilinear self coupling λv
- Higgs quartic self coupling λ.

The VEV, by using the masses of gauge fields, was found to be $v \simeq 246$ [4] With its discovery in 2012, Higgs boson mass has been measured to be $m = 125.09 \pm 0.24$ GeV [9]. Therefore, predicting the value of λ was made possible by using the relation between m_H, v, and λ:

$$\lambda^{SM}_{HHH} = \frac{m_H^2}{2v^2} \simeq 0.13. \qquad (1.31.)$$

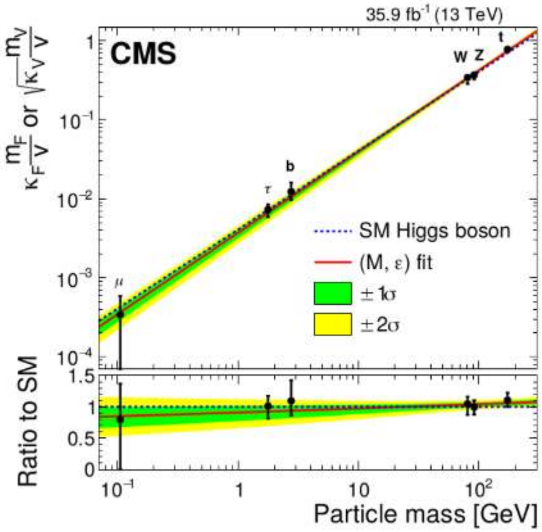

Figure 1.1. | Measurement of the coupling of the Higgs with the top and bottom quarks, and the tau and muon leptons, and the weak bosons W and Z, performed by the CMS collaboration [10].

The trilinear coupling can soon be in our grasp through the observation of Higgs pair production (one of the main motivations behind High Luminosity LHC), whereas the quartic coupling is still far from our reach given the extremely small cross-section of triple Higgs production. Experimental efforts put in place since its discovery confirmed the Higgs boson's couplings to several fermions and weak bosons to be compatible with theory predictions as shown in Figure 1.1.

1.4. Higgs pair production in the Standard Model

As described in Section 1.3, double and triple Higgs production are the only processes providing access to Higgs self couplings. As the former is expected to be possible to characterise at the LHC, it is crucial to do a review of its production mechanisms here in this theory chapter. Figure 1.2 shows the Feynman diagrams of the processes that will be covered in this section.

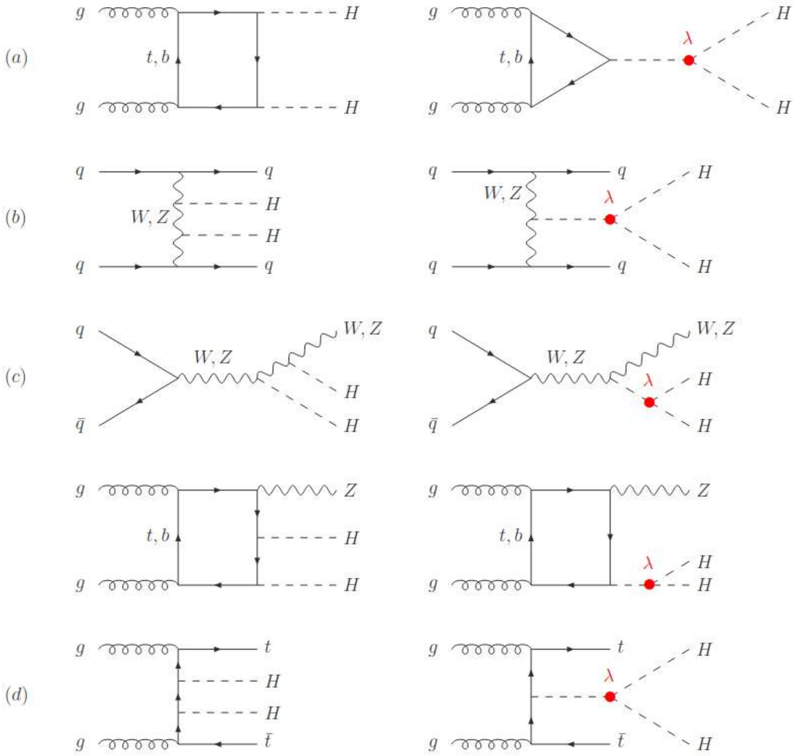

Figure 1.2. | Diagrams contributing to Higgs pair production: (a) gluon fusion, (b) vector-boson fusion, (c) double Higgs-strahlung and (d) double Higgs bremsstrahlung off top quarks. The trilinear Higgs coupling contribution is marked in red. From [11].

Gluon fusion: Loop-induced gluon-fusion (ggF) mediated by top quark loops is the dominant Higgs pair (HH) production mode. Similar to single Higgs production, there are two kinds of diagrams describing the HH production: box (Fig. 1.2a left) and triangle 1.2a right) diagrams that interfere destructively. This destructive interference leads to a reduction of about 50% in the total cross section at the leading order (LO). The QCD corrections are known up to next-to-leading order (NLO), and at next-to-next-to-leading order (NNLO) in the limit of heavy top quarks.

Vector-boson fusion: This is the second-largest production mode and mainly mediated by t-channel W and Z exhange, similar to the single Higgs case. Corresponding to Figure 1.2b, It involves continuum diagrams originating from two Higgs radiations off the virtual W or Z bosons, and diagrams in which an off-shell Higgs splits into a Higgs pair. The QCD corrections are known up to N^3LO.

Double Higgs-strahlung: This mechanism corresponds to the associated production of Higgs pairs with a W or Z boson. It has a significantly lower production rate than the VBF. The QCD corrections to the cross section is known at NLO and NNLO which increase the total cross section by about 30%. This mechanism shown in Figure 1.2c.

Double Higgs bremsstrahlung off top quarks: This mechanism corresponds to the associated production of Higgs pairs with top quark pairs as shown in Figure 1.2d. While this mode has significantly small cross section for center of mass energy of 13 TeV, it reaches a cross section value close to the VBF at a 100 TeV collider. The QCD corrections to the cross section are negative and modify the total cross section at the level of 20%.

1.5. Open questions in the Standard Model

Despite its tremendous success in proving accurate in uncountable predictions, SM fails to provide answers to some very fundamental questions. This section aims to give a short overview of these open questions that SM does not address.

- The so-called **hierarchy problem** is caused by the disagreement between the experimentally measured Higgs boson mass and what SM suggests. The Higgs mass can be considered as the sum of the bare mass M_{bare} and the loop corrections δM where $M^2_{measured} = M^2_{bare} + \delta M^2$. The corrections are quadratically divergent with Λ^2 where Λ is the cut-off scale. Then, at very high values of Λ the quantum corrections become very large and hence imply a boost in the Higgs boson mass. As this was experimentally falsified, this issue stays as an open question.
- Cosmological models and astronomical observations showed that more than 80% of matter in the universe is composed of **dark matter**. This matter

$\sqrt{s}$	13 TeV	14 TeV	27 TeV	100 TeV
ggF HH	$31.05^{+2.2\%}_{-5.0\%} \pm 3.0\%$	$36.69^{+2.1\%}_{-4.9\%} \pm 3.0\%$	$139.9^{+1.3\%}_{-3.9\%} \pm 2.5\%$	$1224^{+0.9\%}_{-3.2\%} \pm 2.4\%$
VBF HH	$1.73^{+0.03\%}_{-0.04\%} \pm 2.1\%$	$2.05^{+0.03\%}_{-0.04\%} \pm 2.1\%$	$8.40^{+0.11\%}_{-0.04\%} \pm 2.1\%$	$82.8^{+0.13\%}_{-0.04\%} \pm 2.1\%$
ZHH	$0.363^{+3.4\%}_{-2.7\%} \pm 1.9\%$	$0.415^{+3.5\%}_{-2.7\%} \pm 1.8\%$	$1.23^{+4.1\%}_{-3.3\%} \pm 1.5\%$	$8.23^{+5.9\%}_{-4.6\%} \pm 1.7\%$
W^+HH	$0.329^{+0.32\%}_{-0.41\%} \pm 2.2\%$	$0.369^{+0.33\%}_{-0.39\%} \pm 2.1\%$	$0.941^{+0.52\%}_{-0.53\%} \pm 1.8\%$	$4.70^{+0.90\%}_{-0.96\%} \pm 1.8\%$
W^-HH	$0.173^{+1.2\%}_{-1.3\%} \pm 2.8\%$	$0.198^{+1.2\%}_{-1.3\%} \pm 2.7\%$	$0.568^{+1.9\%}_{-2.0\%} \pm 2.1\%$	$3.30^{+3.5\%}_{-4.3\%} \pm 1.9\%$
$t\bar{t}HH$	$0.775^{+1.5\%}_{-4.3\%} \pm 3.2\%$	$0.949^{+1.7\%}_{-4.5\%} \pm 3.1\%$	$5.24^{+2.9\%}_{-6.4\%} \pm 2.5\%$	$82.1^{+7.9\%}_{-7.4\%} \pm 1.6\%$
$tjHH$	$0.0289^{+5.5\%}_{-3.6\%} \pm 4.7\%$	$0.0367^{+4.2\%}_{-1.8\%} \pm 4.6\%$	$0.254^{+3.8\%}_{-2.8\%} \pm 3.6\%$	$4.44^{+2.2\%}_{-2.8\%} \pm 2.4\%$

Table 1.3. | Signal cross sections (in fb) for HH production including the available QCD corrections. From [11].

would be electrically neutral, weakly-interacting particle with mass around the electroweak scale. The SM does not account for dark matter.

- The SM assumes massless neutrinos. However, neutrino observatories have showed evidence on the phenomenon called neutrino oscillations where neutrinos change flavor as they travel long distances. This could be explained by **neutrino mass** and neutrino flavor eigenstates, implying that the neutrinos have a non-zero mass.
- The **baryon symmetry** as an open question is about the fact that the Big Bang should have created equal amounts of matter and anti-matter. Astronomical observations so far fail at detecting a large amount of antimatter.
- As described in the previous sections, the SM is a non-gravitational theory. It is unable to incorporate **gravitational interactions** within the model as the addition of a hypothetical boson (graviton) mediating this interaction would lead to a non-renormalizable theory.

Chapter

2.

An Apparatus: The Compact Muon Solenoid

The first chapter was dedicated to our current best theoretical framework of fundamental interactions between elementary particles. This second introductory chapter will describe the other side of the story; the experimental apparatus we are using to test the predictions made by the SM. Starting with the accelerator complex at CERN, we will move to the description of the CMS experiment and detector along with methods used to make sense out of the data recorded by the detector.

2.1. The Large Hadron Collider

The Large Hadron Collider is so far the world's most powerful particle accelerator and collider and lies in a tunnel beneath the Franco-Swiss border near Geneva. Having a circumference of 27 km, LHC re-uses the tunnel that was built for the previous machine, the Large Electron Positron Collider (LEP). Even before LEP started running, scientists started thinking about the LHC in the early 1980s and its construction was officially approved in 1994 [12].

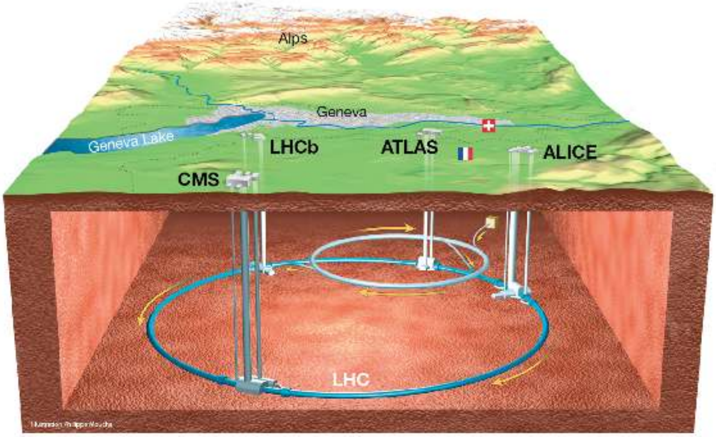

Figure 2.1. | An illustration of the LHC ring located beneath Franco-Swiss border [13].

LEP was limited because the energy loss of the electrons due to synchrotron radiation is large. Under this limitation, LEP could maximally reach an energy of 209 GeV. However the LHC currently reaches a center of mass collision energy of 13.6 TeV, since the energy loss of hadrons caused by synchrotron radiation is much lower than that of the lighter particles such as electrons and positrons.

Along with its prime motivation, i.e., search for the Higgs Boson, LHC was also designed to investigate the Charge-Parity Violation, Supersymmetry, Dark Matter, Antimatter, and the state of matter that existed in the early Universe called Quark-Gluon Plasma, as well as any kind of new physics.

2.1.1. Design

LHC is a two-ring superconducting hadron accelerator and collider located at a typical depth of 100 m and on a plane tilted with 1.4% slope towards Lake Geneva. The depth is around 175 m under the Jura mountains and 50 m towards Lake Geneva. Re-using the existing tunnels from the LEP was approved because not only it would be less costly but also the earth's crust would be a good shielding for the radiation produced.

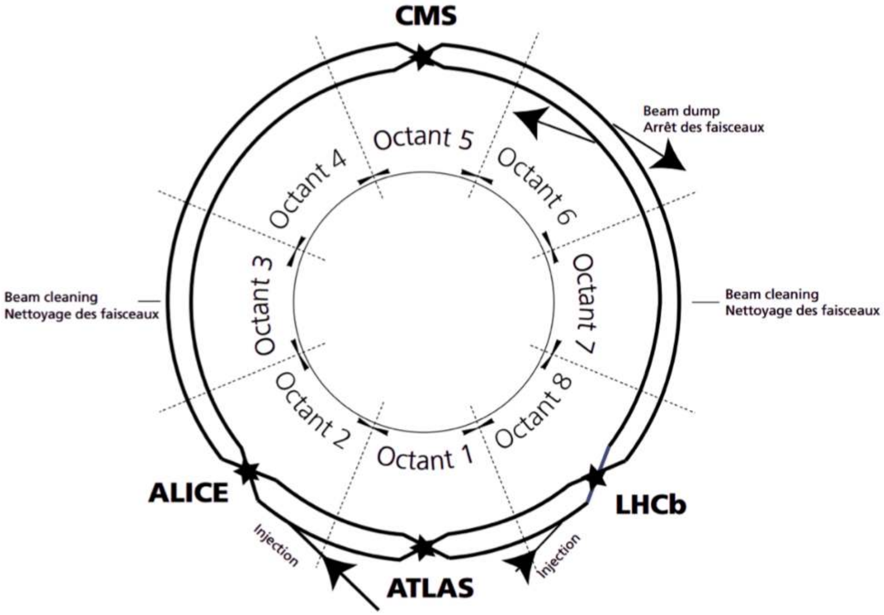

Figure 2.2. | Schematics of the LHC layout [14].

The LHC is not a perfect circle with its arcs and straight sections and its basic layout follows the LEP tunnel geometry. It has eight arcs and eight insertions where insertion means a long straight section consisting of two transition regions. The octants shown in Figure 2.2 are regions that start from the middle of an arc and end in the middle of the following arc, hence spanning a full insertion. Each arc is 2.45 km long and each one contains 154 dipole bending magnets. Each insertion is 528 m long and the specific use of each insertion can be different, e.g. physics (beam collisions within an experiment), injection, beam dumping, beam cleaning. Of eight straight sections there are, only four are used and the remaining four are suppressed, i.e., the beams cross at only four of these sections. There are four experimental insertions for each of these beam crossings which are the ATLAS experiment at Point 1, the CMS experiment, which is located diametrically opposite to the ATLAS experiment, at Point 5, the ALICE experiment at Point 2, and the LHCb experiment at Point 8. Point 2 and Point 8 also house the injection systems for Beam 1 and Beam 2, respectively. Point 3 and Point 7 include collimation systems; Point 6 contains the beam dump insertion, where the two beams are vertically extracted from the machine [15].

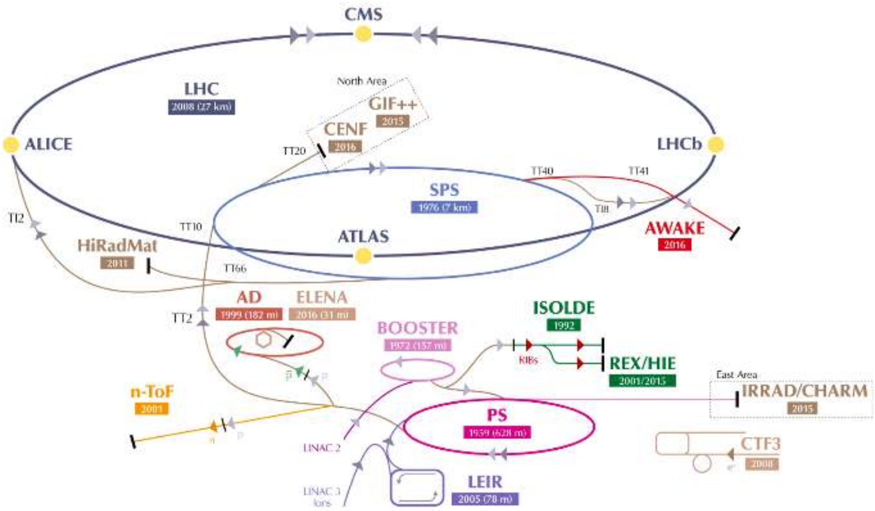

Figure 2.3. | Schematics showing the accelerator complex [16].

The process of accelerating a proton to 0.999999991 times the speed of light is not done only by the LHC ring. The LHC itself is fed by a number of particle accelerators, working in sequence to achieve a final energy of 7 TeV. Starting with the extraction of protons from the gaseous hydrogen, these protons are first accelerated to 50 MeV in Linac 2 and then fed into the Booster, the first ring of the acceleration process. After the protons are accelerated to 1.4 GeV in the Booster, they are passed on to the Proton Synchrotron (PS) to be accelerated to 25 GeV. It is right here at the PS that the LHC bunch crossing frequency is set to

40 MHz (corresponding to 25 ns time spacing). The protons are then injected into the Super Proton Synchrotron (SPS) where they are accelerated, one last time before being passed on to the LHC, to 450 GeV. The protons at 450 GeV are then injected into the LHC from the injection points at Octant 2 and Octant 8 and are then accelerated and kept at constant energy by the Radio Frequency cavities up to 6.8 TeV. While in the LHC, the beams are kept in circular orbits by the dipole magnets and are focused by the quadrupole magnets. The two beams are then collided at the four interaction points corresponding to four experimental insertions, i.e., the four big experiments ATLAS, CMS, ALICE, LHCb. There are three secondary experiments installed at the LHC; the Large Hadron Collider forward (LHCf) experiment, the TOTal Elastic and diffractive cross section Measurement (TOTEM) experiment, and Monopole and Exotics Detector at the LHC (MoEDAL).

2.1.2. Luminosity and pileup

The two most important characteristics of a collider are its center-of-mass energy and luminosity. This is the parameter that impacts the amount of data collected and can be expressed as the production rate of a given process divided by its cross section. The number of events per second generated at the LHC collisions, for any desired process, is then:

$$\frac{dN}{dt} = \mathcal{L}\sigma_{\text{process}} \tag{2.1.}$$

where L is the *instantaneous luminosity*. L, when the beam has a Gaussian profile, can be expressed as [17]:

$$\mathcal{L} = \frac{f_r N_b N_p^2}{4\pi\sigma_x\sigma_y} = \frac{f_r N_b N_p^2}{4\pi\epsilon\sqrt{\beta_x^*\beta_y^*}} \tag{2.2.}$$

where:

- f_r = 11.245 kHz is the revolution frequency,
- N_b =[2208,2546] is the number of colliding bunches (variable per data-taking year and per fill),
- $N_p = 1.1\ 10^{11}$ is the proton density per bunch,
- $\sigma_{x,y}$ = 11 µm is the standard deviation of the assumed Gaussian shaped beam density profile at the IP,
- ϵ = 0.3 nm is the un-normalized beam emittance,
- $\beta^*_{x,y}$ = 40 cm is the minimum of the betatron function $\beta_{x,y}(s)$ – as a function of the s position along the ring – at the IP, by definition $\sigma_{x,y} = \sqrt{\epsilon\beta^*_{x,y}}$.

during the data taking between 2016 and 2018. Since in a real-life collider two beams do not collide head on but with a small crossing angle to avoid multiple bunch collisions, a reduction factor needs to be applied on the luminosity:

$$R_{geometrical} = \frac{1}{\sqrt{1+\left(\frac{\sigma_z\theta_C}{2\sigma_x}\right)^2}} \tag{2.3.}$$

where $\theta_C =$ is the crossing angle, $\sigma_z =$ is the longitudinal RMS bunch length, and $\sigma_x =$ is the transverse RMS bunch size under the assumption that $\sigma_x = \sigma_y$. The instantenous luminosity is computed from the beam parameters that change with respect to time. Its integral over time then yields the *integrated luminosity*:

$$\mathcal{L}_{\text{int}} = \int \mathcal{L} dt. \tag{2.4.}$$

Among other methods that can provide a real-time value of the instantaneous luminosity, a detector-dependent method is preferred. This method uses luminometers and the interactions for which the cross-section is known to a high degree of precision. The rate of the interaction is then:

$$R = \sigma_{\text{ref}}\mathcal{L} \tag{2.5.}$$

where luminosity can be extracted as follows by choosing the reference process as the inelastic collision of a proton:

$$\mathcal{L} = \frac{\mu f_r}{\sigma_{\text{inel}}} = \frac{\mu_{\text{vis}} f_r}{\epsilon\sigma_{\text{inel}}} = \frac{\mu_{\text{vis}} f_r}{\sigma_{\text{vis}}}, \tag{2.6.}$$

where μ is the average number of collisions per bunch crossing, called *pileup*.

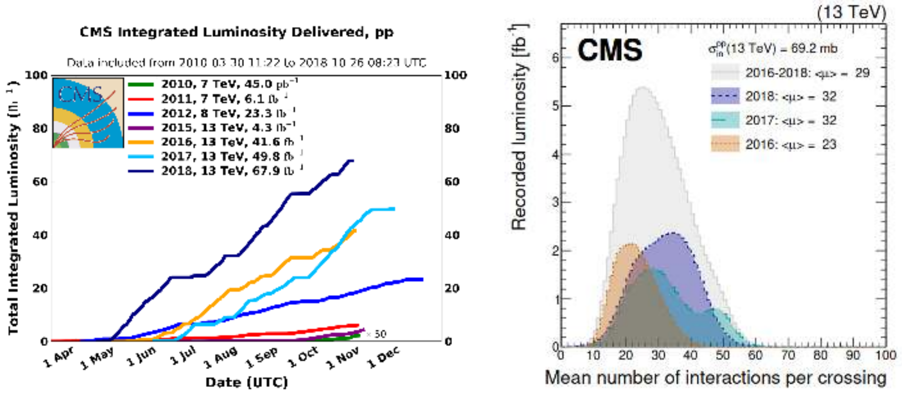

(a) **(b)**

Figure 2.4. | Evolution of the integrated luminosity (left) and average pileup (right) along the data-taking years for the CMS experiment between 2010 and 2018. From Ref. [18] and Ref. [19].

Figure 2.4 shows the evolution of luminosity and pileup recorded by the CMS experiment.

2.1.3. The Detectors and Experiments of the LHC

There are a total of seven experiments installed at the LHC as mentioned in the previous section. A Toroidal LHC ApparatuS (ATLAS) and the Compact Muon Solenoid (CMS) are general-purpose detectors designed to cover the widest possible range of physics at the LHC, from precision measurements of the Higgs boson to searches for new physics beyond the Standard Model. A Large Ion Collider Experiment (ALICE) is designed to investigate the state of matter that existed in the early Universe called Quark-Gluon Plasma. The Large Hadron Collider beauty (LHCb) experiment is designed to study the B-particles; events and interactions with b quark. The two minor experiments LHCf and TOTEM are forward detectors located near the collision points of ATLAS and CMS detectors respectively. The third minor experiment MoEDAL is a detector located near the collision point of LHCb detector and is designed to investigate hypothetical particles.

2.2. The Compact Muon Solenoid detector

The Compact Muon Solenoid (CMS) is a multi-purpose detector with physics motivations including search for the Higgs Boson, which was discovered together with ATLAS, search for supersymmetric particles, search for new massive vector bosons, and search for extra dimensions. Weighing 12.500 tonnes and being 21.6 m long, 14.6 m high and 14.6 m wide, it is *compact*. With the intense bending power of the magnets which actually contain more iron than the Eiffel Tower, measuring the momentum of *muon*s with a higher precision was the driving force behind the detector design. This bending power, resulting from the 3.8 T magnetic field is provided by the superconducting *solenoid* magnet.

Built around its central piece, the superconducting solenoid magnet, CMS has a cylindrical shape with a symmetry in the azimuthal angle ϕ. The bore of the solenoid is large enough to accommodate the tracker and the calorimetry inside. Being the closest detectors to the beam, trackers are surrounded by the Electromagnetic Calorimeter (ECAL), and ECAL is surrounded by the brass/scintillator sampling Hadron Calorimeter (HCAL). The iron return yoke interspersed with muon chambers are the outer layers positioned right after the solenoid [20].

2.2.1. Coordinate conventions

Located at the north of the LHC center, CMS detector has the origin centered at the collision point and uses a right-handed Cartesian coordinate system. The x-axis is horizontal, pointing radially inward toward the center of the LHC, the y-axis is vertical, pointing upward, and hence the z-axis points along the beam direction. Considering the cylindrical structure of the CMS, a polar coordinate system is used as well and it is defined such that the azimuthal angle ϕ is measured from the positive x-axis in the x-y plane (*the transverse plane*) and the radial coordinate in this plane is defined as r, the polar angle θ is measured from the z-axis in the r-z plane, and the pseudorapidity, which is a spatial coordinate calculated by using θ, is defined as $\eta = -ln[tan(\theta/2)]$.

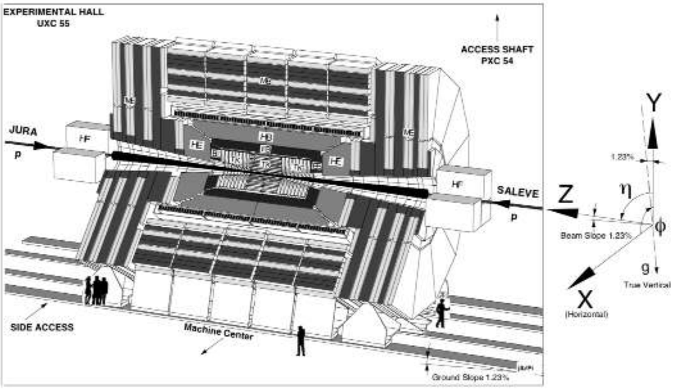

Figure 2.5. | An overall view of the CMS with its coordinate system.

2.2.2. Tracker

The trajectory of a particle with a positive or negative charge is bent under the influence of a magnetic field. The tracker system was designed to provide a precise measurement of the bent trajectories of the particles (under the influence of the homogeneous magnetic field provided by the solenoid magnet) emerging from the LHC collisions as well as to reconstruct the secondary tracks of the charged particles produced in the decays of the primary particles inside the tracker volume. Surrounding the interaction point, it is the closest detector system to the collisions. It consists of two parts: the vertex or pixel detector and the Silicon Strip Tracker (SST).

2.2.2.1. The pixel detector

Being the closest to the interaction region, pixel detector is the innermost detector sub-system and is exposed to the highest fluence. It's initial design consisted of three barrel layers and two endcap disks with 250 µm thin silicon pixel detectors with a pixel cell size of 100×150 m^2, covering a pseudorapidity range of $-2.5 < \eta < 2.5$. It contributes tracking points in $r - \phi$ and z therefore it is essential for the reconstruction of secondary vertices. By design, it was

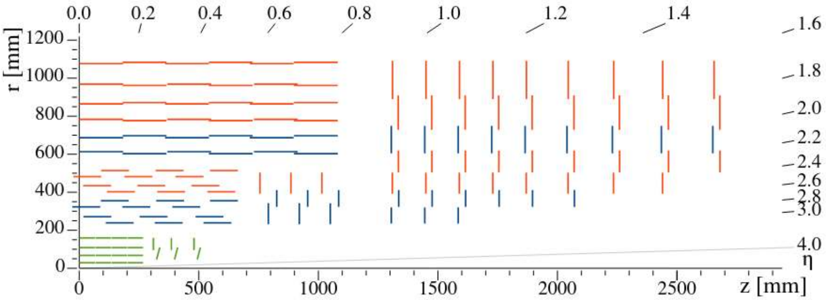

Figure 2.6. | Sketch of one quarter of the Phase-1 CMS tracking system in $r-z$ view. The pixel detector is shown in green, silicon strip tracker is depicted in blue and red [21].

expected that the pixel detector would require a replacement mid LHC. In 2017, the CMS collaboration installed a new detector called Phase-1 pixel detector with the main motivation being maintaining the overall performance of the tracking system with the increase in instantaneous luminosity. The main design guidelines were shaped around overcoming the dynamic inefficiencies by upgrading the readout chips and increasing the readout bandwidth. However, the detector geometry was improved as well by the addition of extra layers both in the barrel region (BPix) and in the forward region (FPix). The current pixel detector in use has therefore four barrel layers, the BPix and three disks on each side, the FPix.

2.2.2.2. The silicon strip tracker

Surrounding the pixel detector, silicon strip tracker allows for the measurement of the momentum of charged particles. It consists of four partitions: the inner and outer barrel, the inner disks, and the endcap. This sub-system is of central interest for this dissertation. Therefore it will be explained in detail in the next chapter.

2.2.3. Electromagnetic Calorimeter

As it is the case for most of the particle physics experiments, a distinction is made between electromagnetic calorimetry and hadron calorimetry. The electromagnetic calorimeter (ECAL) of the CMS, as the other electromagnetic calorimeters do, measures the energy of the particles that interact through the electromagnetic force, i.e., it is based on the production of electromagnetic showers. The ECAL is a hermetic homogeneous calorimeter made of lead tungstate ($PbWO_4$) and comes right after the trackers, consisting of two main parts; barrel and endcaps. The barrel part, comprising 61200 ($PbWO_4$) crystals, covers the pseudorapidity range of $|\eta| < 1.479$. The endcaps, having 7324 ($PbWO_4$) crystals mounted on each, cover the pseudorapidity range of

$1.479 < |\eta| < 3$. The driving criteria in the design was the capability to measure the two-photon decay mode for $m_H \leq 150$ GeV and to measure the electrons and positrons from the decay of Ws and Zs originating from the $H \rightarrow ZZ^{(*)}$ and $H \rightarrow WW$ decay chain for 140 GeV $\leq m_H \leq$ 700 GeV.

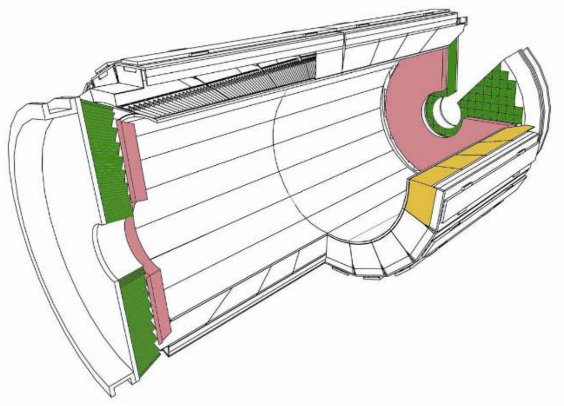

Figure 2.7. | Layout of the CMS ECAL. One of the 36 barrel supermodules is highlighted in yellow, and the endcaps are highlighted in green.

Having short radiation (0.89 cm) and Molière lengths (2.2 cm) and being fast (about 80% of the light is emitted from the crystals in 25 ns, which is the same as the LHC bunch crossing frequency) made it certain that the lead tungstate was the ideal choice for the design. The light pulses that are converted from electrons and photons are read out by the silicon photodiodes. Avalanche photodiodes (APDs) to collect the scintillation light are used in the barrel, and to survive a much higher radiation dose and neutron fluence vacuum phototriodes (VPTs) are used in the endcap regions.

A very front-end card (VFE) is responsible for amplifying the signal from five photo-detectors. These signals are then digitised by ADCs and the corresponding ADC gain is forwarded to the front-end card. In the front-end, the signals carried from VFE cards are kept awaiting a Level-1 accept signal. Upon receiving the Level-1 accept signal, the signals from ten consecutive bunch crossings are sent to the off-detector read-out system.

2.2.4. Hadron Calorimeter

Surrounding the electromagnetic calorimeter (ECAL), HCAL is a sampling hermetic calorimeter designed to measure the timing and energy of hadronic showers. In accordance with the CMS geometry, HCAL consists of a central barrel region and two endcap disks.

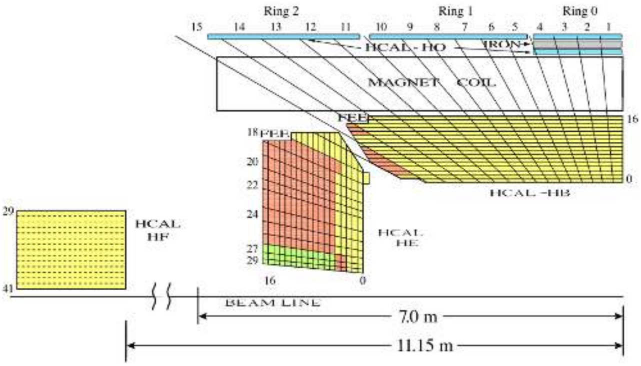

Figure 2.8. A quarter slice of the CMS HCAL detectors. The right end of the beam line is the interaction point. FEE denotes the location of the Front End Electronics for the barrel and the endcap. In the diagram, the numbers on the top and left refer to segments in η, and the numbers on the right and the bottom refer to scintillator layers [22].

As shown in Figure 4.1, the HCAL is organised into a central barrel, comprising the Outer (HO) and Barrel (HB), endcap (HE), and forward (HF) sections. The barrel and endcaps are positioned such that they are the last layer of subsystems put inside the magnet, coming after the electromagnetic calorimeter and the tracker as seen from the collision point. The barrel is restricted by the inner extent of the magnet coil from above and by the outer extent of the electromagnetic calorimeter from below which in turn leaves the possibility of some particles escaping from HB, and hence HO is positioned right after the magnet coil, complementing the barrel and ensuring no energy leaks left undetected. The forward sections (HF) are positioned relatively farther from the interaction point, outside of the magnetic volume, and is designed to detect particles escaping from the collision point at low angles relative to the beam line.

Hadron Outer is an additional layer of scintillators placed outside of the solenoid magnet, as the first layer of each of the five iron yoke rings to ensure that the perfect absorption/containment of the hadronic showers. The central ring has two layers of HO scintillators and all other rings have only one layer of scintillator. Specifically designed to account for identifying late starting showers and measuring their energy, HO covers the pseudorapidity range of $|\eta| < 1.3$. Out of 9072 readout channels of HCAL, HO contributes 2160 channels where the readout signal is acquired from the collection of the scintillation light by wavelength shifting (WLS) fibers and then their transfer to hybrid photodiodes (HPD).

Hadron Barrel is a heterogeneous sampling calorimeter, meaning it consists of alternating layers of absorbers and scintillators, and covers the pseudorapidity range of $-1.3 < \eta < 1.3$. Surrounding the lead tungstate electromagnetic barrel (EB), it is formed by two half barrels and is cylindrically symmetric. Each half barrel holds 18 wedges having a segmentation $\Delta\phi = 20^\circ$. The wedge consists of layers of copper alloy absorber plates and each plate accommodates 9 mm thick slots for the scintillator trays.

Hadron Endcap consists of two disks, endcap minus (HEM) and endcap plus (HEP), inserted into the ends of the solenoid magnet (attached to the muon endcap yoke), hence made of non-magnetic material, covering the pseudorapidity region $1.3 < |\eta| < 3$. HE contains about 34% of the particles produced in the final state. As in HB, HE is made of 18 wedges on each side and is composed of brass absorber plates and active plastic scintillating tiles. Of 9072 readout channels of HCAL, 2592 channels (exactly the same number of channels that HB contributes) belongs to HE. Again identical to HB, the scintillation light from the tiles are collected by WLS and read out by hybrid photodiodes (HPD).

Hadron Forward calorimeters are cylindrical steel structures installed outside of the muon endcap yokes. They are azimuthally subdivided into 18 wedges on each side, and are embedded with radiation hard quartz fibers. HF differs from the rest of the HCAL with quartz fibers producing and collecting the Cherenkov light and photomultiplier tubes (PMT) forming the readout. Out of 9072 readout channels, HF contributes 1728 channels. The pseudorapidity region covered by HF is rather wide and is $3.0 < |\eta| < 5.0$.

The HPDs of the hadron calorimeter were replaced by silicon photomultipliers (SiPM) within the scope of the Phase 1 Upgrade of CMS. HPDs were chosen as photodetectors for their gain (of about 2000) and their magnetic field tolerance. However, some anomalous signals (not coming from beam collisions) during Run 1 proved to be caused by electrical discharges from the HPDs. SiPMs, on the other hand, have about a gain of 10^5 , and are operated at a much less voltage of about 100 V, compared to the 8 kV that is required for the HPDs, and are not sensitive to magnetic fields, hence they eliminate the sources of anomalous signals. SiPMs are also much smaller in size compared to HPDs and this implies that more channels can be fit in the same physical space. This makes the main component of the Phase 1 Upgrade to be the replacement of HPDs with SiPMs which in turn makes it the first large scale use of SiPMs in a radiation environment. To be compatible with the new readout for the new photosensors, the associated front-end electronics were also upgraded.

2.2.5. Superconducting Solenoid Magnet

Yielding a magnetic field of 3.8 T over a length of 12.5 m and a free bore radius of 5.9 m, this large superconducting solenoid was the central feature of the CMS design i.e. precise momentum measurement of charged particles while they escape from the interaction point by bending their track. It is made of superconducting Niobium Titanium *(NiTi)* wires which are traversed by an electrical current of 20,000 Amperes to reach the nominal magnetic field of 3.8 T. The 5.9 m radius is large enough to accommodate the trackers (pixel tracker and silicon tracker), electromagnetic calorimeter and hadron calorimeter inside.

2.2.6. Muon system

Muon detection is the most powerful tool to detect interesting events over the background since they are less affected than electrons by radiative losses in the tracker material, e.g., a "gold plated" signal of the Higgs boson is its decay into four leptons, of which the best resolution is achieved if the leptons are muons ($H \rightarrow ZZ^{(*)} \rightarrow 4\mu$). Positioned right after the solenoid magnet, the muon system in the CMS is the outermost detector system and is expected to perform three major tasks: muon identification (the central theme and the middle name of the experiment), muon triggering, and momentum measurement via the three types of gaseous detectors: drift tubes (DT) in the barrel region, cathode strip chambers (CSC) in the endcap region, and resistive plate chambers (RPC) in both the barrel and endcap. The solenoid magnet and the return yokes help ensure the performance of these tasks. Interspersed with the iron return yokes, the muon detectors obey the cylindrical geometry of the solenoid magnet, hence comprising a barrel region and planar endcaps. The barrel region, covering the pseudorapidity region $|\eta| < 1.3$, consists of four muon stations, MB1 to MB4, of 250 chambers. The endcaps also have four stations, ME1 to ME4, and cover the pseudorapidity region $|\eta| < 2.4$. Figure 2.9 shows the layout of one quarter of the muon system.

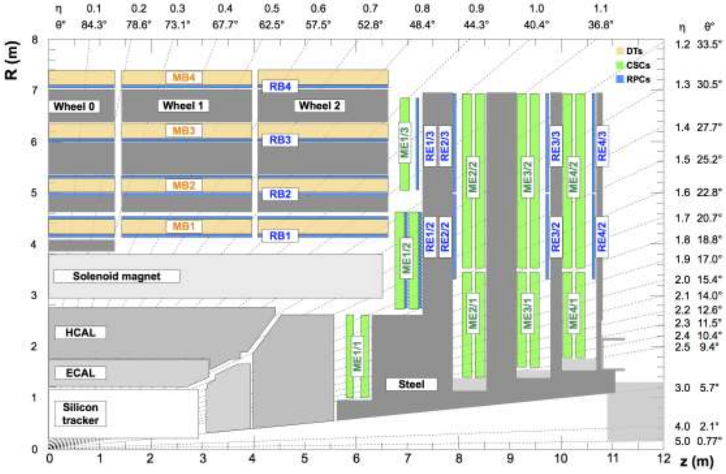

Figure 2.9. | The layout of one quarter of the CMS muon system. From Ref. [23]

2.2.7. Trigger and data acquisition

At the LHC, proton bunches are collided with an interaction rate of 40 MHz, every 25 ns. This high interaction rate then results in very high number of events rendering the storage and processing unfeasible. However, the events of interest represent only a fraction of the bulk of collision events which then necessitates a system of selection for the interesting events. The trigger system serves for this exact purpose: providing a drastic rate reduction through the first step, the Level-1 (L1) Trigger and further reduction through the second step, the High-Level Trigger (HLT).

Level-1 Trigger

The Level-1 (L1) is a hardware system consisting of programmable electronics that perform the first step of the rate reduction. The trigger primitives that are summary information from calorimeters and muon detectors are provided to this system. The L1 then provides an accept or reject signal within 3.8 μs of a collision. The hardware system consists of two sub-systems: the Calorimeter Trigger and the Muon Trigger.

The calorimeters of the CMS, ECAL and HCAL, provide the input to the calorimeter trigger system. This input is prepared by the Trigger Primitive Generators (TPG) which are integrated with the calorimeter read-out. They sum the transverse energies deposited in the calorimeters to obtain the trigger tower E_T and attach the correct bunch crossing number where trigger towers are divisions of calorimeters. Each trigger tower has an (η, ϕ) coverage of the 0.087×0.087 up to the region $|\eta| = 1.74$. Regions beyond this η have larger trigger towers. The electron/photon candidates are determined by the The Regional Calorimeter Trigger (RCT) after being provided with the TPGs. The e/γ candidates originate from a local energy maximum in ECAL towers and then adding the next-highest energy deposit in one of the neighboring towers. A shape and isolation criteria is applied as the next step and hadronic energy is computed.

Jet candidates originate from a local energy maximum in HCAL (and HF) which is also called *the seed*. They are built as 9×9 lattice and the four neighboring clusters with a 3×9 lattice are used for the evaluation of pileup contamination. The three lowest of these contributions are removed and the jet energy is calculated. A final energy correction is applied on this candidate, on its p_T and η.

The missing transverse energy is defined as the negative sum of all energy deposits above threshold up to $|\eta| = 5$. The threshold is both η and pile-up dependent.

The muon trigger system receives the trigger primitives from three different

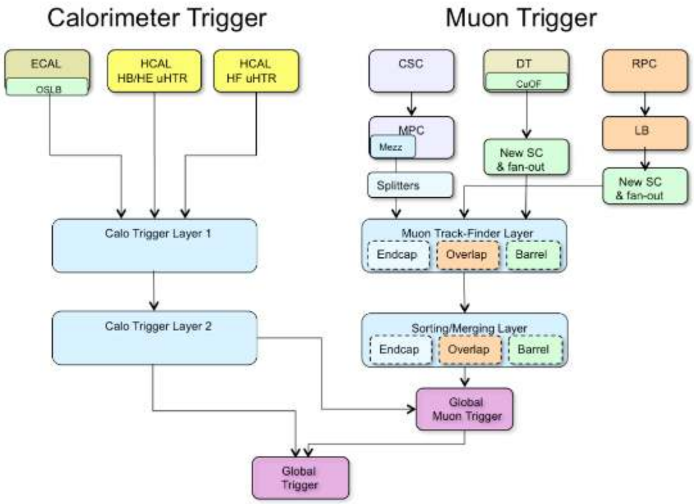

Figure 2.10. | Schematic representation of the Level-1 trigger system. From Ref. [24]

sub-systems: Drift Tubes (DT), Cathode Strip Chambers (CSC) and Resistive Plate Chambers (RPC). The hits from the DT and CSC are combined into track segments, while the hits from RPC are clustered together to deliver their own track segments. These track segments are the trigger primivites and they are fed into track-finders depending on their geometrical position. The barrel muon track finder (BMTF) covers the $|\eta| < 0.83$, the overlap muon track finder (OMTF) covers $0.83 < |\eta| < 1.23$, and the endcap muon track finder (EMTF) covers the $1.24 < |\eta| < 2.4$. The muon candidates from the three systems are then sent to the global muon trigger where the information from calorimeter trigger is also benefited for muon isolation. The candidates are then transferred to the final stage of L1 trigger, the Global Trigger (GT). All trigger objects (calorimeter and muon candidates) are then filtered by a menu of triggers containing up to 512 conditions or *trigger paths* to generate the Level-1 accept signal. The output rate of the L1 system is at 100 kHz which is where the drastic rate reduction happens. Depending on the filling scheme of the LHC, where an approximate rate is 40 MHz, the reduction factor is $\frac{1}{400}$. Therefore, only 0.25% of the collisions are kept.

Data acquisition and High-Level Trigger

All events that triggered the L1A signal are transferred to a computer farm of about 22000 CPU cores for further physics selections and event filtering using faster versions of the offline reconstruction software. For accepted events, the

L1A signal is propagated back to the front-end buffers that store the collision information. Upon the the arrival of L1A signal, the stored data is sent to the Front-end Drivers (FED) which are further transferred to Front-end Readout Optical Links (FEROL). FEROLs then assemble and merge data coming from a certain number of FEDs to build an event fragment and transmit it on 10 GB optical links. Event fragments belonging to the same L1A from all FEDs are assembled into a complete event by the Builder Unit (BU). The complete events are then sent to the Filter Unit (FU) to apply the high level trigger to achieve further rate reduction, i.e., down to 1 kHz. This is achieved by the use of *trigger paths* that are multi-step processing algorithms, performing both reconstruction and refinement. The system is designed in a way that would enable fast decision making; succession of steps of reconstruction and filtering in increasing order of complexity. If an event fails to fulfill any of the (roughly) 500 trigger paths is then discarded as soon as possible with an average of 50 ms. Events that pass this final selection are sent to the CERN computing centre called Tier 0 for long term storage and offline reconstruction.

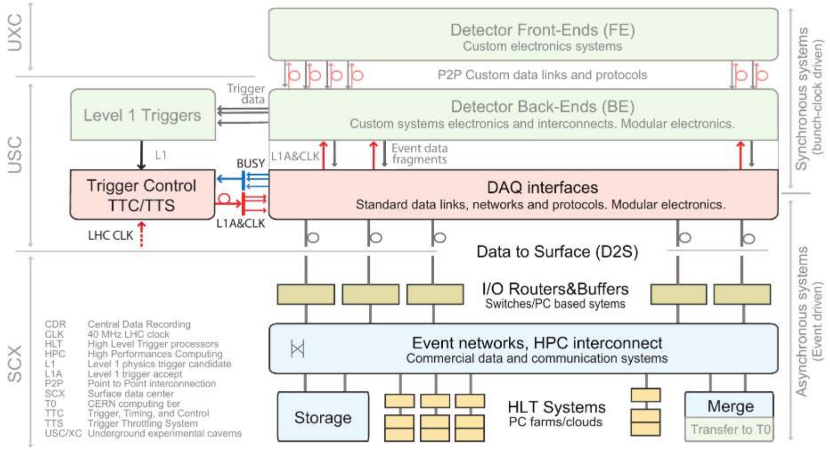

Figure 2.11. | Schematic representation of the DAQ and HLT system. From Ref. [25].

2.3. Data reconstruction and enhancement techniques

As described in Section 2.2, the events that pass the HLT are encoded into a raw format and stored to disk for offline analysis. This raw format contains low level information that would not allow for data analysis. To perform offline analysis and extract results, high level objects associated to particles have to be reconstructed. In CMS, this is achieved via a method that combines information from various sub-detectors and applies specific algorithmic processing called the Particle-Flow (PF) [26]. This section aims to describe the aforementioned multi-step process, starting from tracks and vertices and arriving at the reconstruction of different physics objects.

2.3.1. Tracks and vertices

Track reconstruction at CMS happens in two major phases: first a local reconstruction and then a global reconstruction. Local reconstruction deals with the signals recorded in the pixel and strip trackers to firstly cluster them into hits. Then, global reconstruction deals with groups of these hits to convert them to global coordinates and to finally reconstruct the tracks.

Local reconstruction

In the pixel detector's data acquisition system, zero-suppression is carried out in the readout chips, where adjustable thresholds are applied to each pixel. Offline, clusters of pixels are formed by grouping adjacent cells, including both side-by-side and corner-by-corner connections. Algorithms are employed to determine the position of these pixel clusters.

In the silicon strip tracker, the local reconstruction process operates as follows. The signal from each strip is shaped in its corresponding APV25 channel. The Front-End Drivers (FEDs) offer different formatting options for the raw data: *Scope mode* that captures the raw data within a configurable time window, primarily used for detector commissioning, *Virgin Raw* that provides digitized pulse height data from the sensors, used for testing, commissioning, and calibration purposes, *Processed Raw* that reorders the data to match the strip order and subtracts pedestals, *Zero-suppressed* that the standard operating mode where a configurable threshold is applied to the signals, along with subtracting pedestals and common-mode noise, and *Zero-suppressed lite* that is similar to zero-suppression but with reduced information, designed for high luminosity data taking.

The raw data output from each FED contains the essential hit information for tracking. Zero-suppression is the default operation mode for pp collisions. The raw data is then unpacked to interpret and extract strip information (known as digis). After unpacking, neighboring digis are grouped together using a dedicated clustering algorithm. This process aggregates them into clusters, which are then transformed into potential hit measurements using a cluster parameter estimator algorithm [27]. These hits are assigned a position and corresponding uncertainty in a local orthogonal coordinate system within the plane of each sensor and with this information, global track reconstruction can be performed.

Global reconstruction

The position information coming from the clusters is then used to build particle tracks. However, this approach is spoiled by certain factors including *fake tracks* (especially under high particle multiplicities). A method called Combinatorial Track Finder (CTF) [28] is used to perform the track finding. This is an iterative method aiming to identify tracks starting by the easiest and iterating on the hits that the previous iteration failed to associate to any tracks. The CTF can be described in four main steps:

Seed generation uses the innermost tracker layers to provide track candidates found initially by using 2 or 3 hits.

Trajectory building begins with a rough estimate of the track path provided by the seed, extrapolation by the Kalman Filer (KF) [29] method. Then by scanning the successive detector layers, track candidates are built and checked for compatibility with the extrapolated track path. If such hits are found then the track parameters are updated. This is repeated until no valid hit is found. For electrons, given that they radiate a significant portion of their energy through bremsstrahlung, the energy losses are highly non-Gaussian in nature. The KF method mentioned above relies on uncertainties being Gaussian, therefore an alternative is needed. A modified KF filter has been developed for this purpose, called the Gaussian Sum Filter (GSF) [30].

Track fitting, once the trajectory is built, extracts the best possible estimate of track parameters: d_0, z_0, ϕ_0, θ, p_T;

- d_0 : distance in the transverse plane between the origin and the point of closest approach between the track;
- z_0 : longitudinal coordinate of impact point;
- ϕ_0 : azimuthal angle of the track at impact point;
- θ : polar angle of the track;
- p_T : the transverse momentum;

Track selection makes the final selection on track candidates as the track of a charged particle can be built by different seeds or a given seed can develop into more than one track candidate. To make the selection, the fraction of shared hits between two track candidates is calculated:

$$f_{shared} = \frac{N^{hits}_{shared}}{min(N^{hits}_1, N^{hits}_2)} \tag{2.7.}$$

where N^{hits}_1 and N^{hits}_2 are the number of hits used in building the first and the second track candidate, respectively. If this fraction exceeds the value of 19% (determined empirically), the track with the fewest hits is removed; if both tracks have the same number of hits, the track with the largest χ^2

value is discarded. The procedure is repeated iteratively on all pairs of track candidates [31].

The position of the pp collisions within a bunch crossing can be estimated by the reconstructed tracks of the charged particles. In a given pp collision, the tracks of the particles originate from a common point called *vertex*. The vertex containing the hard process, coinciding with the interaction point of a pp collision is called the *primary vertex*. The vertices emerging from the tracks of particles that decay within the detector volume are then called the *secondary vertices* and they are displaced from the primary vertex due to their relatively long lifetime. Vertex reconstruction can be done by using the available reconstructed tracks in three steps: selecting a set of tracks that pass a quality criteria, clustering of the tracks that originate from the same vertex, and fitting for the extraction of the position of each vertex.

2.3.2. Object reconstruction

As mentioned in 2.3, particle candidates are generated by the PF method by combining the track and calorimeter deposits throughout the detector. In a similar fashion to track and vertex reconstruction, energy deposits in the calorimeters are reconstructed as clusters, independently for every sub-detector. First, energy deposits (or seeds) that are above an energy threshold are found and grown into topological clusters. A Gaussian mixture model then generates clusters from the topological clusters.

Once the tracks, vertices, and calorimeter deposits are there, the task is then to correlate these measurements to define particles, along with their kinematic properties, that are present in the event. This is done via PF blocks where a PF block is defined as a set of objects that can share a common origin, e.g., the extrapolated track of a particle in the inner tracker and the center of a calorimeter deposit are aligned. In a recorded event, each PF block is run through a sequence of particle flow identification. This starts with muons, then electrons and isolated photons, then charged and neutral hadrons, and finally the Missing Transverse Energy (MET). The PF elements used at each iteration of the sequence are removed from the block. Once an object is identified, it can be classified into different categories (with varying efficiency and purity) called working points (WPs).

Muon reconstruction

Muons are minimum ionizing particles (MIP) that are the only charged particles that traverse the whole CMS detector and therefore leaving hits in the tracker, energy deposits in the ECAL and HCAL, and hits in the muon chambers. Their reconstruction starts by evaluating their isolation. This is done by defining the scalar sum of the transverse energy and momentum of any track or calorimeter deposit within a cone of radius ΔR, where ΔR is usually 0.4. If the sum is larger than the 10% of the transverse momentum of the candidate, then the muon is considered non isolated. In the cases where the isolation criteria is not met, the candidate has to fulfill additional conditions not to misidentify punch through hadrons as muons. The additional conditions for this selection are requiring additional hits compatible with expectations from a muon in the inner tracker, muon chambers, and calorimeter deposits.

The muon momentum reconstruction relies on the fit of its trajectory and four application-specific fitters are used: the *inner tracker fit* for muons with $p_T <$ 200 GeV using only the track information from the silion tracker, the *Tracker-Plus-First-Muon-Station fit* for more energetic muons using both the tracker and the muon chambers, the *picky fit* in the cases of showers in muon chambers using only the high quality, compatible hits, and the *dynamic-truncation fit* in the cases with large energy losses on the muon trajectory by performing an inside-out fit from the closest inner tracker layer to the nearest segment in the muon chambers. The choice of the fit among the four is made by an algorithm called Tune-P based on the goodness of fit and associated uncertainties.

After the muon is identified and its momentum is measured, the object is then subjected to further selections to be classified under a WP. Three WPs are defined: muons originating from the PV as well as from the leptonic decays of hadrons in the detector volume pass the Loose WP criteria, muons originating from the PV only, leaving at least six hits in the inner tracker (at least one from the pixel detector), and having a matching segment in the at least two muon stations pass the tight WP criteria, and muons having an intermediate set of criteria pass the Medium WP. How medium WP leads to higher efficiencies can be seen in Figure 2.12.

Electron and Photon reconstruction

Both electrons and photons are particles that interact electromagnetically and they are related through phenomena such as bremsstrahlung and electron-positron pair creation. Therefore they are considered together when reconstructing events. Similar to muons, their isolation criteria is based on the transverse energy sum of all charged particles and calorimeter deposits within a cone of $\Delta R = 0.3$. Electron identification is based on GSF tracks where the PF-associated ECAL cluster that is linked to at most two tracks. Whereas for photons, they are built solely from ECAL deposits that are not associated to any tracks. For both particles, the associated HCAL deposits are required to be small. In the cases where it's not small, then a correction factor is applied, depending on the E_T and η of the cluster.

On any given analysis, the backgrounds can yield non-prompt electrons from secondary electrons produced from photon conversion, misidentified jets, or

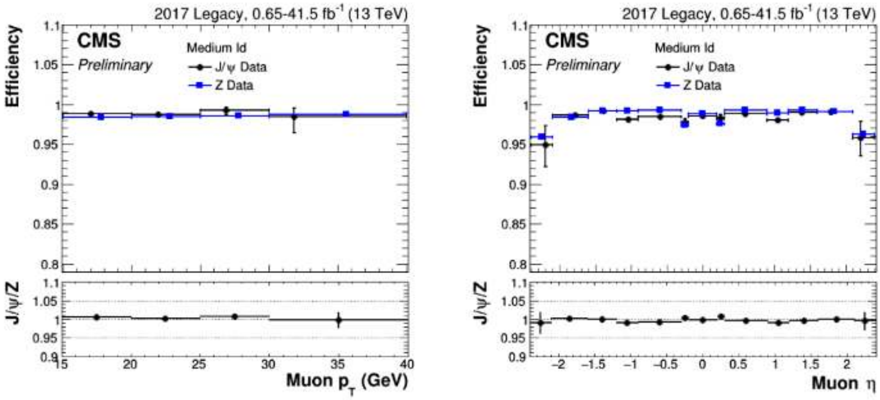

Figure 2.12. The medium WP evaluated on 2017 dataset using a Tag-and-Probe (T&P) method, as a function of the transverse momentum (left) and pseudorapidity (right). From Ref. [32].

electrons coming from b or c decays. Further selections are therefore applied to provide WPs for prompt electrons. This is achieved by two methods: the cut-based method and the multivariate analysis method (MVA). The cut-based method uses several track parameters along with ECAL cluster parameters on simulated $t\bar{t}$ events. The MVA method uses a Boosted Decision Tree (BDT) trained on simulated Drell-Yan+jets sample. See Figure 2.13 for a comparison of the two methods. The idenfication of photons is performed by either cut-based or MVA methods. However, since they have no track information, their idenficiation is based on the shape of the energy deposit, the ratio between ECAL and HCAL deposits, and isolation parameters.

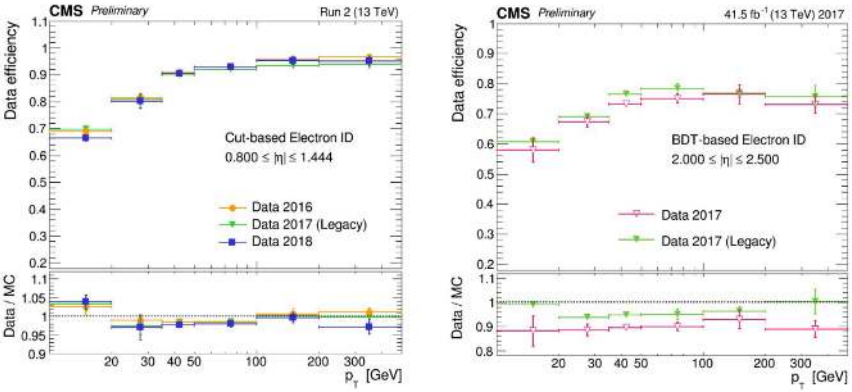

Figure 2.13. Performance of the cut-based (left) and BDT (right) methods as a function of the transverse momentum. From Ref. [33].

Jet reconstruction

Jets are collimated clusters of particles that are formed after the hadronization of the partons resulting from ample amounts final-state radiation following a collision. This cluster of particles can be considered as a spray of particles that form a geometrical cone. Their identification starts after removing the PF blocks concerning muons, electrons, and isolated photons from the PF so that the hadrons can be extracted from the remaining items.

Two thirds of the jet energy is carried by charged hadrons while the remaining energy is carried by neutral particles, i.e., photons or neutral hadrons. Hadron identification is therefore made by using both HCAL and ECAL deposits along with tracks. The calorimeter clusters with no associated tracks are either interpreted as photons (if the cluster is from ECAL) or neutral hadrons (if the cluster is from HCAL). While inside the tracker acceptance, charged hadrons can be defined by associating calorimeter clusters to the tracks. However, outside the tracker acceptance, ECAL-only blocks are interpreted as photons and blocks involving items both from ECAL and HCAL are interpreted as single hadron candidates. After the PF objects are identified as described above, jet clustering is performed via an algorithm called anti-k_T [34] with a radius parameter of R= 0.4 (AK4 jets) or R= 0.8 (AK8 jets). Given the high rate of collisions, pileup mitigation becomes paramount to remove contributions from the underlying event while reconstructing a jet. One of the techniques proving very efficient is the Pile-up Per Particle Identification (PUPPI) [19].

There are therefore three ways that jets can be reconstructed: *calorimeters jets*, reconstructed from calorimeter deposits, *jet-plus-track jets*, reconstructed calorimeters jets with energy response and resolution improved by incorporating tracking information, *particle flow jets*, reconstructed by clustering the four-momenta of the PF candidates (resulting in a significant improvement in momentum and spatial resolution with respect to calorimeter jets). Two corrections are applied to the reconstructed jets: Jet Energy Scale (JES) which is a simulation based correction to account for the bias due to the reconstruction and to remedy an energy offset coming from pileup, Jet Energy Resolution (JER) that is to account for the difference in resolution between the real and the simulated detector.

At the LHC, jets can originate from multiple objects, e.g., heavy-flavour quarks or hadronic τ leptons. The jets originating from b quarks can be of special interest to SM studies, in particular Higgs boson pair production studies, as ***b-tagging*** can serve as a very powerful tool in suppressing backgrounds (Higgs boson and top quark's decays involve b quarks respectively in 60% and 100% of cases). Regardless of the algorithm used, every jet is assigned a score between zero for light jets and one for jets most likely to emerge from a b quark on which the user can define cuts. This cut then defines what WP the object falls into; loose, tight, or medium. Most common algorithms are the Combined Secondary Vertex (CSV), deepCSV, and recently emerging deepJet algorithms [35], [36].

Missing transverse energy

In a collision environment, the presence of neutrinos originating from the decay of W bosons or hadrons or other weakly interacting neutral particles escape the detector without leaving any trace. Their detection is therefore impossible. There is however a way to infer the kinematic properties of these particles by using the imbalance in the total measured transverse momentum in an event. On any given collision, protons travel in opposite direction and the total momentum before the collision equals zero. The total momentum after the collision should then be equal to zero, dictated by the conservation of momentum. However, the collision debris travel in the beam pipe undetected after the collision, it's only the neutrino or the undetected particle's total transverse momentum, $\vec{p}_T^{miss}$, that can be recovered.

$$\vec{p}_{\mathrm{T}}^{\,\mathrm{miss}} = -\sum\nolimits_i \vec{p}_{T,i}, \tag{2.8.}$$

where $\vec{p}_{\mathrm{T}}^{\,\mathrm{miss}}$ is also referred as the E_T^{miss}, Missing Transverse Energy (MET).

2.3.3. Analysis methods

Sections 2.3.1 and 2.3.2 describe how the CMS detector records collision data and reconstructs higher level objects to be used in the searches for wide variety of physical phenomena: measurement of standard model properties or searches for new physics. These searches aim at analyzing CMS data to extract statistical results and they follow a common analysis strategy which is shaped around distinguishing the desired phenomena from the overwhelming backgrounds emerging from the high radiation collision environment. This common strategy can be grouped under three major topics: simulating physics, data enhancement, and statistical analysis. This section gives an overview of these topics in a general manner rather than a case-specific one in the aforementioned order.

2.3.3.1. Simulating physics

Simulated physics serves as a multi-purpose handle on the modelling of any analysis performed at CMS by providing efficiencies, acceptances, prediction of number of expected events which are all crucial in interpreting the data recorded. The simulation chain starts with event generation that is achieved by event generators such as `MADGRAPH` [37] or `POWHEG` [38–40] that provide a precise theoretical modelling of the hard interactions. After the event generation, the

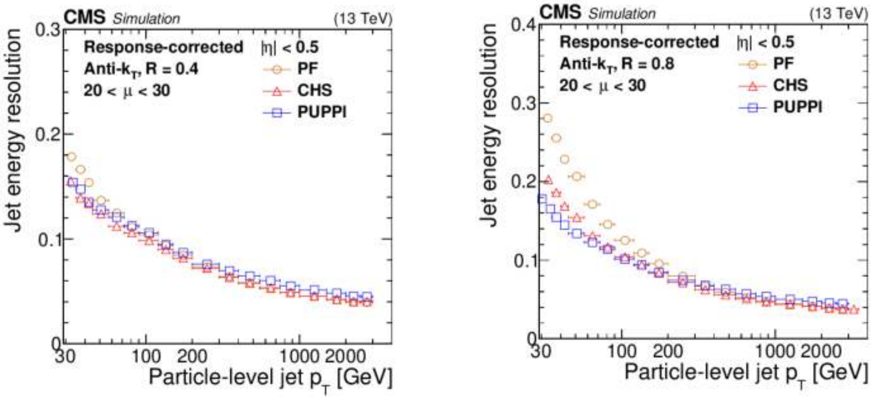

Figure 2.14. | Jet energy resolution for the jets built with different methods; PF, PUPPI, and Charge Hadron Substraction (CHS) for AK4 jets (left and AK8 jets (right). From Ref. [19]

parton shower and hadronization are performed with Pythia [41, 42].

Once the generator level particles are produced, the next step is to emulate the detector response, i.e., the propagation of the generator level particles throughout the detector as similar to the real LHC events as possible. At CMS, this is performed in two ways; full simulation and fast simulation.

Full simulation

This method requires a precise description of the CMS detector comprising both its geometry and materials. This is achieved via the simulation software GEANT4 [43] that is implemented in the CMS framework CMSSW. Full simulation starts with simulating the interactions of all particles with the detector material (including electronics, support structures, and cooling pipes) and the energy deposits they invoke using a Monte Carlo (MC) technique. The energy deposits are then converted into detector hits. This step in the MC generation is called GEN-SIM. The hits, as it would happen in real-time LHC environments, are expected to create a response in the read-out electronics. Digitization step is where this response is simulated. This is followed by the imposition of the presence of pileup in a step called pileup mixing by using mimimum-bias events. Although full simulation proved to be a reliable and ever-growing tool, it is computationally intensive and therefore requires the use of extensive computing resources.

Fast simulation

The requirement for an expertise and deployment of extensive computing resources poses a problem in certain cases such as phenomenology studies or prospective analyses where the level of complexity delivered by full simulation is not necessarily needed. To face this problem, several fast-simulation techniques that are two to three orders of magnitude faster than full simulation have been developed by the LHC collaborations. These techniques are based on a simplified approach based on the parametrization of the detector response. One of the frameworks achieving this is called the DELPHES [44] framework. The analysis described in this thesis deployed samples that are generated by DELPHES. The event generator output is given as an input to the framework to perform a fast and realistic simulation of the CMS detector. Long-lived particles emerging from the hard scattering are propagated to the calorimeters. This is followed by the smearing of the initial long-lived particles' momenta according to the detector resolution. Finally, high-level objects that are ready to be used in data analyses are reconstructed, e.g., jets, isolated electrons, muons, photons, and missing transverse energy. Figure 2.15 shows the electron and photon resolution in comparison to the electron gaussian energy resolution from CMS.

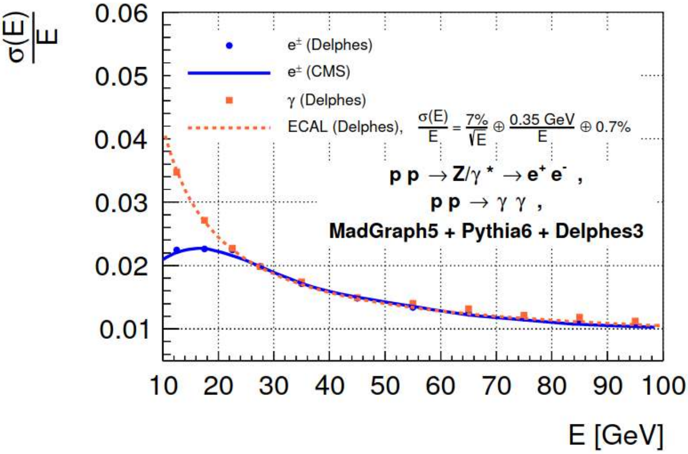

Figure 2.15. | Electron and photon energy resolution as a function of the energy for a CMS-like detector. The electron resolution agrees well between CMS and DELPHES. The electron and photon resolutions match perfectly the ECAL resolution at high energies. However, at low energies the electron resolution is driven by the tracking resolution. From [44].

2.3.3.1. Data enhancement

For any physics data analysis, the search for the desired phenomena starts by defining basic pre-selections on the objects belonging to the expected final states. This cut-based approach already significantly reduces the amount of data in target. However, these pre-selections are in most of the cases not sufficient to provide the optimal signal sensitivity, i.e., they are not sufficient to suppress and reduce background contamination in the signal region (SR) while keeping a high signal purity. One remedy is to reconstruct higher level physics variables such as invariant masses, transverse masses, or angular variables. Propagating the complexity through cuts on these variables can help improve the signal purity in the SR. While doing a physics data analysis, the SR is blinded and the phase space outside of this region (control regions (CR)) is used to ensure good data to simulation agreement. Once the agreement is achieved and systematic uncertainties are well understood, the SR is unblinded and the statistical analysis is conducted.

Already in use for more than two decades, neural networks have been proving more powerful than traditional cut-based methods. With the recent advances in ML and availability of frameworks, possible ML applications enlarged and the ML applications at CMS cannot be put under classification only, however, the growing trend towards the employment of MVA tools and their application in terms of signal sensitivity optimization is of interest for this section. These tools are carefully crafted algorithms that take as an input a set of variables to train on and learn how to discriminate between the backgrounds and the expected signal on simulations. The MVA tools of choice are usually boosted decision trees (BDT) or neural networks (NN). The analysis featured later on in this document employs Deep Neural Networks (DNN) and therefore this section covers only NNs.

Neural networks

Motivated by the formulation of the human neuron activity, NNs are networks of artificial neurons –also called perceptrons – and are a subset of machine learning with a diverse range of applications. In the case of classification, NN approach can be summarized as the following: the quality of classification achieved by the classfier C(x) between $y = 0$ and $y = 1$ can be quantified by a loss fuction L, and the C(x) is found such that the average loss L over the previously defined dataset is minimized.

Each individual neuron of a NN then acts on a linear combination of inputs where the input can be described by weights w_i, a bias b_i, and an activation function ϕ. The output of the neuron is then:

$$y_i = \phi\left(b_i + \sum_j w_{i,j} x_j\right). \tag{2.9.}$$

A NN is constructed by connecting multiple neurons into a layer and then connecting multiple layers into a network. The output described in Eq. 2.9 that is delivered by each neuron in a layer is used as an input for the neurons of the next layer. Figure 2.16 shows an example network with its layers and neurons. If there are layers in an NN that neither receive any input nor deliver any output, they are called the hidden layers. The NNs that have several hidden layers are called Deep Neural Networks (DNN).

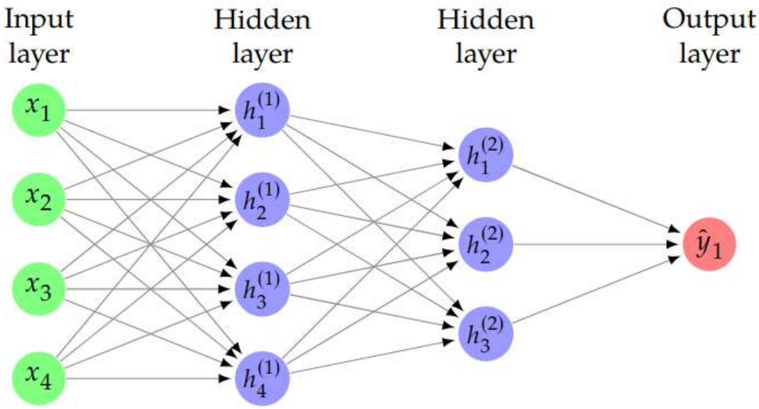

Figure 2.16. | Example of a multi-layer NN with four input parameters, two hidden layers, and a single output neuron.

As mentioned at the beginning of this subsection, C(x) is found such that the average loss is minimum. This requires finding the optimal neuron weights and it is also referred as *training* a network. During the training, at every step, the neuron weights are updated by a small shift in the direction of the steepest decrease in the loss function. All layers of the NN are updated recursively by calculating the gradients of every layer, from the last layer to the input layer. This is called backpropagation and it was a game-changer in the NN history.

2.3.3.1. Statistical analysis

A likelihood ratio based statistical analysis [45, 46] takes place as the last phase of a physics analysis, given that the simulations of the signal and background modelling along with a data enhancement strategy is already in place.

The signal model parameters can then be used to compute the expectations in the different regions of the final discriminant. These parameters are the number of observed events d_i, the number of expected signal events s_i, and the number of expected background events b_i where i denotes mutually exclusive regions, i.e., the individual bins of a histogram in this case. The likelihood is then expressed as a product of Poisson likelihood of measuring d_i given the expectations, over each independent region:

$$\mathcal{L}_{s+b}(\mu) = \prod_i p(d_i|\mu s_i, b_i) = \prod_i \frac{e^{-(\mu s_i + b_i)}(\mu s_i + b_i)^{d_i}}{d_i!} \tag{2.10.}$$

where μ is the *signal strength*, the parameter of interest (POI). In the frequentist approach, a statistical test for the signal presence in analysis regions requires the likelihoods of two hypotheses: the null hypothesis where the signal is absent ($\mu = 0$, background only hypothesis), and the hypothesis where there is both the signal and the background. The ratio of these two likelihoods provide a discriminating test statistic:

$$X_{obs} \equiv \frac{\mathcal{L}_{s+b}}{\mathcal{L}_b} \sim X_{s+b} \tag{2.11.}$$

$$CL_{s+b}(\mu) \equiv p(X_{s+b} < X_{obs}) \tag{2.12.}$$

The confidence level of the signal plus background hypothesis can be computed as the distribution of X_{s+b} is at hand. Next, the confidence level of the background is computed which then used in the Modified Frequentist confidence level; ratio of signal plus background confidence level and background confidence level:

$$CL_b \equiv p(X_b < X_{obs}) \tag{2.13.}$$

$$CL_s(\mu) \equiv \frac{CL_{s+b(\mu)}}{CL_b} \tag{2.14.}$$

The likelihood ratio in Eq.2.14ref used to compute the p-value by comparing toys extracted from the known likelihoods. In the case of the presence of an excess of data, a significance value Z is computed as the number of standard deviations from the null hypothesis:

$$p = \int_Z^\infty \frac{1}{\sqrt{2\pi}} e^{-\frac{x^2}{2}} dx. \tag{2.15.}$$

The discussion above assumes a perfect knowledge of the signal and background, however, this is never the case. The imperfect knowledge of the theoretical predictions and experimental measurements, *the nuisance parameters*, have to be taken account as they will impact the expected probabilities.

3.

Chapter

The CMS Silicon Strip Tracker

The CMS Silicon Strip Tracker (SST) is located the second closest to the interaction point and it surrounds the pixel detector. It provides the track measurement of charged particles together with the pixel detector up to the pseudorapidity range of $-2.5 < \eta < 2.5$. The SST has a total active silicon area of 198 m^2 split into 9.3 million strips distributed over 15148 modules. It is 5m long and has a diameter of 2.5m. The four partitions of the detector are named Tracker Inner Barrel (TIB), Tracker Inner Disks (TID), Tracker Outer Barrel (TOB), and Tracker End-Caps (TEC) and can be seen in Figure 3.1.

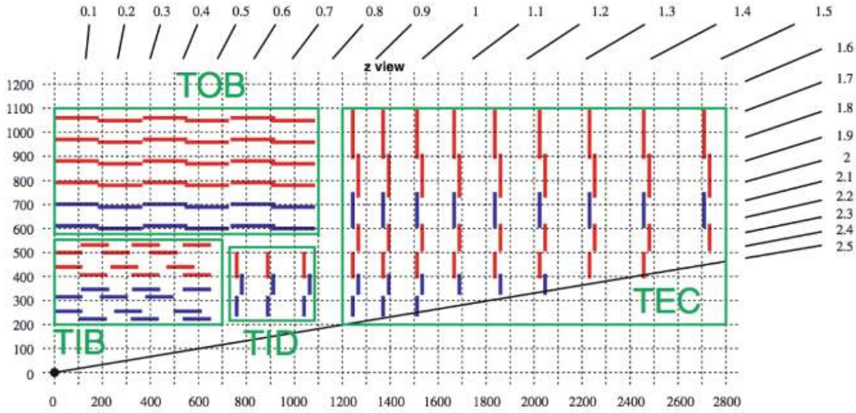

Figure 3.1. | The layout of the silicon strip tracker. From Ref. [47]

3.1. Silicon sensors and modules

The SST is comprised of 24244 silicon sensors whose sensor element is p-on-n type silicon micro-strips of pitch between 85 μm and 205 μm. The sensors have been manufactured on 6 inch wafers with the base material being n doped float zone silicon with $\langle 100 \rangle$ cyrstal orientation. The thickness of sensors differs depending on the partition of the tracker, i.e., TIB/TID and the inner rings of TEC uses thin sensors of 320 ± 20 μm thickness whereas TOB and the outer rings of TEC uses thicker sensors of 500 ± 20 μm thickness. The SST uses 15 different sensor geometries: two rectangular types each for TIB and TOB, and 11 wedge-shaped sensor types for TEC and TID, having either 512 or 768 strips (reflecting the readout modularity of 256 channels). The sensors are manufactured on 6 inch wafers while, for instance, the typical dimensions of the sensors used in TIB and TOB are 6 x 12 cm^2 and 10 x 9 cm^2, respectively.

Of the 15148 sensor modules of the SST, the ones used in TIB, TID and rings 1 to 4 of TEC are equipped with one thin sensor (of thickness 320 μm). TOB and rings 5 to 7 of TEC, however, are equipped with two thick sensors (of thickness 500 μm). Four layers from the barrel and three rings from the endcaps are populated by so-called *stereo modules*; additional modules with sensors tilted at 100 mrad angle. The difference in strips fired in the two modules provides an improved z-direction measurement in the barrel and R measurement in the endcaps. The module design is supported by a main frame made of either carbon fiber or graphite. The insulation of the silicon from the module frame is done by a Kapton foil. This Kapton circuit layer is also used to provide the electrical connection to the sensor back plane. The front-end hybrid and the pitch adapter are carried on the module frame. The total number of different module designs for all four partitions is 29. Figure 3.2 shows an exploded view of the module design along with a photograph of a TEC module.

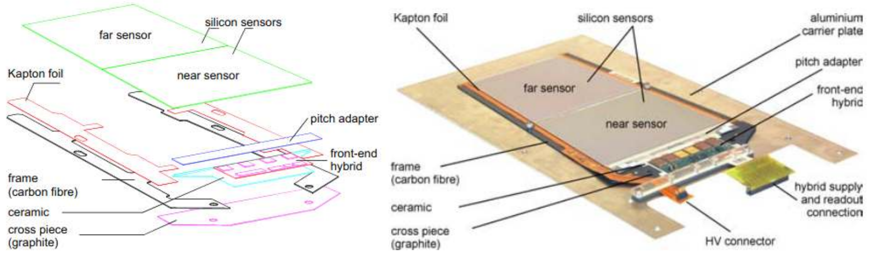

Figure 3.2. | Exploded view of a module housing two sensors (left) and a photograph of a TEC ring 6 module, mounted on a carrier plate (right). From Ref. [20].

3.2. Readout system

The signal produced by the silicon sensors are amplified, shaped, and stored by a custom integrated circuit (IC) named the analogue pipeline voltage (APV25) chip. The APV25 has been designed in an IBM 0.25 μm bulk CMOS process as this sub-micron process ensures radiation tolerance. The pre-amplifier of this ASIC transforms the charge produced into a potential difference. Then, a programmable inverter makes sure the signal input to the 50 ns CR-RC shaper is positive. The output from the CR-RC circuit is then sampled at the LHC bunch crossing frequency of 40 MHz, and stored in the 192 cell deep analogue pipeline. Figure 3.3 shows a schematic of the APV25 with its components.

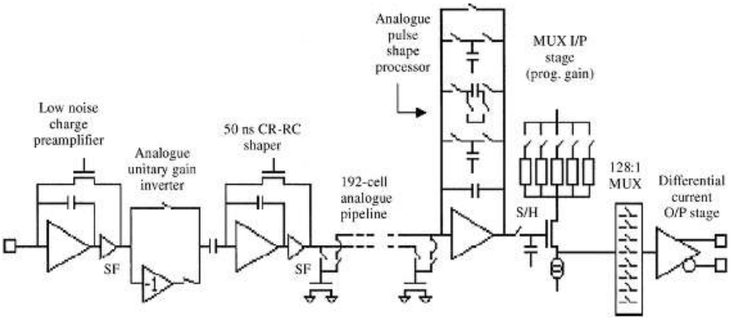

Figure 3.3. | Schematics of the APV25 ASIC. From Ref. [48].

The Analogue Pulse Shape Processor (APSP) has two different readout modes implemented in it. In the *peak* read-out mode, a single pipeline voltage is read-out upon receiving a L-1 trigger accept signal. In the *deconvolution* mode, a weighted sum of three consecutive voltages are read-out. This second mode is needed for high luminosities in order to confine signals to the correct LHC bunch crossing. The read-out chips, APV25, are hosted on a multi chip module called hybrid along with other front-end read-out electronics for a detector module: the APVMUX chip, the PLL chip, and the DCU chip. The hybrids distribute and filter the supply voltages to chips, route clock, control and data lines, and remove the heat from the chips into the cooling system. A total of 12 different hybrid flavours were realized for the SST. The analog signals from the sensors processed by APV25 are then converted to optical signals on analog-opto-hyrbids (AOH) and sent to the front-end drivers (FED). This can be seen in Figure 3.4.

The FED is a VME module that receives data from 96 optical fibres, each corresponding to 2 APV25 chips (or 256 read-out channels) and performs cluster finding and pedestal and common mode substraction. The analogue input data is first digitized by an ADC. Then, the pedestal corrections are applied and the common mode is substracted on an even-by-event basis. The FPGA of FEDs are programmed with a clustering algorithm that outputs a list of clusters with address information for each fired strip, thus passing only the objects of relevance to the central data acquisition system (cDAQ). There are a total of 450 FEDs in the whole of SST. The front-end controllers (FEC) are VME modules that distribute the clock, trigger, and control data to the communication and control units (CCU) that they receive from the global Timing Trigger and Command (TTC) system.

3.3. Tracker Inner Barrel/Tracker Inner Disk

Out of 10 layers of the barrel region of the tracker, the four short layers make up the tracker inner barrel (TIB). These four layers are four concentric cylinders

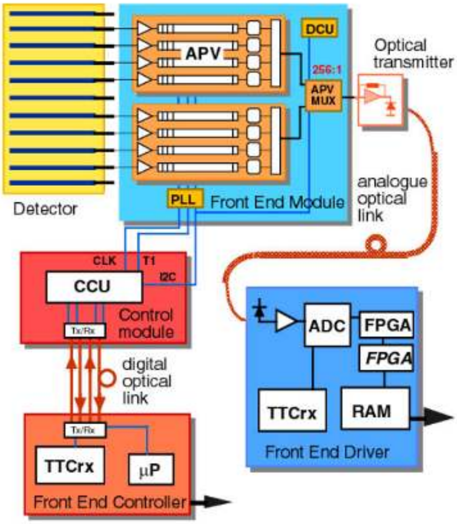

Figure 3.4. | The readout scheme of the SST. From Ref. [20].

placed at radii of 255.0 mm, 339.0 mm, 418.5 mm, and 498.0 mm from the beam axis, respectively. Stereo modules with a pitch of 80 μm are used in the two inner rings while single sided modules with a strip pitch of 120 μm are used in the two outer rings. The ends of TIB± are coupled with two service cylinders that end in a service distribution disk made of conventional G-10 fiber epoxy with 30 μm copper on both sides called the *margherita*. As can be deducted from Figure 3.5, the service cylinders' role is twofold: routing out the services from the shells to margherita and supporting the tracker inner disks (hidden inside the service cylinders).

The three disks that are hosted inside the service cylinders of TIB make up the tracker inner disks (TID). The disks are made of the same carbon fiber material as TIB shells, are identical, and consist of three rings. The TID± is placed in z between ±800 mm and ±900 mm. The TIB/TID structure nests in the TOB volume, is hermetic, and covers a pseudorapidity range of up to $|\eta| = 2.5$. There were two factors taken into account for the cooling aspect of the TIB/TID sub-system: efficient cooling with the coolant temperature down to -25° C and minimal material budget. Therefore the choice of material was aluminium. The aluminium piping used in the TIB/TID is of 6mm cross section and 0.3mm wall thickness. These pipes are bent into loops and soldered into inlet/outlet manifolds where both the dimension and the number of the loops used across the sub-system depend on the heat dissipation of the given layer (single sided modules dissipate much less heat). There are a total of 70 cooling loops in the TIB/TID.

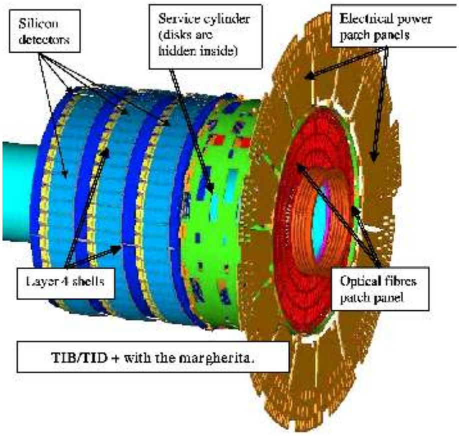

Figure 3.5. | The schematic of one half of TIB/TID structure. From Ref. [20].

Modules have been grouped together electrically to maintain a low number of power supplies where the smallest group consists of three modules while the largest can consist of 12 modules where the modules of the given group are interconnected through a Kapton circuit which ensures the distribution of power and the detector controls. These power groups are fed by a tracker-specific power supply unit (PSU) and are contained within a control ring where control ring is an electrically more complex group which is interfaced by the communication and control unit module (CCUM).

3.4. Tracker Outer Barrel

The 6 remaining layers of the barrel region make up the tracker outer barrel (TOB). These 6 layers form a single mechanical structure called *wheel* comprising 688 sub-assemblies called *rods*. The wheel is 2180 mm long and has an inner radius of 555 mm and outer radius of 1160 mm. Figure 3.7 shows a picture of the wheel where three inner and three outer cylinders can be seen while Figure 3.6. The wheel consists of four identical disks (each having the 6 layers of cylinders) made of carbon fiber epoxy laminate. The sub-assemblies, the rods, are 1130 mm long carbon fiber profiles hosting either 6 (single-sided) or 12 (double-sided) silicon detector modules. The rods are hosted in openings contained on the disks of the TOB where each disk has 344 openings. The single-sided rods populate the four outer layers (3-6) while the double-sided rods populate the two inner layers (1,2). The modules of any given rod (6 or 12) are powered by a single PSU, i.e., they form a power group. The grouping design was made by taking into account two considerations: the recommended limit on CCUMs per ring being 10, avoiding having control rings span across different cooling segments. The achieved average number of CCUMs per ring in the TOB is 7.5.

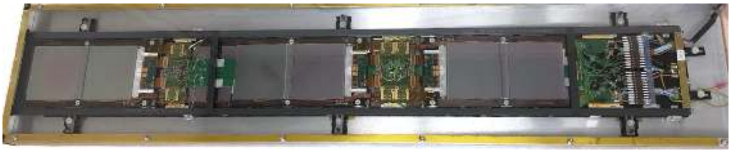

Figure 3.6. | The picture of an assembled TOB rod [20].

Figure 3.7. | The picture of the naked TOB wheel [20].

3.5. Tracker End-Caps

The tracker endcaps complement the barrel detector at both ends with detector planes perpendicular to the beam axis and they extend radially from 220 mm to 1135 mm and along the z-direction from ±1240 mm to ±2800 mm. Each endcap consists of 9 disks where each disk carries substructures that host individual detector modules, as well as two more disks serving as termination disks on both sides. The disks of the endcap are carbon fiber composite (CFC)/honeycomb structures. They are joined together by eight U-profiles, also referred to as service channels, on their outer periphery. On the inner periphery, however, an inner support tube is employed so that each disk is attached to it at four securing points. The disks vary in radii as a result of hosting the pixel detector inside. The first three rings therefore have a smaller radii (229 mm) than the last six disks (309 mm). The substructures that carry the detector modules are called *petals*. They carry a total of 10 different types of modules that are arranged in rings around the beam pipe and they can be individually removed from the endcaps without uncabling/dissasembling the entire structure. Each disk of the endcaps carry 16 petals; eight on the front face and eight on the back face of the disk.

The petals have a 10 mm NOMEX core sandwiched between 0.4 mm CFC skins

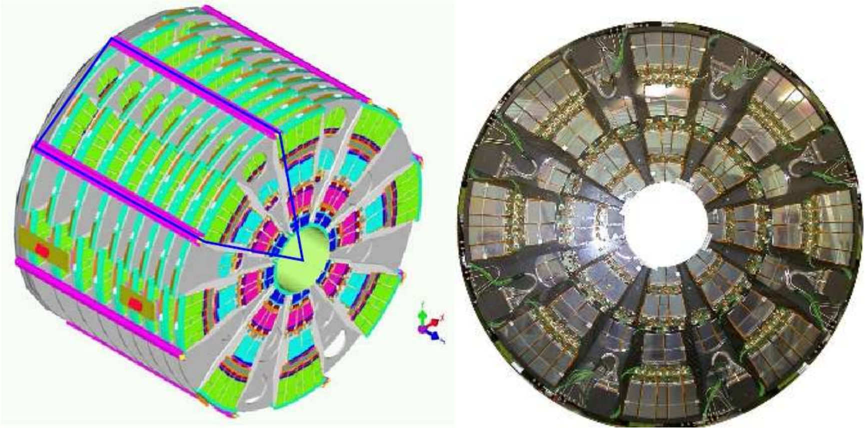

Figure 3.8. | A sketch of one endcap (left) and a photograph of the completed TEC+ (right) [20].

and the cooling of the sensors and hybrids are mainly handled by these CFC skins. The rest of the components, both on the front and on the back of the petal, are cooled by the cooling pipes (each petal contains two cooling circuits) traversing the petal longitudinally. The pipes are made of titanium with an outer diameter of 3.9 mm and a wall thickness of 0.25 mm.

The petals carry motherboards named InterConnect Boards (ICBs) that the AOHs and CCUMs are connected to. These ICBs transmit the LVDS and I^2C signals, bring the ground, distribute the various supply voltages and the bias voltage to the electrical components on the petal. Electrical grouping of the modules are done in a way such that there are three low voltage (LV) groups and that for each LV group there are two high voltage (HV) channels provided. Furthermore, for each HV channel there are up to four single HV lines. One front petal and one back petal are connected in a control ring, where the front is the first in the control loop.

A 5 cm wide and 150 μm thick copper ring serves as the termination ring and is glued on the outer radius of each back disk of the endcaps. They are connected to the hadron calorimeter (through the tracker support tube) which is a very solid ground. Therefore, these disks serve as the TEC common ground. The CF skins of the disks and petals, the reference points of all power groups, the shields of all cables, and the outer aluminium shields of the TEC are connected to this common ground.

3.6. Detector Status and Performance by the end of Run 2

After ten years of operation between 2008 and 2018, the CMS strip tracker performance is still outstanding with a 96.2% fraction of active readout channels.

The monitoring of the strip tracker is done through a set of metrics quantifying the performance of the detector. Two of these metrics are the signal to noise ratio (S/N) and the single hit efficiency. The signal to noise distributions are used to fit a Landau convoluted with a normal distribution, from which the most probable value (MPV) is extracted as an estimation of the S/N. Figure 3.9 shows the signal to noise distributions for TIB and TOB.

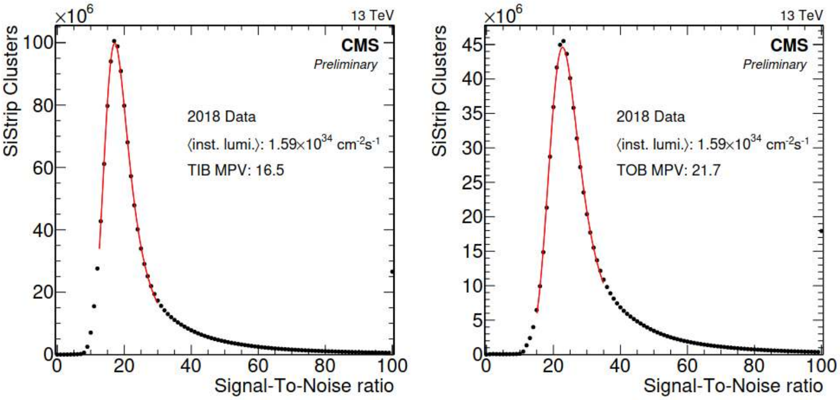

Figure 3.9. | Signal to noise distribution for hits on reconstructed particle tracks for TIB (left) and TOB (right). From Ref. [47].

Furthermore, the S/N drops with the integrated fluence as expected from the irradiation studies. Figure 3.10 shows how the signal to noise ratio evolves with increasing integrated luminosity which then allows for an estimation that indicates the S/N will be sufficient for high quality physics data taking during foreseen operation time of the detector. As can be seen on Figure 3.10, single hit efficiencies remain above 98% and depend on the layer of the detector as the difference in the probability of highly ionizing particles (HIP) passing through the sensors. This causes a significant inefficiency which can be tracked on the high luminosity region of the right plot of Figure 3.10. The decrease in the hit efficiency is mainly resulting from the secondary particles from the collisions saturating the read-out chip and rendering the chip blind in the meanwhile.

Sitting in a very high radiation region, the tracker is continuously monitored in terms of radiation effects. The two crucial effects are the increase in leakage current and the change in the full depletion voltage of the sensors.In 2017, this lead to some modules coming close to the current limit of the power supplies. The fact that the modules affected by this issue being located in a region with passive cooling (degraded cooling contacts or closed cooling loops) allowed for thermal runaway, a positive temperature-current feedback loop. This was handled by reducing the bias voltage to 200 V. Also in 2017, the operational temperature of the tracker was changed to -20°C as keeping it at -15°C would mean reaching the power supply current limit in the regions with passive cooling. The operational temperature of the detector further decreased to -25°C during long shutdown 2 (LS2) between 2019-2022, the detector was then re-calibrated and commissioned to start data taking in Run 3.

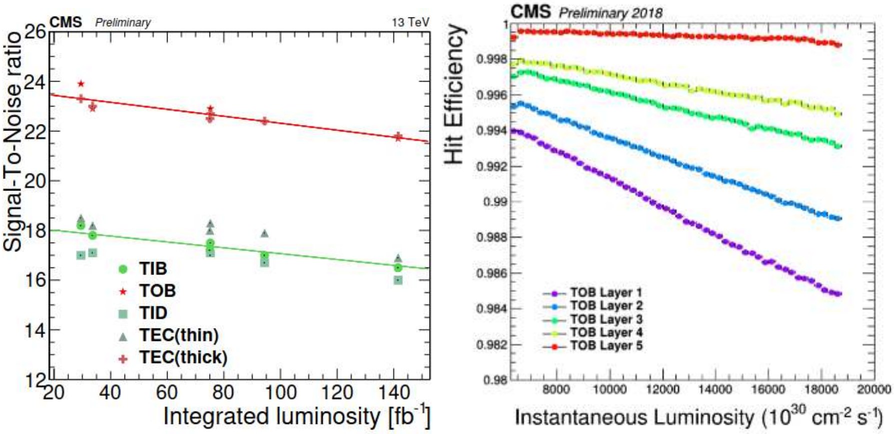

Figure 3.10. | The evolution of the run-2 S/N in the different detector partitions as a function of integrated luminosity (left) and single hit efficiencies as a function of the instantenous luminosity, as seen during the 2018 data-taking period (right). From Ref. [47].

It is safe to say that after ten years of operation the CMS Strip Tracker has been performing very well by the end of Run 2 (2018), showing no crucial degradation. At the time of writing, there has been a long shutdown (LS2) of the LHC complex to accommodate the installation of the upgraded subsystem such as the Phase-1 upgrade of the HCAL. Following LS2, in July 2022, the third run of the LHC started and delivered proton-proton collisions at the center of mass energy of 13.6 TeV. The tracker performance should continue to be outstanding for the remainder of Run 3 data taking with the greatly increasing luminosity (500 fb^{-1}).

4. Chapter

The CMS Experiment at the HL-LHC

This fourth introductory chapter will cover the details of the upgrade that the LHC and the CMS will undertake after the completion of Run 3, which at the moment of writing of this dissertation completed its first era. Since the beginning of its operation, the accelerator recorded copious amounts of data which then yielded numerous discoveries and more than a thousand publications in referred journals. This, however, does not change the fact that, to this day, many physics analyses suffer from the lack of statistics: a major example is the Higgs pair production among many other physical phenomena we want to observe at the LHC. In pursuit of the observation of a broader range of physics, it was decided that the accelerator will be operated at higher luminosities and hence the name High Luminosity LHC (HL-LHC).

This following section will describe the technical details and the timeline of the upgrade, followed by an overview of the detector upgrades to the CMS sub-systems. The third section of the chapter will go through the tracker upgrade with greater detail on the outer tracker upgrade, which stands to be one of the two main topics of this dissertation.

4.1. The High Luminosity LHC

When the CERN Council adopted the European Strategy for Particle Physics in Brussels on 30 May 2013, its first priority was agreed to be “the exploitation of the full potential of the LHC, including the high-luminosity upgrade of the machine and detectors with a view to collecting ten times more data than in the initial design, by around 2030 ” [49]. This decision was derived by the fact that unless there is a significant increase in luminosity, the statistical gain in running the accelerator becomes minimal; we would need to run the accelerator for more than ten years only to half the statistical error in the measurements made until 2019. In this pursuit, the target luminosity for this phase of the LHC lifetime is set to 5×10^{34} $\mathrm{cm}^{-2}\mathrm{s}^{-1}$ of instantaneous luminosity leading to an integrated luminosity of 250 fb^{-1} each operating year. Resulting in total integrated luminosity of 3000 fb^{-1}, HL-LHC will have increased the design (integrated) luminosity by an order of magnitude. This levelled luminosity will serve as an unprecented portal for the weak-scale nature of the universe, making it possible to probe physics sectors such as Higgs precision measurements or quantum nature of dark matter.

We will start by introducing the physical concept behind increasing the luminosity by making use of Eq. 2.2 for the instantaneous luminosity. As it can be deduced easily from the equation, a straightforward way to increasing luminosity is to reduce β^*. The drawback to this action is that smaller β^* requires larger crossing angle which then brings a reduction on the geometrical factor R from the Eq. 2.3, see Figure 4.1.

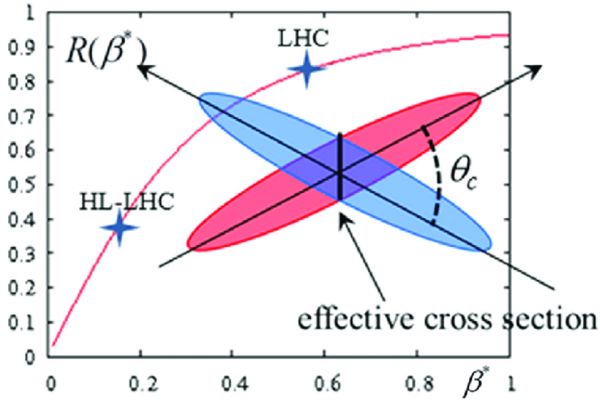

Figure 4.1. | Effect of geometrical reduction factor on luminosity plotted against β^* with two operating points shown: nominal LHC and HL-LHC. The sketch of bunch crossing shows the reduction mechanism. From [50].

To compensate for the adverse geometrical effect resulting from β^* reduction, the beam bunches need to be rotated as to guarantee they do not suffer from the reduction in beam overlap due to increased θ_C. An efficient solution to this is applying a torque to the beams to rotate each bunch by $\theta_C/2$ so that they collide head on. This is achieved via crab cavities that are specical radiofrequency (RF) cavities that are capable of generating transverse electric field and are located on each side of the interaction point. The method has proven to be working successfully in supressing the geometrical reduction at the BELLE experiment at KEK. Figure 4.2 shows how crab cavities rotate the beams and ensure a head on collision.

Figure 4.2. | Sketch of bunches colliding in a regular accelerator on the left, and with the introduction of crab-cavities to the right. From [51].

The implications on the hardware aspect of the upgrade involves both the LHC machine and its injector complex. The upgrade of the latter was designed and implemented within the LHC Injectors Upgrade (LIU) [52, 53] project during the long shotdown 2 (LS2) [54]. The main goal of LIU was enabling the injector chain to double the intensity and brightness of the beams supplied to the LHC main ring. The major changes to the individual components of the injector complex starts with the replacement of the LINAC2, which injected protons into the PSB until 2018, with the LINAC4 [55] which, unlike its predecessor, accelerates H- ions up to an increased energy of 160 MeV. The PSB had to be modified to accommodate a new injection region to enable the H- injection at 160 MeV instead of the 50 MeV multi-turn proton injection from LINAC2, allowing for higher brightness beams. Upgraded RF and power supply systems enabled PSB beam extraction at higher energies which leads to an increased energy output to PS at 2 GeV instead of 1.4 GeV. Lastly, the main 200 MHz RF system of the SPS was upgraded to keep up with the increased beam intensity.

The second part of hardware upgrades, the upgrade of the LHC machine itself, is planned to be implemented during the LS3 which, at the time of writing of this dissertation, is planned to take place between 2026 and 2028. The full technical details of the LHC upgrade is given in [51]. The major hardware changes within this upgrade are the replacement of the insertion magnets that are responsible for squeezing the beam at collisions and the installation of crab cavities. The new magnets benefit from the success of the Nb_3Sn technology in surpassing the limits of Nb-Ti based magnets (they cannot surpass 9 T in magnetic field strength). Therefore, the quadrupole triplets will be replaced by Nb_3Sn quadrupoles. To allow for lower operational temperature and higher heat evacuation, the cryogenic systems will be replaced.

	LHC Design	HL-LHC baseline	HL-LHC ultimate
Peak luminosity ($\times 10^{34} cm^{-2} s^{-1}$)	1.0	5.0	7.5
Integrated luminosity (fb^{-1})	300	3000	4000
Number of pileup events	~ 30	~ 140	~ 200

Table 4.1. | Projected HL-LHC operating parameters.

4.2. The CMS Upgrade for the HL-LHC: CMS Phase-2

As described in Section 4.1, HL-LHC will reach unprecedented luminosities creating a very harsh radiation environment and much higher pile-up levels. The current detectors are far from being sufficient to keep up with the increased data rate in terms of bandwidth and granularity, neither in the event selecting efficiency, i.e., trigger. Specifically, the CMS tracker is reaching its end-of-life because of radiation damage. A very broad upgrade program will be conducted by the CMS experiment to replace and improve the whole of the detector system making this upgrade the second of the two-phased upgrade program, therefore the name CMS Phase-2. This section will give an overview of these upgrades whose details can be accessed at length in the technical design reports from Ref. [21, 56–60]. The tracker upgrade will be treated the last, providing deeper detail on the outer tracker upgrade.

4.2.1. Trigger and DAQ Upgrade

The two level strategy of the current trigger that is described in Section 2.2.7 comprises the L1 trigger, the custom hardware that is on the detector level, and the HLT, performing the rate reduction and operating on software level. The Phase-2 trigger system will use the same two level strategy but with an entirely new set of trigger and DAQ system that can allow a maximum L1A rate of 750 kHz. While the current L1 trigger latency is 3.4 μs, the upgraded L1 will have a latency of 12.5 μs which corresponds to 500 LHC bunch crossings. Another major change in the trigger system is that the system is currently being input trigger primitives from calorimeters (ECAL and HCAL) and muon chambers (CSC, DT, and RPC) only. However, phase-2 trigger will include central tracking information as well as the high granularity calorimeter information which will improve track matching to calorimeter deposits. The proposed L1A rate is 500 kHz for beam conditions yielding an average pileup of 140 which would allow CMS to maintain the typical Phase 1 trigger. The case with an average pileup of 200, however, requires a rate of 750 kHz to achieve a comparable performance to Phase 1.

The current event size of 2.0 MB is expected to increase to 7.4 MB because of high granularity that is targeted and the high rate of events that needs to be read out. The read out data rate is expected to be up to 50 Tbits^{-1}. To accommodate this high rate, the DAQ system will go through an upgrade such that each BE module will asynchronously transfer its accepted data to a DAQ concentrator where it will be collected before being sent to the surface through standard protocols into the Event Network. The Event Network, a high performance network of commercial processors, will then assemble different fragments into a complete event. As soon as the event is built, it will be stored in a buffer while waiting for an available HLT processor that will perform the reconstruction and the final event selection. It is expected that the bandwidth and the computing power required for the upgraded HLT system will be about 10 (15) and 15 (30) times higher than the existing system for operation at a pileup of 140 (200) [49].

4.2.2. The MIP Timing Detector

A major issue with high pileup collision environments is that the task of reconstructing the primary vertex gets complicated and an overall degradation in reconstruction performance is expected if the detector system is kept at the current design. A solution was proposed to overcome this challenge by the addition of a new sub-detector: the Minimum Ionising Particle Timing Detector (MTD). The main purpose of the detector is assigning precise timing information to the identified tracks with an initial resolution of 30-40 ps at the beginning of operation and degrading under radiation damage to 50-60 ps by the end of HL-LHC operation.

After considerations of mechanical constraints, performance, radiation tolerance, and cost, the detector design converged on a thin layer between tracker and calorimeters that is divided into a barrel region with the coverage $|\eta| < 1.5$ and two endcap regions with coverage up to $|\eta| <= 3.0$. The barrel region is called the Barrel Timing Layer (BTL) and the endcap regions are called the Endcap Timing Layers (ETL). The BTL design employs scintillator rods carrying LYSO:CE crystals that are coupled with SiPMs on both sides. The SiPMs are read out by custom ASICs called TOFHIR, time-of-flight high rate. The endcap region, however, has much higher occupancy and radiation levels which eliminates SiPMs for the task. The technology chosen for the task are planar silicon devices with internal gain, the Low Gain Avalanche Detectors (LGAD). The LGADs are read-out by custom ASICs called Endcap Timing Readout Chips (ETROCs).

The mechanical design of the detector allows interventions during technical stops for potential repairs and the improvements it will provide are numerous, e.g., b-jet identification, lepton isolation, missing transverse momentum.

4.2.3. Calorimeter Upgrade

As described in Sections 2.2.3, 2.2.4, the CMS electromagnetic and hadronic calorimeters are designed hermetically, providing a coverage within $|\eta| < 5$. Serving for the identification and reconstruction of photons, electrons, jets, and missing transverse momentum, the calorimeters were designed to meet harsh radiation conditions of integrated luminosity of up to 500 fb^{-1} over 10 years of data taking at an instantaneous luminosity of $1\times10^{34}\mathrm{cm}^{-2}\mathrm{s}^{-1}$. After the Phase 1 upgrade of the hadron calorimeter [61], the detector is now capable of operating at luminosities up to $2\times10^{34}\mathrm{cm}^{-2}\mathrm{s}^{-1}$. However, the HL-LHC operating parameters listed on Table 4.1 indicates that an upgrade to the whole calorimeter complex is necessary.

Barrel Calorimeters

The HCAL barrel upgrade that took place during the LS2, (see Section 2.2.4), proved that performance loss caused by the radiation damage on the active material can be mitigated by replacing the HPDs with SiPMs. This will hold true for HL-LHC data taking period and therefore will not require an upgrade to the active material nor the read-out electronics.

The ECAL barrel, however, will need a series of upgrades to its on- and off-detector electronics to cope with the extreme conditions of HL-LHC and to maintain its current performance. The current on-detector electronics of the ECAL barrel consists of very front end (VFE) and front end (FE) boards. The VFE will contain two different kinds of ASICs named CATIA and LiTE-DTU where the former is a pre-amplifier ASIC and the latter is a data conversion, compression, and transmission ASIC. The VFE consists of $5 \times$ CATIA and $5 \times$ LiTE-DTU chips. The new FE, in contrast to the current FE, will allow streaming of full-granularity data off-detector at the bunch crossing frequency. The L1 trigger information will be provided by FE via high speed radiation hard optical links called low power GBT (lpGBT). Off-detector electronics, or back-end electronics, do not require a radiation tolerance condition considering the fact that they will be located at the service cavern. Commercial FPGAs with sufficient computing power will therefore be used for the back-end upgrade of ECAL barrel electronics. The studies summarized in [62] covers several major topics regarding the ECAL barrel performance: the lead tungstate crystal longevity, APD longevity, spike rejection, and the impact of precision timing. The crystal longevity studies shows comparable performance for the crystal life under HL-LHC conditions with one caveat being the requirement on lower operational temperature; from 18°C to 9°C. Similarly, studies done on the APDs show that the major concern regarding the APDs is the increased dark current (which will be monitored by the new FE boards). Spikes, large isolated signals due to hadron interactions within the APD volume, will be identified with better discrimination against the EM showers, thanks to the upgraded electronics. The last concern for the upgraded detector's performance is the reconstruction performance which will be improved greatly with the addition of precision timing (ECAL timing + MIP timing). For the very important decay channel $H \rightarrow \gamma\gamma$ the primary vertex efficiency would drop from 75% to 30% in the absence of the upgrade. Figure 4.3 shows studies done on different timing scenarios.

Endcap Calorimeters

As mentioned earlier in the beginning of this section, the existing endcap calorimeters (EE+HE) can withstand radiation levels corresponding to an integrated luminosity of up to 500 fb^{-1}. The proposed calorimeter complex replacing the EE+HE system is called the high granularity calorimeter (HGCAL) [58].

The HL-LHC luminosity levels, being much higher than that, will lead to drastic loss of performance therefore it necessitates a replacement of existing calorimeters. Inspired by the R&D studies conducted on the silicon tracker

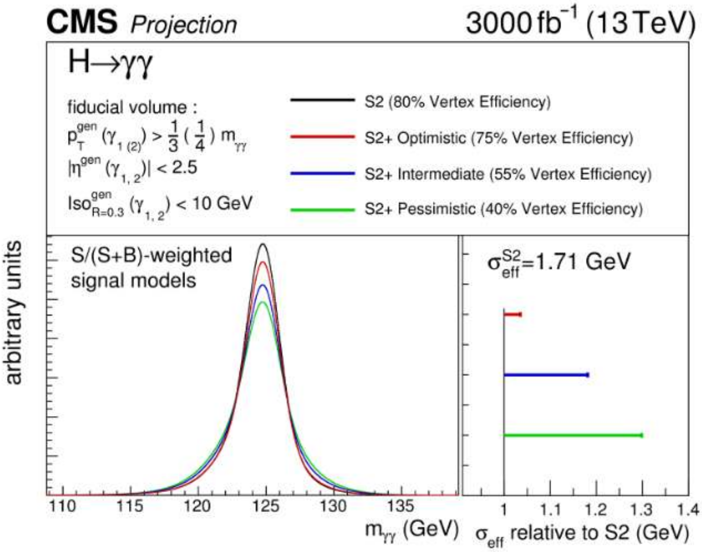

Figure 4.3. | Lineshape for the H $\rightarrow \gamma\gamma$ signal in the four scenarios: no precise timing (green), precise timing in calorimeter (blue), precise timing in calorimeter and MIP timing (red) and Run 2 conditions (black). From Ref. [62].

upgrade, choice of active material was decided to be a combination of silicon and plastic for this upgrade. Simulation studies based on fluence is shown in Figure 4.4, where n_{eq}/cm^2 denotes the number of 1 MeV equivalent neutrons per square cm. The study shows that, even after being showered with a fluence that is 50% higher than expected for the HL-LHC conditions, silicon sensors retain adequate charge collection. The design using silicon sensors with the increased leakage current and decreased charge collection efficiency requires a lower operational temperature therefore the whole calorimeter will be operated at -30°C.

The mechanical design realized for this new calorimeter consists of a sampling calorimeter with silicon and scintillators as active material. It involves an electromagnetic section (calorimeter endcap - electromagnetic (CE-E)) and an hadronic section (calorimeter endcap - hadron (CE-H)). CE-E corresponds to EE in the legacy design where CE-H corresponds to FH + BH. As can be seen in Figure 4.4, the expected radiation is higher in the electromagnetic section and the innermost hadronic section. The active material choice is made accordingly such that these inner regions employ silicon as the active material whereas the outermost region uses plastic scintillators to reduce the cost. Figure 4.5 shows the design realized with these requirements in mind.

The silicon module design that will be used in the new detector are hexagonal

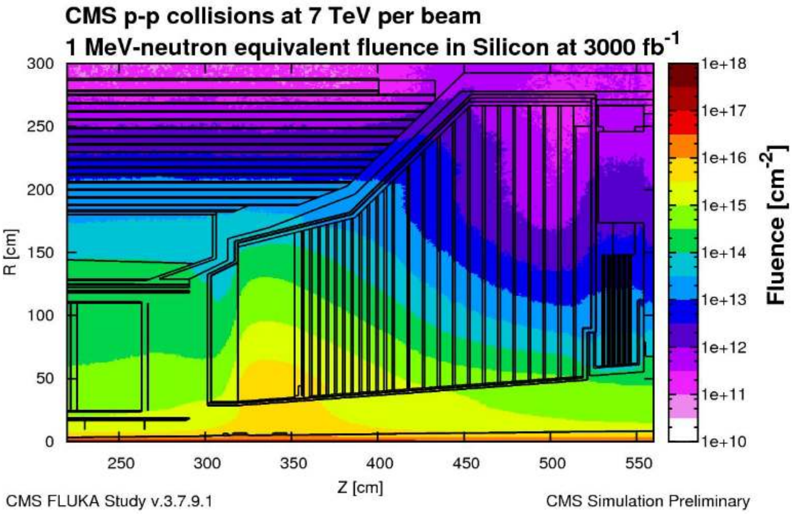

Figure 4.4. | Fluence accumulated in the endcaps after an integrated luminosity of 3000 fb^{-1}, simulated using FLUKA. From Ref. [58].

sensors with three different flavors in sensor thickness: 100 μm, 200 μm, or 300 μm with the cell size being different between the first and the last two. The plastic scintillators will be either polyvinyltoluene or polystrene-based and they will be arranged in a R-ϕ grid with their size varying between 4 cm^2 to 32 cm^2. They will be hosting the SiPM at their centre.

The HGCAL is expected to provide an unprecedented granularity by combining the timing, position, and pulse height information. This combination heavily relies on the read-out chips with the two kinds (ASICs for silicon read-out and ASICs for scintillator read-out) being conceptually very similar. The granularity that will be achieved with HGCAL provides 28 sampling layers with a total thickness of 34 cm in the electromagnetic part and 12 planes of 35 mm thick SS plates followed by another 12 SS planes with a thickness of 68 mm. The impact on the physics performance involves improvement on electromagnetic energy resolution, H $\rightarrow \gamma\gamma$ mass resolution, angular resolution, and BSM physics.

4.2.4. Muon System Upgrade

As pronounced by the experiment's name, muon detectors play a major role in CMS with two example cases being the discovery of the Higgs boson and the observation of W and Z bosons. Considering that many sensitive signatures of physics include one or two muons, CMS was built with several subdetectors to individually and accurately identify and measure muons. The longevity tests of the present DT chambers showed that the subsystem should be able work throughout the HL-LHC data-taking and a replacement is not necessary.

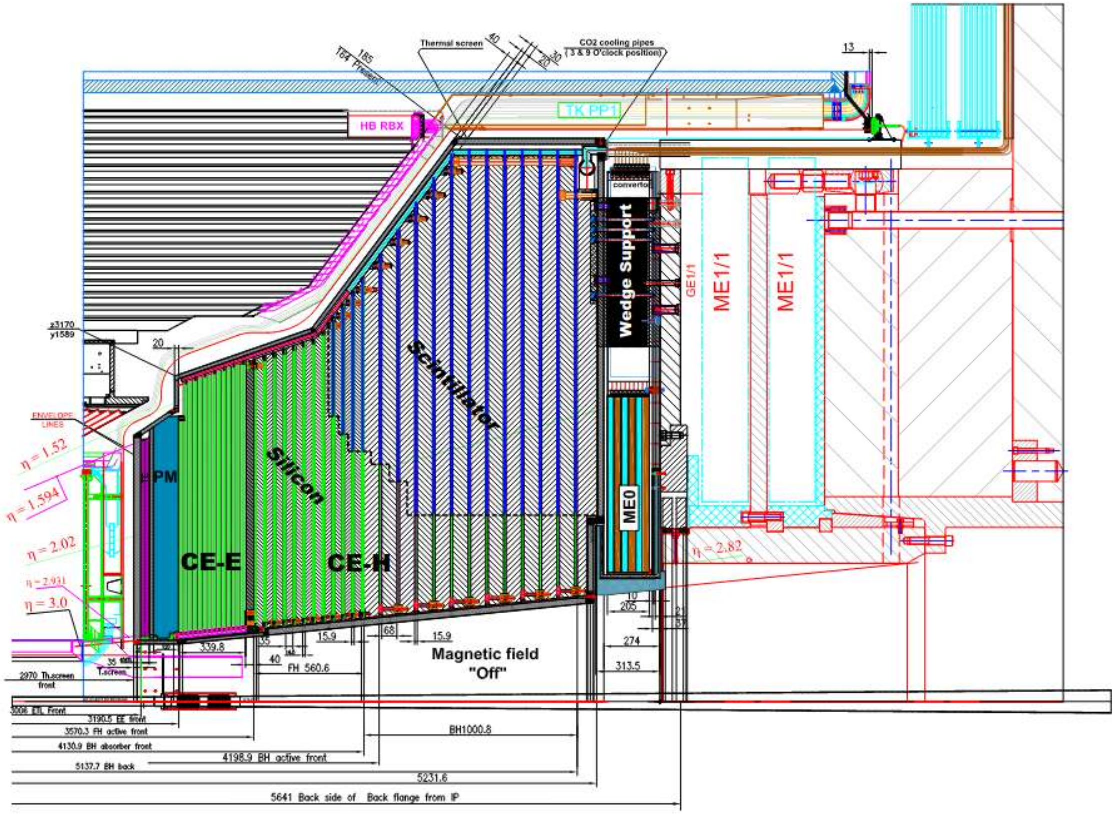

Figure 4.5. | Longitudinal cross section of the upper half of one endcap calorimeter. It consists of an electromagnetic compartment (CE-E) followed by a hadronic compartment (CE-H). The green region to the lower left is instrumented with silicon detectors and the blue region to the upper right with scintillator tiles. From Ref. [58].

The major change regarding Phase 2 is then the replacement of the Minicrate electronics (MiC) that are attached to each chamber hosting the readout and trigger electronics. The current version MiC1 will be replaced by the improved MiC2. Similarly, the longevity tests of the CSC proved that the subsystem can be used until the end of HL-LHC operation. The only change needed is once again regarding the electronics. In this case, the current cathode front-end boards (CFEB) will be replaced by digital cathode front-end boards (DCFEB). This will be followed by other minor changes in anode local charged track boards (ALCT) and tigger mother boards (TMB). Finally, the RPCs will be able to operate until the end of Phase-2 while their link system which connects the front-end board to the trigger processors must be replaced. The new link system will include new control boards and optical links and the ASICs used on link boards will be replaced by FPGAs.

One of the major goals of CMS for the HL-LHC conditions is the reliable triggering on muons in the very forward regions. This requires the extension of pseudorapidity coverage in the forward region. To achive this, new forward muon detectors will be added to the muon system. These are namely GE1/1, GE2/1, RE3/1, and RE4/1. Thanks to the addition of these, the pseudorapidity coverage extends up to $|\eta| = 2.4$, matching the extended tracker coverage. The two first of the new detectors are GEM detectors while the two last are RPC detectors. Figure 4.6 shows the layout of the muon system with a highlight on the new detectors.

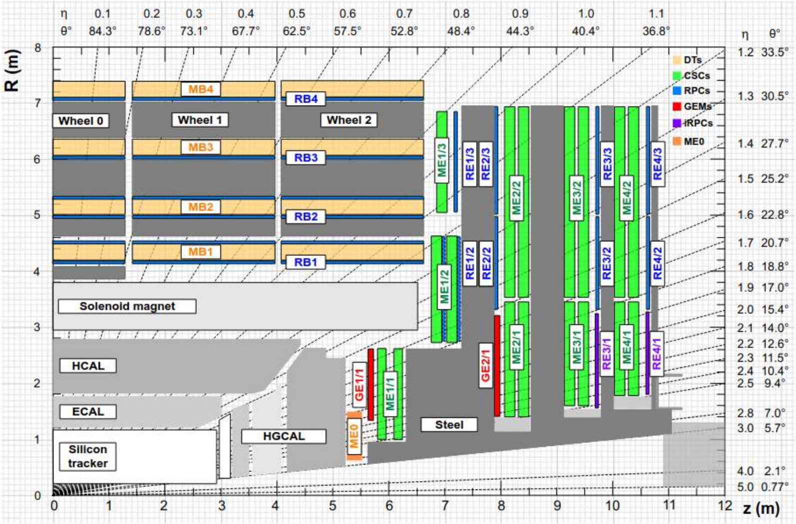

Figure 4.6. | Layout of the CMS muon detectors including both the Phase-1 and Phase-2 (ME0, GE1/1, GE2/1, RE3/1, RE4/1) upgrades. From Ref. [60].

4.3. The CMS Tracker Upgrade for the HL-LHC: CMS Tracker Phase-2

The present tracking system at CMS was designed to operate at instantaneous luminosity of $1\times10^{34}\text{cm}^{-2}\text{s}^{-1}$, with an average number of pileup events of $\sim$ 30 per bunch crossing, and up to an integrated luminosity of 500 fb^{-1}. Although the instantaneous luminosity is at higher levels than the design value, the system is still performing at very high efficiencies. However, HL-LHC considerations make it certain that performance degradation is inevitable due to the radiation damage the system will suffer. By the end of Run 2 in 2018, the LHC recorded an integrated luminosity of 150 fb^{-1}, which is expected to reach the level of 300 fb^{-1} by the end of Run 3.

The degradation expected during and at the end of HL-LHC data-taking, documented in Ref [63], shows that the pixel detectors will suffer from reduced charge collection efficiency and Lorentz angle leading eventually to reduced hit efficiency. For the strip tracker, the concern is centered around the increased depletion voltage and the increased leakage current. While the latter can be mitigated via certain solutions, the former cannot and it simply leads to inoperational double-sided strip modules already after 1000 fb^{-1}. Therefore, the present tracker should and will be replaced entirely for the Phase-2.

The main requirements for the new tracker can be summarized in the following list:

- **radiation tolerance** up to an integrated luminosity of 3000 fb^{-1} , which translates to a maximum particle fluence of 1.5×10^{15} $\text{n}_{eq}/\text{cm}^2$ in the Outer Tracker region and 2×10^{16} $\text{n}_{eq}/\text{cm}^2$ in the pixel volume;
- **increased granularity** to maintain the channel occupancy near or below the 1% level in all tracker regions;
- **improved two-track separation**, to overcome current limitations in track finding performance in high-energy jets, and exploit the statistics of HL-LHC;
- **reduced material** in the tracking volume, which is currently a significant limiting factor for the CMS tracking and calorimetry performance; extended coverage of the tracker (and calorimeters) in the forward region, which will benefit the overall CMS physics capabilities;
- **compliance with the L1 trigger upgrade** (increase of L1 rate and latency to 750 kHz and 12.5 μs) and adding tracking information to the L1 trigger decision [64].

The new tracker design that was realized with the conditions above being the driving force is shown in Figure 4.7 where two sub-systems are plotted with a color code; the Inner Tracker and the Outer Tracker.

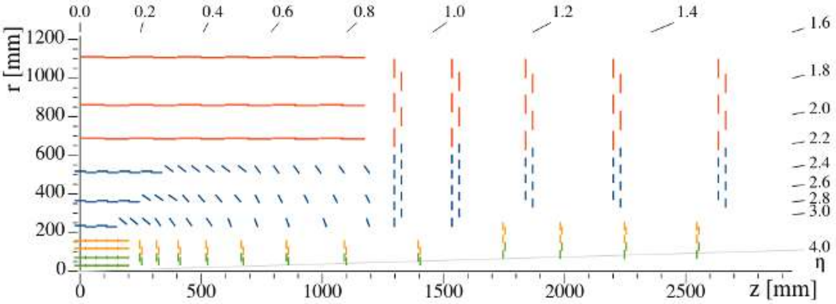

Figure 4.7. | One quarter of the tracker layout in r-z view. The green and yellow lines correspond to the inner tracker while the blue and red lines correspond to the outer tracker. From Ref. [21].

4.3.1. Inner Tracker

HL-LHC conditions imply a heavy radiation damage to the inner tracker, given that it's the closest system to the beam pipe. To accommodate the desired performance in terms of detector resolution, occupancy, and two-track separation, thin silicon sensors of thickness 100-150 μm of type n-in-p segmented into pixel sizes of 25×100 μm^2 or 50×50μm^2 will be used. The segmentation of the sensors will allow for reduced cluster size and higher charge collection per hit, which results in lowered bandwidth consumption while signal to noise ratio is increased. There are two different kinds of sensor designs: 3D sensors for the first layer as they have a higher intrinsic radiation tolerance due to a shorter charge collection path and traditional sensors for the remaining layers. The 3D sensors were not chosen for the whole detector as they are more costly. Together with the ATLAS experiment, a custom readout chip with 2500 μm^2 cell size in 65 nm CMOS technology was developed for low detection threshold [65]. As can be seen in Figure 4.7, the Inner Tracker is composed of four cylindrical layers in the barrel region and eight small plus four large disc-like layers in each forward region. The pseudorapidity extension is increased to $|\eta| \approx 4$.

4.3.2. Outer Tracker

This section provides in depth detail of the outer tracker design starting with an overview of the layout. Section 4.3.2.1 describes the p_T modules including the silicon sensors and the on-module electronics, as well as the mechanical aspects. The mechanical support structures are presented in Section 4.3.2.3. Then, to conclude, Section 4.3.2.4 gives a description of the L1 track finder algorithm and the expected performance of the new tracker.

The outer tracker design took as a basis for the design the ability to participate

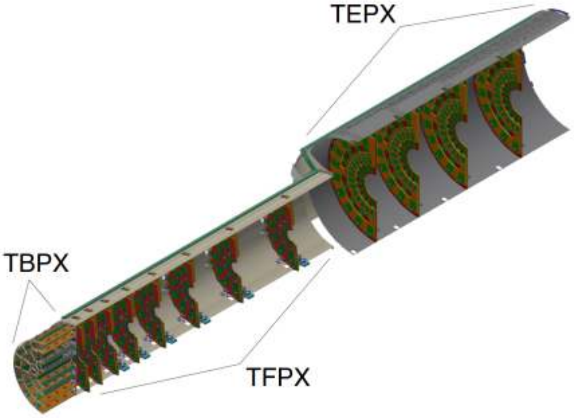

Figure 4.8. | Perspective view of one quarter of the Inner Tracker, showing the TBPX ladders and TFPX and TEPX dees inside the supporting structures. From Ref. [21].

in the L1 trigger: providing data for the L1 reconstruction per bunch crossing and for the global event processing upon reception of L1A decision. For ease of design, cost, production, and operation of the detector, only two module version are conceived [64] where each version has their subcategories that differ by the thickness, the length of the pigtail, and cooling contacts. Figure 4.9 shows the layout of the outer tracker with two module concepts plotted in blue (PS) and red (2S).

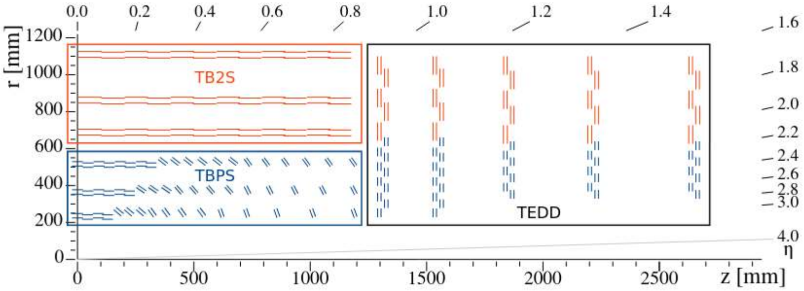

Figure 4.9. | Sketch of one quarter of the Outer Tracker in r-z view. Blue (red) lines represent PS (2S) modules. The three sub-detectors, named TBPS, TB2S, and TEDD, are indicated. From Ref. [21].

The new detector has a barrel region that is composed of six layers in the central region covering the range $|z| < 1200$ mm. The two sub-detectors of the barrel region are distinguished by the module choice of the sub-system: the Tracker Barrel with PS modules, TBPS; the Tracker Barrel with 2S modules, TB2S. The endcaps complement the barrel region on each side by five double-disc structures covering the region $1200 < |z| < 2700$ mm. This sub-detector is called the Tracker Endcap Double-Discs, TEDD.

Table 4.2 presents a size comparison of current silicon tracker and new outer tracker.

	Current	Phase-2
Silicon [m^2]	200	220
Strips	9×10^6	48×10^6
Macropixel	–	217×10^6
Modules	15148	15508
Readout rate [kHz]	100	750
Stub readout rate [kHz]	–	40000

Table 4.2. Size comparison of current and Phase-2 tracker [64].

4.3.2.1. Sensors and p_T modules

Located at 20 cm from the interaction region, outer tracker will be exposed to great levels of radiation which corresponds to a hadron fluence of $1.5\times10^{15} n_{eq} cm^{-2}$. The extensive studies that can be accessed via Ref. [66–70] explored a broad range of materials and concepts to achieve the required radiation tolerance and to outline the requirements of operating temperature. The options explored are Float-Zone, Magnetic Czochralski substrate, and Epitaxial substrate, both p-in-n and n-in-p with active thickness of 50 μm to 300 μm. The charge collection performance, noise behaviour, and strip isolation before and, more importantly, after irradiation being the deciding factors, the sensor choice converged on n-in-p sensors with a (290) 320 μm (active) thickness.

The module design that was realized was required to provide tracking information to L1 trigger. As explained in the Section 2.2.7, this would mean transferring hit information off-detector at the bunch crossing rate of 40 MHz. The hit levels that will be achieved in HL-LHC data-taking would require a very large bandwidth to accommodate the transfer, which is simply unaffordable by the experiment. The solution to this issue was provided with the new module concept; modules that are themselves capable of rejecting hits from particles below a certain transverse momentum, p_T threshold, therefore the name *p_T modules*. Studies show that a threshold imposed at 2 GeV already corresponds to a data reduction of one order of magnitude [64].

Two flavors of p_T modules are devised to be used across the outer tracker and are composed of two very closely spaced silicon sensors that are read out by a common front end that is capable of correlating the signals collected in two sensors of the module. The correlation of the signals is done such that for each hit on the inner sensor an acceptance window is defined on the outer sensor hit and once there is a matching pair then the two hits are used to form a *stub* (Figure 4.10), that is compatible with the particles above the chosen p_T threshold.

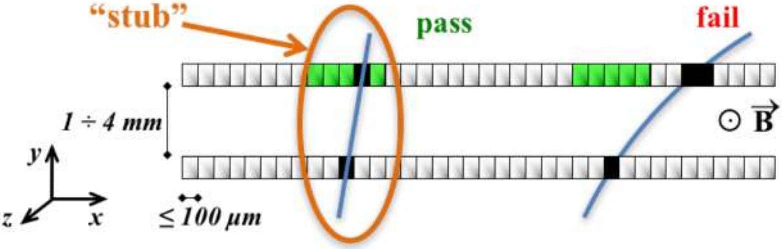

Figure 4.10. Illustration of stub finding concept showing how the correlation of signals in closely-spaced sensors enables rejection of low-pT particles; the channels shown in green represent the selection window to define an accepted stub. From Ref. [21].

Flavor **2S** stands for two superimposed strip sensors of ≈ 10×10 cm^2. They are mounted with the strips parallel to each other and segmented in strips of dimensions 90 μm × 5 cm. Making up an approximate sensing area of 150 m^2, they populate the outer regions (can be seen in Figure 4.9) with r ≈ 60 cm. The two strips are wire bonded at the opposite ends of the sensor to the front-end hybrid (FEH). Made with the same flex technology as the FEH, service hybrids (SEH) carry the auxiliary electronics for powering and optical readout. Each 2S module carry one service hybrid at one end of the sensor assembly.

Flavor **PS** stands for two sensors of ≈ 5×10 cm^2 where one of the sensors is segmented in macro-pixels of size 100 μm × 1.4 mm and the other segmented in strips of size 100 μm × 2.4 cm. The strip sensors of PS modules are wire bonded to their readout chip, similar to 2S modules. The readout chip of the macro-pixel sensor is wire bonded to the readout chip of the strip sensor. Because of space limitations, PS modules do not have a service hybrid like the 2S. Instead, this is implemented in two separate circuits: opto hybrid for the readout and the power hybrid for powering.

4.3.2.2. Architecture and electronics

The outer tracker electronics and architecture is designed to readout data at L1A rates up to 750 KHz and to cope with latencies up to 12.5 μs. This section will give an overview of on-module/front-end and off-module/back-end electronics that will be employed in the detector along with its architecture and data flow. The system architecture can be seen in Figure 4.12.

At the *front-end*, on-module electronics for the outer tracker benefits heavily from the custom developed ASICs and HL-LHC wide services for data transfer

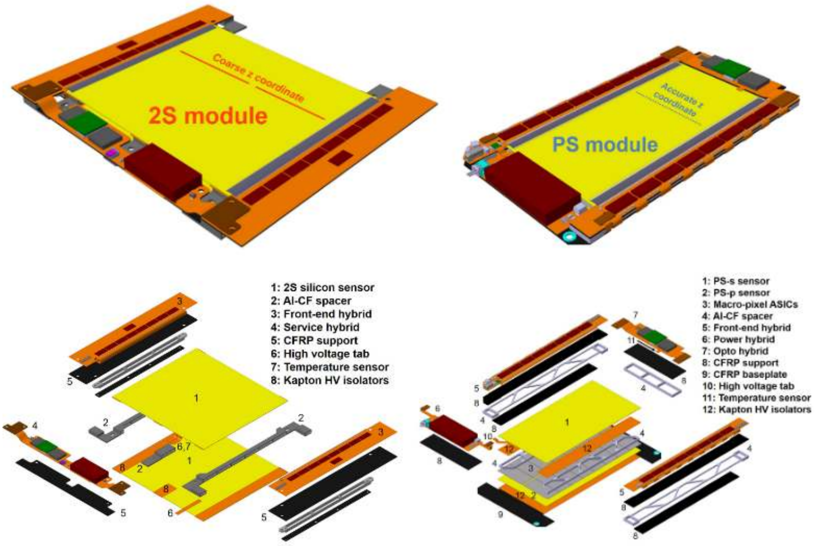

Figure 4.11. | The 2S module (left) and PS module (right) of the Outer Tracker. Shown are views of the assembled modules (top) and exploded view of the modules (bottom). From Ref. [21].

such as Low-power Gigabit Transceiver (LpGBT) [71] and Versatile Link Plus (VL+) [72]. Both module types carry two electronic readout hybrids surrounding the sensor. Each 2S front-end hybrid carries eight CMS Binary Chips (CBCs) responsible for the sensor readout. The Concentrator Integrated Circuit (CIC) ASIC serves as interface between the CBCs and the readout link. For the PS modules, however, the custom readout chip is called the Macro-Pixel ASIC (MPA) for the macro-pixels and the the Short Strip ASIC(SSA) for strips, while the concentrator chip is the same as 2S, the CIC. Once the readout is done by the FE chips, the data is buffered, aggregated, and formatted by the CIC that acts as a data hub to the service hybrid. Supporting the powering and optical readout, service hybrids hosts all services to/from the counting room: bidirectional optical data transfer (VL+), low voltage power (LV), and high voltage bias (HV). As mentioned earlier, the service hybrid is split into two hybrids for the PS module: the Power Hybrid (POH) and the Read-Out Hybrid (ROH) lying in opposite positions of the module. The DC-DC converters allowing for a self-contained and independent unit, carrying its own components for power delivery and defining power granularity at module-level are located on the same hybrid (service hybrid) for the 2S modules. Whereas, for the PS modules, the DC-DC converters are located on the POH.

At the *back-end*, a custom developed commercial FPGA based board called the

Data, Trigger, and Control board (DTC) sends and receives data to/from the modules. It processes three data streams to/from the detector: data acquisition (DAQ) referring to the full event data sent upon receiving L1A signal, L1 track finder data (TRIG) referring to the data sent to L1 trigger at bunch crossing rate, and timing & control (TTC & CTRL) referring to the clock and trigger signals.

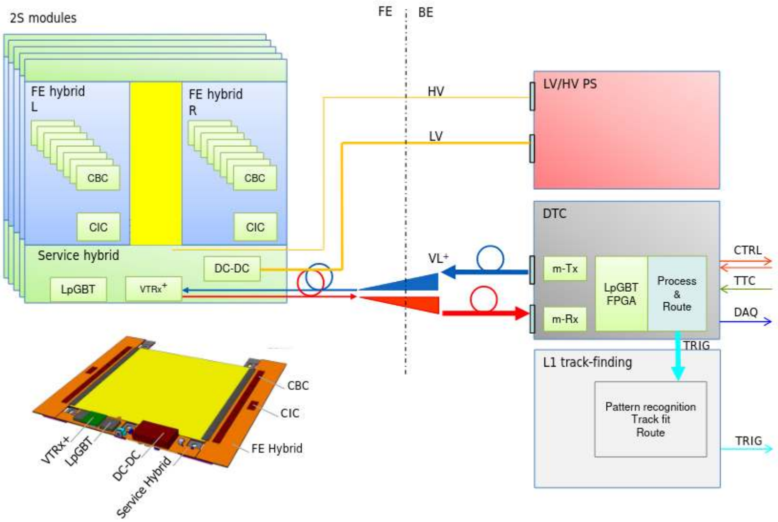

Figure 4.12. | The block diagram of the system architecture exemplified for the 2S module. From Ref. [21].

4.3.2.3. Mechanical structures

As mentioned earlier, the outer tracker has three sub-detectors: TB2S, TBPS, and TEDD.

The TB2S sub-detector, reusing the concept from the present TOB detector, features ladder structures that are made of two parallel carbon fibre C-shaped profiles on which the modules are mounted. A wheel consisting of four discs joined by cylinders at the inner and outer radii is used as a support structure. The ladder length was decided to be half the length of the wheel to ease the installation from the two ends of the barrel. See Figure 4.13.

The TBPS sub-detector consists of three concentric layers where each layer is divided into one central section with horizontal modules that are supported by flat plank structures and two tilted sections with tilted modules that are supported by conical rings. See Figure 4.14.

Tracker **E**ndcap **D**ouble-**D**isks consist of ten double-disks whose building element are half-disk structures called the *dee*s on which the modules are mounted. The double disks are made of two discs, providing one hermetic

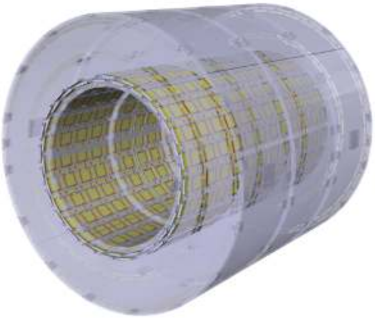

Figure 4.13. | The innermost layer of TB2S installed in the support wheel. From Ref. [21].

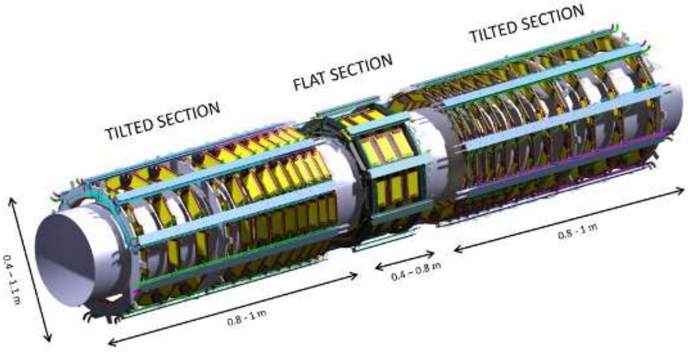

Figure 4.14. | The innermost layer (layer 1) of the TBPS, showing the central flat section and the two (identical) tilted sections. From Ref. [21].

detector plane and five double discs make up one full endcap detector. The TEDD discs come with two different radii to accommodate the change in diameter of the Inner Tracker support tube. The dees have a sandwich structure with multiple layers and the cooling pipes run inside these layers. See Figure 4.15 for simplified 3D models of the design realized.

4.3.2.4. L1 track finder

As outlined earlier in this chapter, L1 track finder in CMS Phase 2 is driven by the p_T module concept and the stub finding mechanism. In the presence of intense magnetic field of the superconducting magnet particles produced in the collision follow a helical trajectory with their bending radius being proportional to their momentum; lower momentum particles therefore traverse the detector volume at a higher angle to the perpendicular. This trajectory produces hits in the two sensors of the module that are farther apart. The implementation of a p_T threshold (> 2 GeV) is therefore made possible by choosing an acceptance

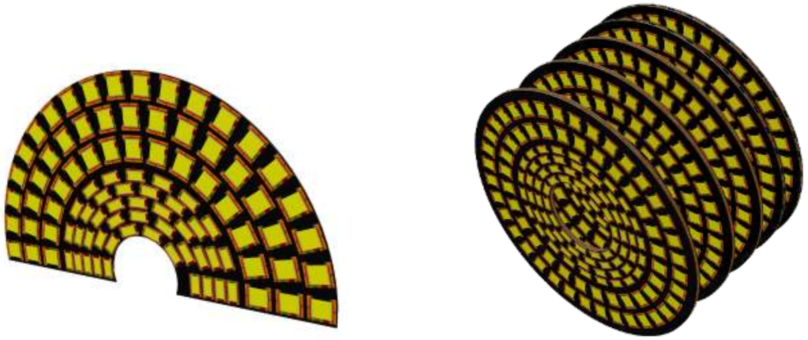

Figure 4.15. A fully assembled dee (left) and a TEDD unit (right) consisting of five double-discs where each double-disc consists of four dees. From [21].

window in the upper sensor, providing a data reduction of one order of magnitude [73].

The L1 track finder will reconstruct all charged particle tracks with a p_T greater than 2 GeV using the stubs in a collision environment where $\sim$ 10000 stubs will be produced for every event. This means that around 200 tracks will need to be reconstructed within the latency budget; approximately 5 μs including a 1 μs estimate for the transmission of the stub data from the detector to the counting room. Different system architectures has been explored and can be accessed via Ref. [21, 74, 75]. The final system design converged on a hybrid solution making use of the tracklet approach (also called the road-search approach) for the pattern recognition and the Kalman filter for the final track fit, bringing ease of implementation by using FPGAs instead of custom ASICs.

The track finder hardware consists of custom boards called Apollo [76] that carry two Xilinx Virtex Ultrascale+ VU13P FPGAs and a 25 Gb/s fibre optic links for receiving and transmitting tracks to the L1 trigger boards. The track finder algorithm that the FPGA's are programmed with is split into multiple independent modules that process one event at a time. The modules are sometimes repetitive in the algorithm chain as to provide parallel processing of stubs from the same event. Figure 4.16 describes the track finding concept: first, stubs are paired up to create seeds; second, by using the seed and the origin, a helical track is calculated and projected to the other layers; third, stubs that are within the acceptance window in the other layers are matched to the track.

The L1 track finder operates in a modular fashion, with specific regions of the tracker corresponding to a sector. These sectors are known as "trigger sectors". The trigger sectors are defined based on the geometry and layout of the Phase-2 tracker where the sectors are typically defined based on a range of pseudorapidity (η) and azimuthal angle (ϕ) covered by each sector. The trigger

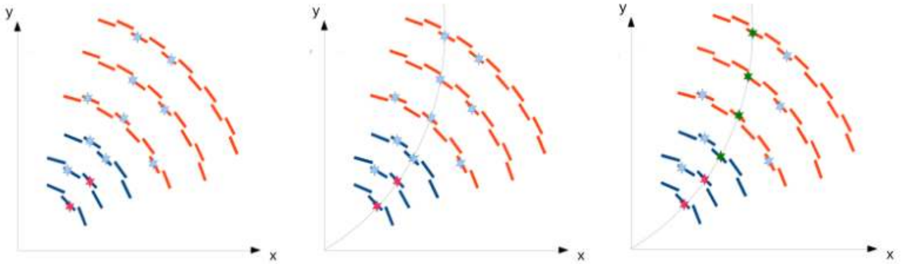

Figure 4.16. | Illustration of the tracklet concept from a section of the Outer Tracker barrel in x-y view is shown. Blue and red lines represent PS modules and 2S modules, respectively. From Ref. [21].

sectors ensure that each processing unit within the L1 track finder focuses on a specific region of the tracker, reducing the amount of data that needs to be processed by each unit. This division allows for efficient parallelization of the track finding algorithm and minimizes latency. Section 4.3.2.6 describes how the division into trigger sectors were defined based on the physical modules of the tracker and shows an example layout resulting from this.

4.3.2.5. Expected performance

The Phase-2 Tracker will reduce the inactive material inside the tracker volume and deliver a significantly extended tracking acceptance compared to the Phase-1 Tracker. The expected performance of the new tracker has been studied by using validated hardware demonstrators and simulated HL-LHC data. Using the given geometry and prototype results, extensive Monte Carlo studies were conducted to assess the tracking performance of the detector. Figure 4.17 illustrates the improvement in transverse momentum and impact parameter resolution across the entire range of pseudorapidity for single muons. The new geometry yields enhancements in both parameters. To evaluate the track reconstruction performance, tt events were generated with the addition of minimum-bias events. Figure 4.18 displays the efficiency and fake rate for tracks originating from the tt events, considering two different pile-up scenarios. In both scenarios, the tracking efficiency remains around 90%, while the fake rate stays below 2% for the 140 pile-up scenario. The optimization of the tracker geometry is an ongoing process, addressing the efficiency dip observed around $\eta \sim 1.2$. Figure 4.19 illustrates an example of expected L1 tracking performance for tracks in $t\bar{t}$ events overlaid with an average pileup of 200 interactions, employing the hybrid solution outlined in Section 4.3.2.4.

The new tracker promises tracking efficiencies exceeding 90% for tracks with p_T greater than 2 GeV. The tracking resolution is expected to be about 1 mm around central η, while it is less precise at higher η as a consequence of the

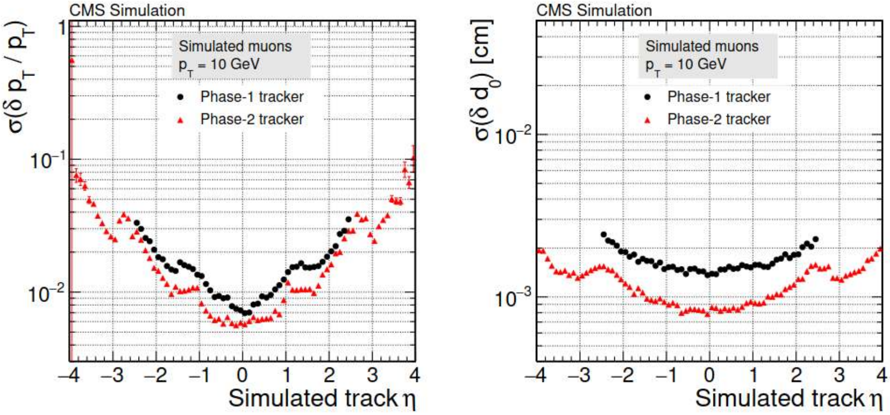

Figure 4.17. | The resolution of the transverse momentum (pT) and impact parameter of isolated muons is compared between the Phase-1 and Phase-2 upgraded trackers as a function of pseudorapidity [77].

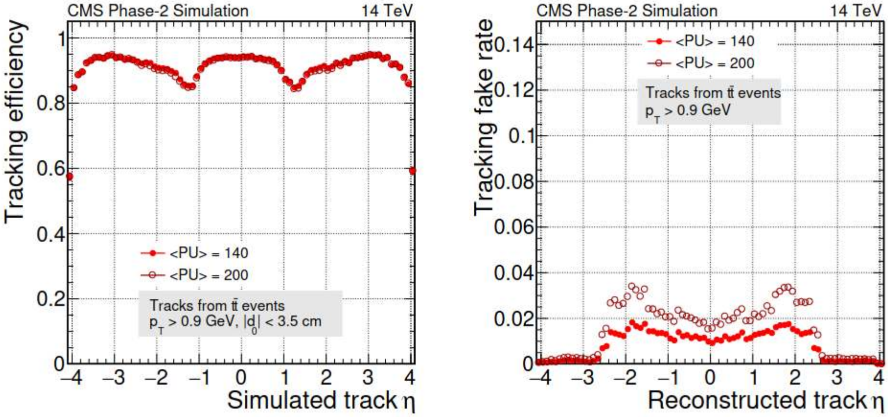

Figure 4.18. | The efficiency of track reconstruction (left) and the rate of falsely reconstructed tracks (right) are shown as a function of pseudorapidity for tracks originating from tt events with the addition of 140 and 200 superimposed minimum bias events [77].

CMS outer tracker geometry with tilted PS modules.

4.3.2.6. Tracker modeling with tkLayout

The Phase 2 upgrade of the world's largest silicon tracker, among other motives, is planned to be instrumented with L1 triggering capabilities. Finding the right detector design (material, geometry, layout) while preserving the desired tracker performance is therefore a task that calls for computer-aided studies. The tkLayout [78] tool is developed specifically to perform thorough analysis

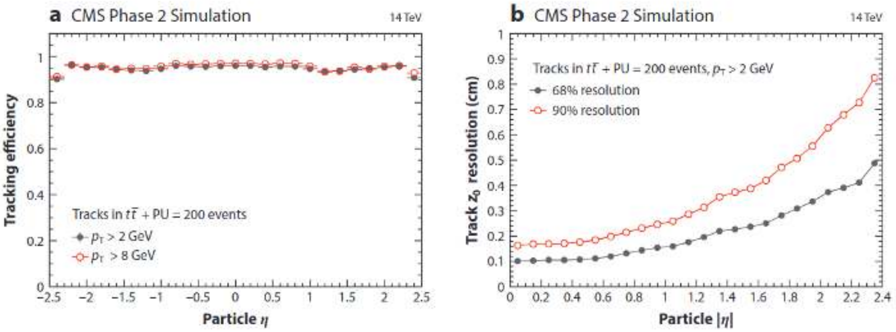

Figure 4.19. a) L1 track-finding efficiency as a function of particle η and b) L1 track longitudinal impact parameter resolution as a function of $|\eta|$ for charged particles from top quark pair events with an average of 200 additional pileup (PU) interactions [77].

of different tracker architectures. The tool creates 3D models of the tracker with addition of material according to a set of user-defined rules. Once the tracker architecture has been modeled, the internal geometry and the material is exported to the CMS Geant4-based Monte Carlo (MC) simulation framework CMSSW, for physics analysis.

The tool has been heavily benefitted for performance tests on different configurations and the detector design in terms of module geometry, trigger window and sensor spacing dimensioning, and module positioning has been completed. The focus of this section, the cabling of the services, takes as an input the mapping of the modules to the services channels that is achieved with tkLayout.

Before moving into the cabling mapping of the modules, a review of the nomenclature is necessary. For optics, 2 fibers exit the outer tracker module that is counted as one link. These links are gathered into Multi-Fiber Bundles (MFB) and the MFBs are gathered into Multi-Fiber Cables (MFC). The MFC is then connected to the corresponding Data Trigger Control (DTC) board. Therefore the mapping that was implemented is as the following:

Outer Tracker Module $\Longleftrightarrow$ MFB$\Longleftrightarrow$ MFC $\Longleftrightarrow$ DTC.

The φ-sector segmentation is done such that each sector corresponds to one DTC-rack. This is achieved by making 40° φ-sector that creates 9 slices per Z^{-}side.

The last consideration for the mapping of the cabling is to minimize the total number of MFBs and MFCs where each MFB contains at most 24 fibers and each MFC contains at most 6 MFBs. Once the mapping is done, the MFBs are assigned to services channels. These channels are clusters where services, routed from modules to the counting room, are gathered. For the Outer Tracker, there are 12 channels on each Z^{-}side of the detector. Figure 4.20 shows one half of the channels on one Z^{-}side. Each service channel, labeled OT* in Figure 4.20, has three sections: section B for the optics (in the center) and sections A and C for power cables and cooling pipes. See Figures 1.2 and 1.3 in the appendix for visualizatino of channels A, B, and C.

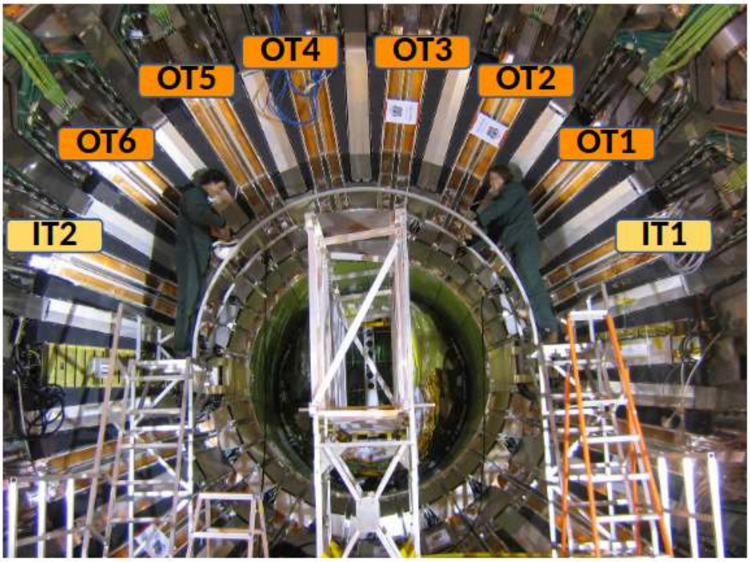

Figure 4.20. | Services channels on one Z-side of the Outer Tracker.

For the power cabling map, exact same scheme as the module to MFB is used and therefore the same mirror symmetry as the optical scheme applies here as well.

Optical and power services have been assigned to services channels. For optics, the assignment has been done with the criteria that all MFBs connected to the same DTC are routed through same services channel, while minimizing MFB crossings. For power, however, channels assignment needs to follow rotational symmetry of 180° around CMS-Y (this is to avoid clash with cooling pipes routing, and avoid duplicating cooling pipes design).

The assignment of optical services to services channels OT*B and the assignment of power services to services channels OT*A to OT*C are shown in Figure 4.21 and 4.22 for the first double disk of TEDD1. This information is later on used for the routing of the services on the dee surface which will be described in Section 5.4.2.3.

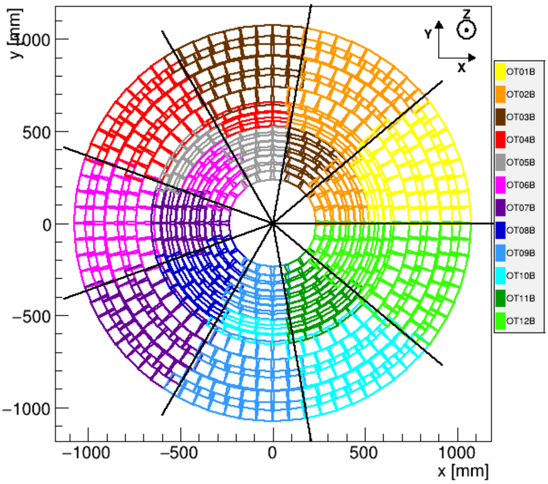

Figure 4.21. | Assignment of optical services to services channels for TEDD1 Double Disk 1, (+Z) side [79].

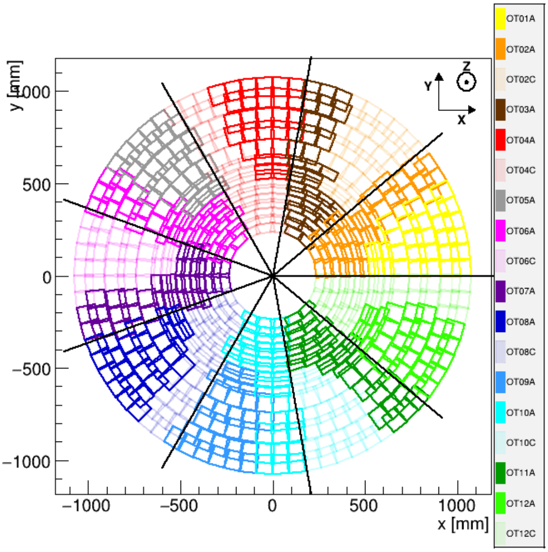

Figure 4.22. | Assignment of power services to services channels for TEDD1 Double Disk 1, (+Z) side [79].

5. Chapter

Building an Endcap Detector: TEDDs

Chapter 4 outlined the HL-LHC upgrade of the CMS detector with an emphasis on the outer tracker upgrade as the author of this document took active role in a broad range of upgrade efforts of the endcaps of the new detector. The tracker endcap upgrade project is managed between three collaborators: CP3 at UCLouvain, DESY Hamburg, and IP2I Lyon, where CP3 and DESY are assembly centers for one full endcap each. The author, being a part of the team at CP3, is involved in the R&D efforts for the services design of the dees, developing integration tests and procedures, as well as developing control systems. This chapter is therefore dedicated to the topics that are aforementioned and will begin by a description of the cleanroom built at CP3 along with the DCS system developed. Then, in the third and fourth section, the TEDD design as well as the services design will be described. The last section will cover the integration tests and the module burn-in.

5.1. CP3 Cleanroom

The upgrade project relies heavily on electronic components that need to be kept and operated in a sterile environment, not to get them contaminated by dust and other airborne contaminants. The CP3 cleanroom was built out of this necessity according to the ISO 14644-1 standard. The existing room has two partitions of which the smaller can serve as the technical room to accommodate the major equipment. The technical room has an air supply unit that can deliver 1.500 m^3/h to the plenum (part located above the false ceiling of the clean room) of which 300 m^3/h is fresh air and 1200 m^3/h is the recirculated air from the supply unit. The fan motor of this supply unit is equipped with a variable speed drive that controls the pressure in the cleanroom; overpressure of 15 Pa during the active period and of 5 Pa during the rest period. The temperature of the room is controlled from inside the room with display of setpoint and room temperature. A 3D model of the room displaying both the technical room and the cleanroom is shown in Figure 5.1. The assembly and integration stations shown in Figure 5.1 are the dee cold box, the dee integration trolley, and the disk and double-disk assembly station, from right to left respectively.

The backend equipment required for module and dee tests are stored in the technical room with the temporary exception of keeping the DAQ equipment in the cleanroom until the developments are over. The main equipment are:

- **MARTA** chiller: a transportable laboratory chiller based on evaporation of liquid CO_2. Its technology uses as a basis the TRACI (Transportable Refrigeration Apparatus for CO_2 Investigation) – originally developed at CERN. It can provide a cooling capacity of up to 300W at −30°C,

- **CAEN** power supply: a standard choice of power supply unit that can provide LV and HV to the experiment. SY4527 mainframe, 5 x 8-channel LV (5-15 V) and 4 x 12-channel HV (3.5 kV),
- **High-power chiller**: Julabo FP-52 chiller circulating oil-based fluid, with a working temperature range of −60°C to 100°C, heating power of 3 kW and cooling power at −35°C of $\approx$ 700 W. Used to help cool down the cold box environment, and to heat it up in case curing of the thermal interface material of PS modules is needed,
- **Donaldson** Ultrapac air dryer: The cold box will be flushed with dry compressed air, to avoid buildup of condensation on the cold modules. Depending on the air tightness of the box, an outlet needle valve may have to be added to the box to keep the inside pressure reasonable and drain the humid air quicker,
- **DAQ**: μTCA crate containing up to six FC7 boards, each housing up to two mezzanine cards, each accepting up to eight opto-electrical SFP transceivers (therefore max. 16 modules per FC7).

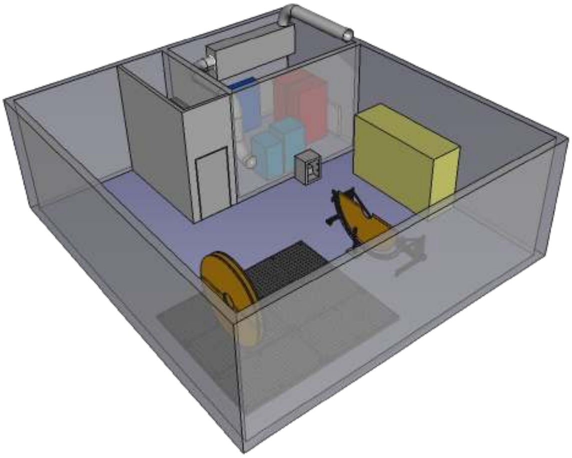

Figure 5.1. | 3D model of the cleanroom and the technical room.

The cleanroom is designed to host the integration and assembly of the dees and eventually of the TEDD. As can be deduced from the model in Figure 5.1, there is a designated dee integration area and a double disk (DD) assembly area. The part of the cleanroom that is empty in the figure (top left corner) will be the double disk storage area. The dee integration will be performed on an integration trolley shown close-up in Figure 5.2.

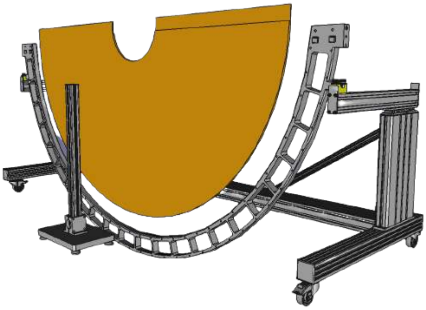

Figure 5.2. | 3D model of the dee integration table with a dee installed on it, showing the elevator arms and third support arm.

The table is made of aluminum profiles and by the use of the elevator arms it can move upwards and downwards. The third support arm is used as a standalone arm to stabilize the dee at the demanded angle as the dee can be rotated on the table. The frame that surrounds the dee, the arc frame, serves as a support mechanism as well as accommodating the temporary patch panels for the dee integration and testing. To place the dee on the table, aluminum clamps will be used to clamp the dee on the arc frame.

The double disk assembly will be done in the designated area in Figure 5.1 (bottom left corner). To simplify the model of the room visually, the equipment for DD assembly is not presented. However, this will be explained in detail in the last section of the chapter. The remaining items from the 3D model of the room are two cold boxes for two distinct purposes. First of these is the smaller cold-box, the module burn-in box. Section 5.5.1 will cover the design of the box and the burn-in procedure in detail. Second is the larger cold-box, the dee box for sector tests of the dees. Section 5.5.2.1 will cover this at length, describing the design of the box and the sector test procedure.

5.2. CP3 Cleanroom: DCS/DSS

A detector control and safety system (DCS/DSS) composed of hardware and software components is implemented following the standard architecture and tech stack in Internet of Things (IoT) [80]. The software component is implemented through fully open source solutions (FOSS) running in a containerized environment. The first one to mention among these solutions is a flow-based programming tool called Node-Red which makes it fairly easy to build your system architecture on a flow editor. The platform provides an editor where each hardware device can be introduced as a node and the user can define, wire together, and program these nodes. For the control of the cleanroom components, a DCS architecture is implemented in Node-Red with a finite-state-machnine (FSM) architecture. The platform supports a user interface (UI) feature that helps build user friendly UIs. Figure 5.3 shows the UI for CAEN.

The second FOSS tool that the DCS system heavily relies on is a time-series database InfluxDB. The DCS/DSS data is continuously published to this database and accessed later on for visualization purposes. This brings up already the third FOSS tool used in the system; Grafana. It is a web application for interactive visualization. Figure 5.4 shows the dashboards created for MARTA parameters. The communication is handled via mostly MQTT protocol and in some cases HTTP protocol.

Figure 5.3. | The user interface for CAEN power supply. The DCS details with the FSM state is indicated on the left. The control of the LV and HV channels is indicated in the middle and on the right, respectively.

Figure 5.4. | The dashboards for MARTA parameters: temperatures, CO_2 pressures and flow rate, as well as the status summary is plotted.

The system architecture summarized in the schematic in Figure 5.5 shows how the hardware devices of the cleanroom is integrated in the DCS and their control and monitoring is done through the FOSS services. The monitoring of the environmental conditions of the experiment and of the room as well as alarm and interlock mechanisms are implemented via a distributed control system called the DiSCo, which makes the hardware component of the system. Next section describes this custom developed board in detail.

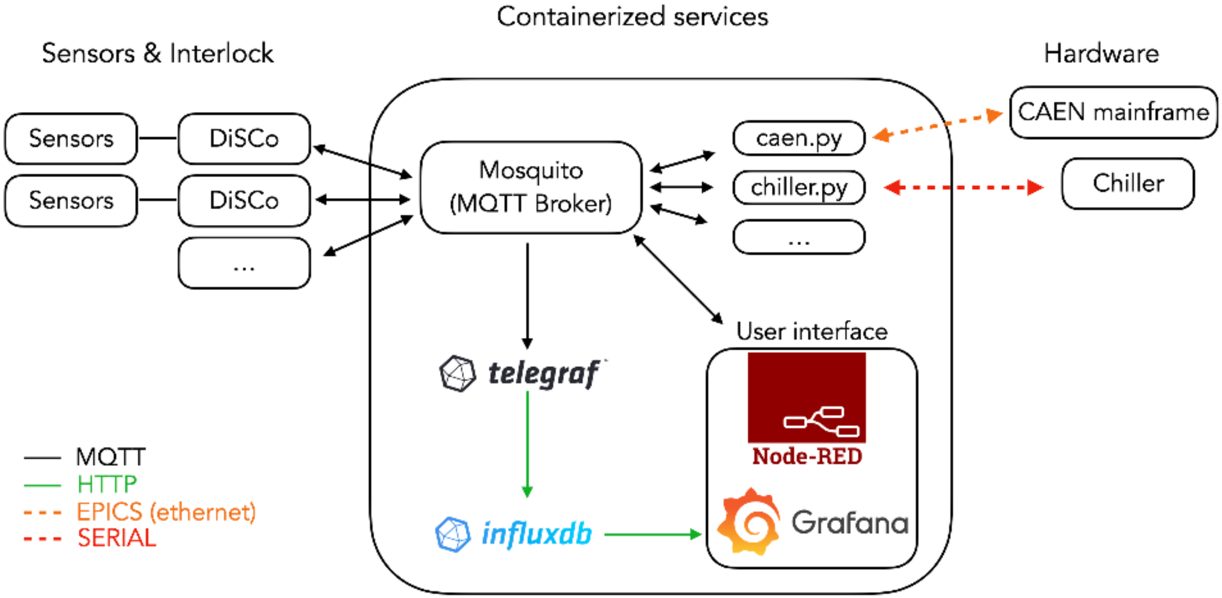

Figure 5.5. | The system architecture for the DCS/DSS.

5.2.1. Developing a Distributed Slow Control System: DiSCo

Distributed **S**low **Co**ntrol system is a generic, low cost tool dedicated to the monitoring and environmental control in the assembly and production centers for the Phase II upgrade of the CMS Tracker. Its hardware part (see Figure 5.6) is based on the ESP8266 chip with WiFi module mounted on the dedicated board for powering and programming while the firmware of the boards is written on Arduino. The firmware uses the MQTT messaging protocol to publish data to the database for further analytics and monitoring on Grafana.

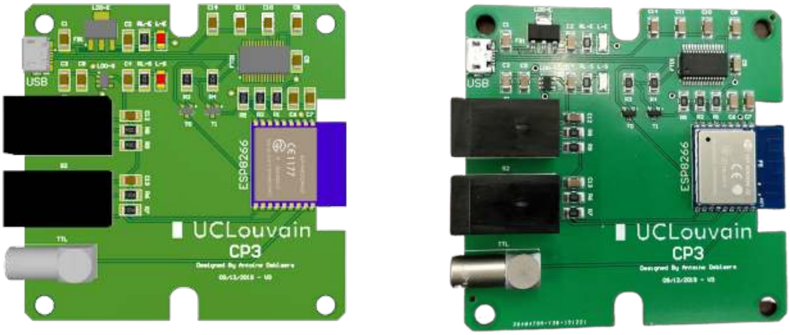

Figure 5.6. | The design of the DiSCo board PCB (left) and a picture of a printed and assembled PCB (right). The boards host the ESP8266 WiFi enabled microcontroller, two GPIO connectors for sensors that can work with either I^2C [81] or One-Wire [82], a Lemo TTL output for interlock signals, an FTDI USB chip for programming ESP8266 microcontroller.

The boards shown in Figure 5.6 are then coupled with a variety of sensors for temperature, humidity, dewpoint, and CO_2 measurements and monitoring. The GPIO connectors are used to input the sensor data and the communication protocol is chosen (I^2C or One-Wire) depending on the sensor type. This forms a sensor module (the DiSCo motherboard and the sensor boards combined) and the modules are distributed over the cleanroom and the technical room as well as the inside of the experiment; the coldboxes. This ensures a comprehensive monitoring of the full lab environment. The Lemo TTL output is used to send an interlock signal to hardware devices to stop operation in case of warnings or alarms. The choice of sensors are as the following:

- **DS18B20** temperature sensor with a range {-55°C, +125°C} with an accuracy of ±0.5°C, communication through One-Wire,
- **BME280** humidity, temperature, and pressure sensor with humidity measurement accuracy of ±3%, communication through I^2C,
- **SCD30** CO_2, temperature, and humidity sensor with CO_2 measurement accuracy of ±(30ppm +3%), communication through I^2C.

Figure 5.7. | The dashboard created with sensor readout: the humidity levels (top plot) and the dewpoint (middle plot) in the burn-in box and in the technical room, and CO_2 levels in the technical room (bottom plot).

At the time of writing, the DiSCo boards are deployed in the burn-in box and the technical room for environmental monitoring. The customizability of the firmware allows for the implementation of an interlock logic however th interlock functionality is not thoroughly tested and not at use at the moment. The advantage and disadvantages of the boards are further discussed in Section 5.8.

5.3. TEDD Design

Section 4.3.2.3 briefly described the mechanics of the new outer tracker. This section, however, will give a detailed description of the TEDD design.

Both outer tracker end caps will consist of five double-disks (**T**racker **E**nd cap **D**ouble-**D**isks), which in turn consist of two disks. Each disk is made of two identical half-disk support structures - the so-called Dee. The detailed specifications of the Dee are described in section 5.3.1. Each double-disk is equipped with modules in such a way that each charged particle traversing the double-disk will be at least detected in one Silicon detector module. In order to achieve this, the Dees/Disks forming a Double-Disk are equipped with modules on their front and backsides. The detailed layout is shown in Figure 5.8. The modules are arranged in 15 rings with modules on odd-numbered rings (red and black in the figure) mounted on the so-called odd Dees/Disks, and modules on even-numbered rings (green and blue in the figure) mounted on even Dees/Disks. Full coverage within a ring of modules is established by alternating modules in the φ-angle (see section **??** for the definition of the coordinate system) between frontside (red and green) and backside (black and blue) of a Dee/Disk.

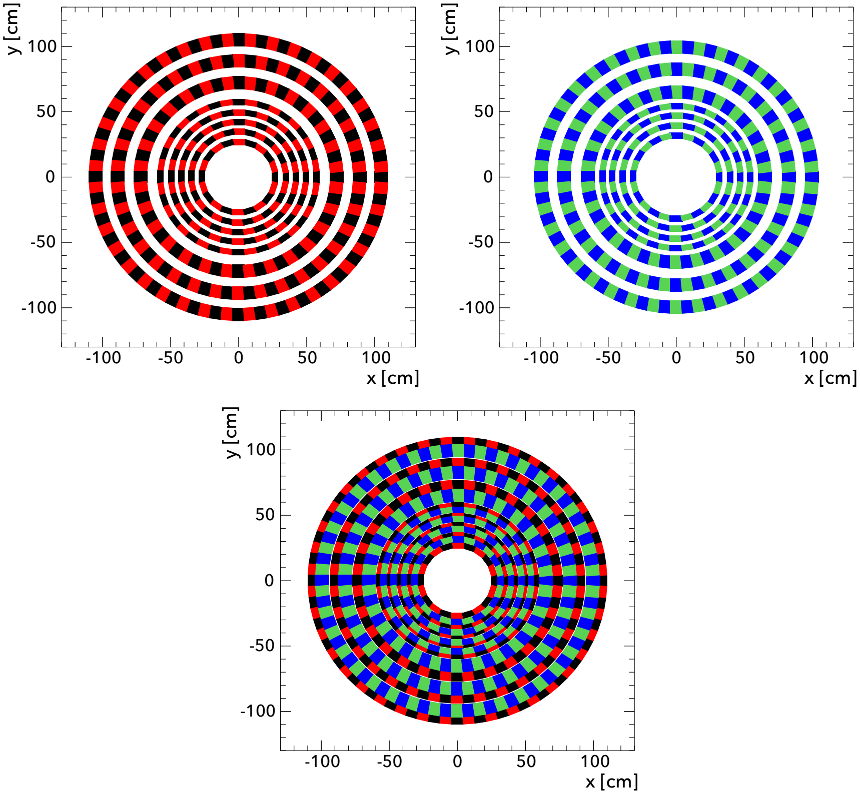

Figure 5.8. | Sketch of the arrangement of modules on the odd (top left) and even (top right) type TEDD1 Disks, and the Double-Disk (bottom).

The first two Double-Disks have a smaller inner radius and are called TEDD1. The remaining three Double-Disks are called TEDD2. The difference in inner radius can be seen in the tracker layout in Figure 4.9. Double-Disks in TEDD1 are instrumented with 15 rings of modules, whereas the TEDD2 Double-Disks are equipped with modules in rings 4 to 15. The two Double-Disks of TEDD1 and the three Double-Disks of TEDD2, respectively, are virtually identical (only the third Double-Disk of TEDD2 show slight differences from the other two Double-Disks of TEDD2, related to the attachment of services at their periphery). To mechanically form disks and double disks from Dees, the

Dee has dedicated inserts. In the final assembly steps, the five Double-Disks of a TEDD will be mechanically connected by eight longitudinal bars at the outer radius and an inner tube at the inner bore of the Double-Disks. Four additional support rings will be mounted to the longitudinal bars between the Double-Disks to increase stiffness. Figure 5.9 shows the CAD model of the TEDD after the last assembly steps. In order to mount the inner tube and the longitudinal bars the Dees are equipped with inserts at the outer and inner edges. For the construction of two end caps a total of 40 Dees are required of which 8 odd and 8 even will be produced by DESY and 12 odd and 12 even will be produced by Lyon.

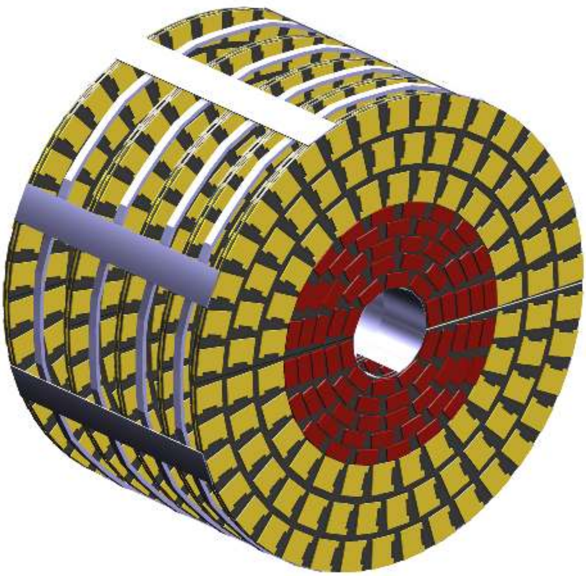

Figure 5.9. | Simplified CAD model of a TEDD after the last assembly steps.

In contrast to the end caps of the existing CMS tracker and the future tracker of the ATLAS experiment, the TEDDs do not consist of a global mechanical skeleton to which local support structures are mounted, but the Dees are a substantial part of the overall mechanical structure. This design has potential to minimize the amount of passive material needed to provide the required stiffness of the TEDDs. However, there is a drawback on the assembly of the TEDDs. The assembly of a TEDD can only start when all five needed Double-Disks are fully integrated, which in the current scheduling requires approximately 3 months.

Definition of TEDD Coordinate System

The TEDD coordinate system, summarized in Figure 5.10, follows the CMS convention of a right-handed coordinate system, centered on the interaction point (IP), with the x-axis pointing towards the centre of the LHC ring and the z-axis aligned with the beam and pointing towards the Jura mountains (i.e. counter-clockwise when viewing the LHC from above). Double-Disks are numbered from the IP outwards, with a sign corresponding to that of their z coordinate (1,2,3… for TEDD+ and $-1,-2,-3\ldots$ for TEDD-).

The two TEDD endcaps are mostly related through a 180° rotation around the y-axis. This symmetry is valid for the dee mechanics (inserts, cooling pipes, etc.) as well as for the positions of modules. However, the numbering of service channels and division of modules into readout groups follows a mirror symmetry around the transverse (xy) plane, because of constraints from the L1 trigger. As a result, the design of services on the dees does not follow the rotational symmetry between the positive and negative endcaps.

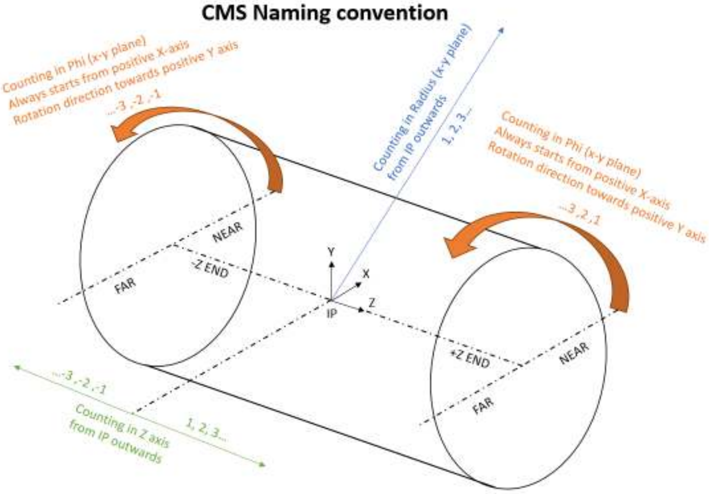

Figure 5.10. | TEDD coordinate system.

5.3.1. Half-Disk Support Structures - Dees

Both the odd and even TEDD1 and TEDD2 Dees are highly integrated CFRP (Carbon Fibre reinforced polymer) sandwich structures with the following embedded features:

- cooling and positioning inserts for 2S modules,
- Carbon foam heat spreaders for PS modules,

- positioning inserts for PS modules,
- inserts for connecting two Dees to form a Disk,
- inserts to connect even and odd Disks to form a Double-Disk, and to mount the support ring for the electrical and optical patch panels,
- inserts to mount the longitudinal bars,
- inserts to mount the inner half-shells,
- inserts accessible from both sides of the Dee that define the coordinate system of the Dee.

As previously mentioned, cooling of the Silicon sensor modules is achieved via evaporative CO_2 cooling. Six cooling pipes arranged in overlapping sectors are embedded in each Dee. The pipe of the cooling sectors are routed in two tiers inside the sandwich structure in order to allow for a crossing of cooling pipes from neighboring sectors without the need of pipe bending in the out-of-plane direction.

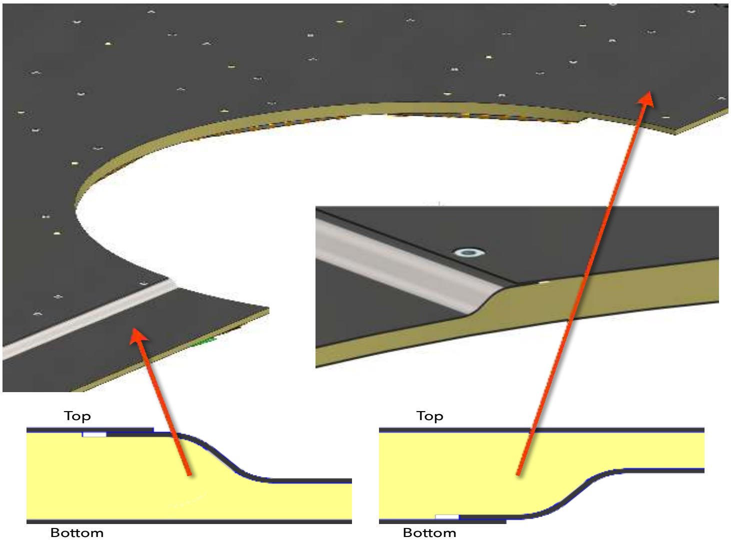

Figure 5.11. | Detail of the Dee showing the step in thickness to the overlap region.

To ensure full coverage with sensor modules within the rings, the edge of the Dee at which it connects to the other Dee in a Disk requires to have a step with a reduced sandwich thickness. This part of the Dee is called overlap region. In order to minimize the number of different Dee types all possible symmetries have been exploited in the design of the Dees. This results in the requirement that the step is on opposite sides as can be seen in figure 5.11.

5.4. Services Design

Services stand for the optical connection of modules to the DAQ, the electrical (LV and HV) connection of the modules and the cooling. It also includes some auxiliary items like the preheater on each cooling line, or sensors.

Services are routed radially on the dee surface to a first patch panel (called PP0) located at the double-disk periphery (see Figure 5.12). From there, longitudinal services are connecting the PP0 to the PP1 located near the tracker bulkhead.

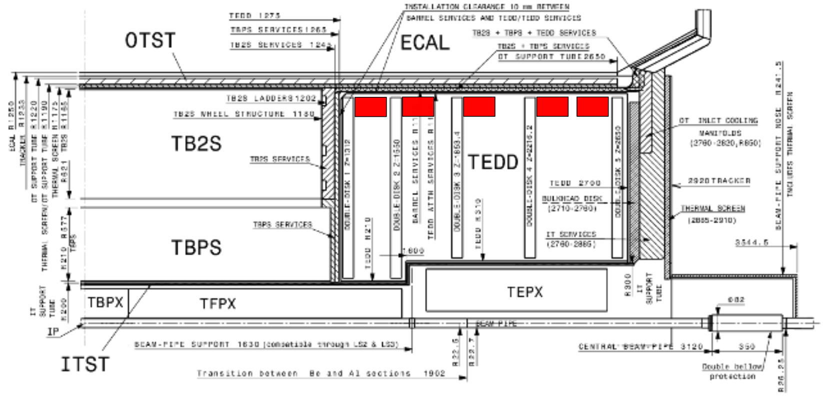

Figure 5.12. | Sketch of the PP0 location in the TEDD. PP0 regions are indicated as red boxes on the TEDD transverse view.

Modules are grouped in (naked) optical fanouts of 1–5 modules, themselves included in larger groups of up to 12 modules corresponding to a single multi-fiber bundle (MFB) also known as rugged fanout. The grouping of modules is driven by the L1 constraints and was derived by tkLayout [78]. Modules are also grouped in power groups. To facilitate the cabling and the commissioning, there is a one-to-one correspondence between the MFB grouping and the power groups. MFBs and power cables are routed to specific service channels following the mapping derived in tkLayout as described in Section 4.3.2.6.

Each double disk is equiped with 18 electrical and 12 optical patch panels, half of them attached to the top part and half to the bottom part, as aligned as possible with the corresponding service channel. Figure 5.13 shows a CAD view of the PP0 region with all services included.

Cooling loops of a pair of adjacent dees are connected in parallel to a cooling manifold next to the PP0s. From there, a single pair of cooling lines runs longitudinally to the proper service channel. This is discussed later in this section.

Details of the optical, electrical, and cooling connections for each module have been computed by a dedicated Python script, starting from the input from

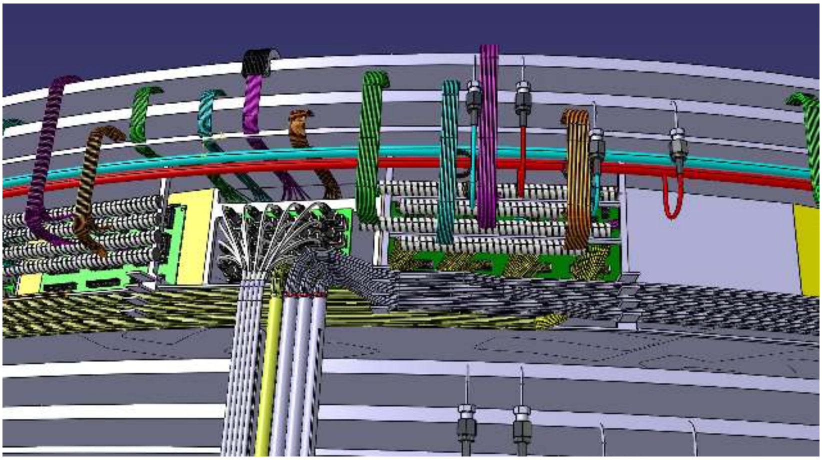

Figure 5.13. | CAD view of the PP0 region with the services included.

tkLayout and incorporating the technological choices specific to the TEDD (patch panels, optical fiber plant, etc.). All the information is grouped in a single PANDAS [83] dataframe stored in the json format. Table 5.1 shows the database fields available for each module. Note that some fields are redundant but their inclusion makes the processing simpler and eliminates the need of any additional calculation to determine the various connections in the TEDD.

5.4.1. Module numbering and symmetry considerations

The convention adopted for module numbering follows that of CMSSW. They can be designated either by their detid (detailed in Table 1.1), which is unique in the whole tracker, or by their position on the dee, as <`ring idx`>-<`phi idx`>.

The rings are counted inside out, ranging from 1 to 15 in TEDD1 and 4 to 15 in TEDD2. For both TEDD1 and TEDD2, odd rings are located on the dee closest to the IP. Within a ring, modules are numbered clockwise from the x axis (see Figure 5.10), alternating between the two sides of a dee. In other words, module 1-1 of TEDD1 dees is therefore on the inner surface for TEDD- and on the outer surface for TEDD+, while module 1-2 of TEDD1 dees is on the outer surface for TEDD- and on the inner surface for TEDD+.

The positions of modules on the top and bottom dees of a given disk are identical since disks possess a 180° rotational symmetry around the z-axis. In addition, the module positions in the positive and negative endcaps are related through a 180° rotational symmetry around the y-axis. However, due to constraints driven by the L1 trigger, service channels and definitions of power and readout groups do not follow these rotational symmetries but only satisfy a mirror symmetry around the xy plane. As a consequence, the design of dee services (power and optics), discussed in Section 5.4.2, is identical between

Table 5.1. | Fields available in the TEDD cabling database.

	Field	Comment	Example
Module	detid	Unique module ID as in CMSSW	411571240
Position	section	TEDD 1 or TEDD 2	TEDD_1
	side	+/-	-
	layer	1,2,3	2
	surface	1→4	2
	assembly_position	based on the detid	1-10
	ring		1
	assembly_phi		9
	rho		259.78
	z		-1541.62
	phi		171
	coolingLoop	1→6	6
Module type	type	PS/2S	PS
	sensor_spacing	in mm	4
Optical cabling	MFB	"multi-fiber bundle"	42040
	OPT_Services_Channel		-7 B
	MFC	"multi-fiber cable"	1403
	MFC_type		PS10G
	pigtailLength	length of the optical pigtail	150
	fiberlength	in mm, from CAD	2053.92080000676
	trunklength	fixed	100
	fanoutType	defines the actual fiber length	2.1
	fanoutbranchLength	rounded naked fanout fiber length	2200
Power cabling	PWR_Services_Channel		-7 A
Optical PP0	oPP0	optical PP0 name	TEDD_1-2_7
	oConnector	column in optical PP0	0
	oFanoutFiber1	fibers occupied on PP0 side of naked fanout, 0→11	3
	oFanoutFiber2		4
	oMFBFiber1	fibers occupied on PP1 side of rugged fanout, 0→23	5
	oMFBFiber2		17
	oSlot	row in optical PP0 (∼surface), 0→3	2
	oRuggedFanoutBranch	0→3	1
Electrical PP0	ePP0	electrical PP0 name	TEDD_1-2_7A
	eConnector	power group on ePP0, 0→3	0
	lvpPosition	pin LV+, module side	16
	lvnPosition	pin LV-, module side	15
	hvPosition	pin HV, module side	8
	lvpOutput	pin LV+, PP1 side	23
	lvnOutput	pin LV-, PP1 side	24
	hvOutput	pin HV, PP1 side	4
Sector test	sector	sequence number	2

any near surface of TEDD+ (facing the IP) and the away surface of the same Disk of TEDD- (and vice-versa). In total, for what concerns dee services there are therefore eight different dee designs (or 16 different dee surfaces) for the complete TEDD (both endcaps).

5.4.2. Dee services

This section will first describe the services that rest on the dee surface and their full connection chain from the modules to the counting room. Next, the methodology of the routing of the services will be explained. Last two subsections will summarize the analysis and validation studies done on the cabling design.

5.4.2.1. Optical chain

Each module is connected to the backend electronics through a pair of optical fibers. PS (2S) modules are equiped with an optical pigtail of 15cm (12cm), terminated by a MT ferrule that can bee seen in Figure 5.14. The pigtail is mated with a "naked fanout". A naked fanout regroups from one to five modules. It is equiped with MT ferrules on the module side and on the PP0 side and has a tree-like structure with 1–5 branches of variable length and a "trunk" of 10cm on the PP0 side. Fibers are protected with silicon spirals or loose plastic tubes[1]. Table 1.2 presents the different types of naked fanouts used in the TEDD. The large number of variants (57) results from the difficulty to accommodate the different fanout topologies on the dees.

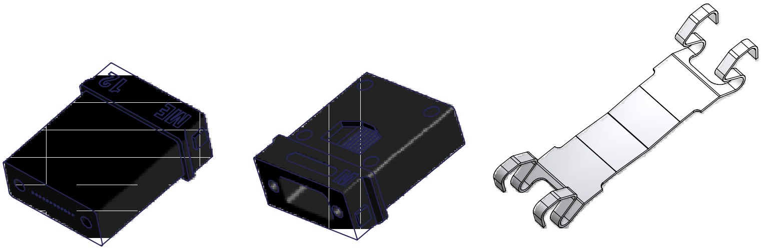

Figure 5.14. | MT ferrule (left) and spring clamp (right) used to mate the module pigtail and the naked fanout.

The optical PP0 is a passive component that takes the form of a 4xN grid equiped with MT to MTP adaptors (Fig. 5.15). The optical PP0 is organized in columns, each column corresponding to one optical group and being made of four rows. In the majority of the TEDD, one row corresponds to one surface

---

[1] While the exact design of the naked fanout is being discussed in the optics group, the silicon spiral option seems prefered at the time of writing.

(one side of one dee). Few optical group are made of modules from four different dees, in which case one row corresponds to one dee. This ensures that each naked fanout can be integrated and tested during the dee integration. Table 5.2 shows the number of column in each TEDD PP0. Figure 5.18 shows a rendering of an optical PP0 with fibers attached.

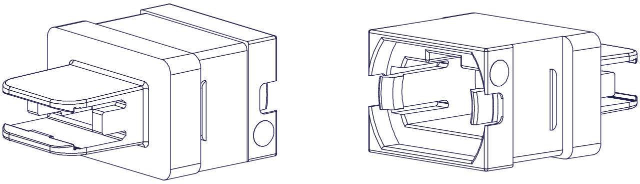

Figure 5.15. | MT to MTP adaptor located at the PP0.

Table 5.2. | Number of column in each TEDD optical PP0. The optical PP0 numbering corresponds to that of the OT service channels and is identical for the positive and negative sides.

Optical PP0	1	2	3	4	5	6	7	8	9	10	11	12
TEDD 1	5	7	5	5	4	5	7	4	5	5	4	7
TEDD 2	5	6	4	5	3	4	6	3	4	5	3	6

From the optical PP0, a "rugged octopus" groups the four rows into one single optical group of up to 12 modules and runs to the PP1 located near the tracker bulkhead. Rugged fanouts are described in more details in section 5.4.3. The full optical chain is summarized in figure 5.16.

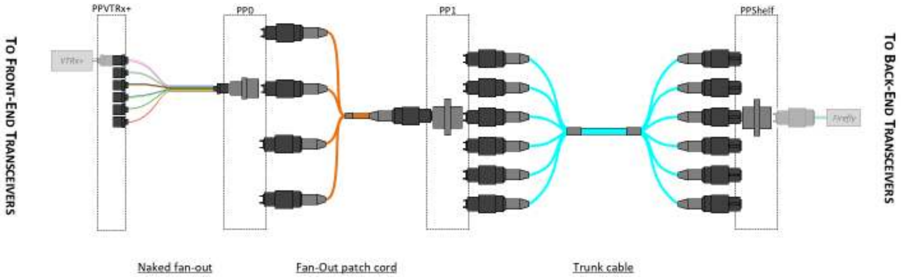

Figure 5.16. | Full optical chain, from the modules to the backend transceivers.

5.4.2.2. Electrical chain

Similarly to the optical services, electrical wires are routed on the surface of the dee to the electrical PP0 located at the periphery. This results in a large variety of length for the wires. To cope with this complexity, it has been decided to use a short pigtail of thickness AWG26 (AWG28) for the LV (HV) for easier manufacturing as well as reduced resistivity at the module connection level. The trunk of the wires will be made of AWG24 (AWG28) for the LV (HV).

The electrical PP0 then regroups modules from two dees to form power groups with the same grouping as the optical groups, for up to 12 modules. The input is made of one LV and one HV connector for each dee (therefore regrouping modules on both sides) and the output is one LV and one HV connector per group. It is designed to accommodate all the variations found in the TEDD: six modules from each of the dees (6+6), five from one and seven from the other (5+7), 4+8, etc. A small fraction of the power groups regroups modules from four dees, in which case a small intermediate connection is added just before the electrical PP0. All connectors used belong to the DF11 family, with varying numbers of pins.

The electrical PP0 exists in two variants, with either three or four power groups. The latter is depicted on Figure 5.17. Figure 5.19 shows a fully connected electrical PP0. Table 5.3 shows the size of each electrical PP0. It is a four-layers PCB, with 0.32mm of dielectric between each layer. The top and bottom layers contain the LV and HV lines, while the second (third) layer contains the LV (HV) ground plane and the preheater and temperature sensor lines. The LV line width is 50mil with a copper weight of 2oz. The spacing of LV lines is ensured by the dielectric over multiple layers. It is rated for 2.58A maximum. The HV line width is 15mil with a copper weight of 2oz. The spacing is 78mil (about 2mm).

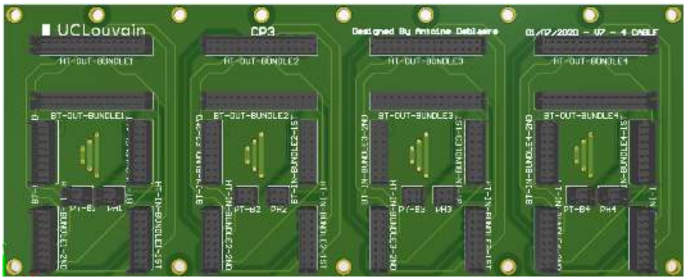

Figure 5.17. | Schematic representation of the electrical PP0 with four power groups. The two top rows of connector correspond to the input (connected to the PP1); the modules connect to the bottom (outputs).

Table 5.3. | Number of power group in each TEDD electrical PP0. The numbering of PP0s corresponds to the OT services channels for the +Z and -Z side respectively. The ordering of PP0s on the negative side reflects the rotational symmetry of the services channels.

Electrical PP0	1A	2A	2C	3A	4A	4C	5A	6A	6C	7A	8A	8C	9A	10A	10C	11A	12A	12C
	-6C	-5C	-5A	-4C	-3C	-3A	-2C	-1C	-1A	-12C	-11C	-11A	-10C	-9C	-9A	-8C	-7C	-7A
TEDD 1	3	4	3	4	3	4	3	4	3	4	3	4	3	4	3	4	3	4
TEDD 2	3	3	3	3	3	3	3	3	3	3	3	3	3	3	3	3	3	3

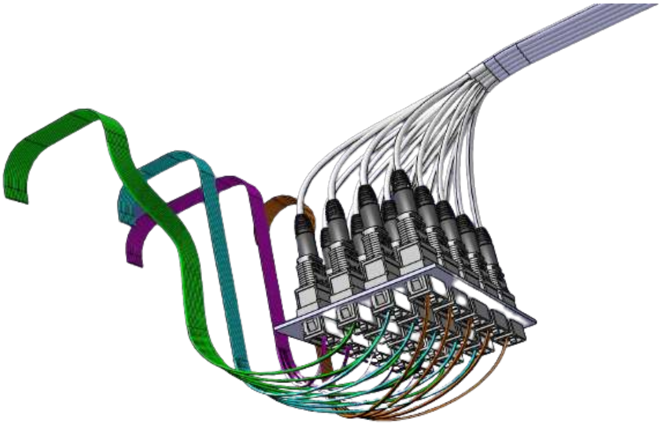

Figure 5.18. | CAD view of an optical PP0 with the tails of the naked fanouts coming from the four surfaces of a Double Disk on the left, and the rugged fanouts going to the PP1 on the right. In reality, the space below the PP0 will be used to cope with the fiber length in excess by looping the fanouts on themselves.

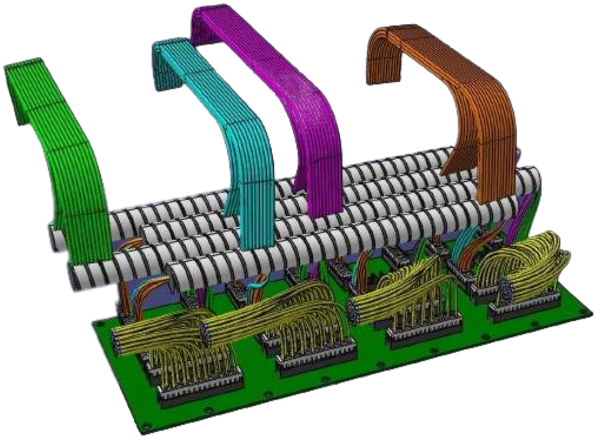

Figure 5.19. | CAD view of an fully connected electrical PP0. Cables coming from the four surfaces of a Double Disk can be seen in four different colors where the yellow cables are regrouping LV and HV for one power group into one cable.

5.4.2.3. Routing on the dee surface: Methodology

The routing of the services on the dee surface comes twofold: optics and power, where the case for the optical fibers is a highly constrained one and the case for the power cables is rather straightforward. In both cases, the fibers and the cables exit modules at precise locations and must be routed to the patch panels (PP0s) at the dee periphery. Both the grouping into optical groups and the location of the service channels are imposed by the L1-trigger design as explained in Section 4.3.2.6, yielding 8 (16) different disk (dee) layouts.

The routing has been obtained in two steps. First, the routes of the services was layed out according to the information from tkLayout using LaTeX with a user-defined library built on the tikz/pgf package. Second, FreeCAD (complemented with dedicated python-based macros) was used for further adjustments and for visualisation of the cabling in 3D.

The dee model drawn on LaTeX includes the full dee geometry, the module layout, and the locations of the inserts and of the PP0s. The script allows to route services by setting standard waypoints close to the module edges. The user-defined library makes it possible to chart the path of the fibers while imposing a minimum bending radius of 12mm. It also assigns a specific color to each fiber, and draws temporary cable holders at the endpoints of straight sections. Each individual fiber has been mapped by starting from the module and attempting to reach its endpoint at the (fixed) PPO location, while avoiding inserts and other modules along the way, and avoiding as much as possible excessive clustering or crossing of fibers in any given location.

The mapping of the power cables was done in a similar fashion, with two main differences: their minimum bending radius is smaller, and they are connected directly to the modules themselves as at the time of making the design the pigtail decision was not made. To avoid overcrowding the renderings and losing clarity, only one of the LV or HV power cables was drawn for each module respectively. The LV and HV cables of a given module will follow essentially the same path right up to the PP0s.

The routing of the optical fibers and power cables was completed for the 16 different dee surfaces of the TEDD [1]. Figure 5.20 shows one example of the resulting routing exercise.

Once the services have been charted using LaTeX, the drawings of the routes are exported as vector graphics. One example of this is shown in Figure 5.21. This is then imported on FreeCAD to generate CAD models as shown in Fig. 5.22. The model facilitates further detailed analysis of the services, such as:

---

[1] The module numbering on LaTeX is just a convention for ease of use. They are then converted to the regular numbering on FreeCAD.

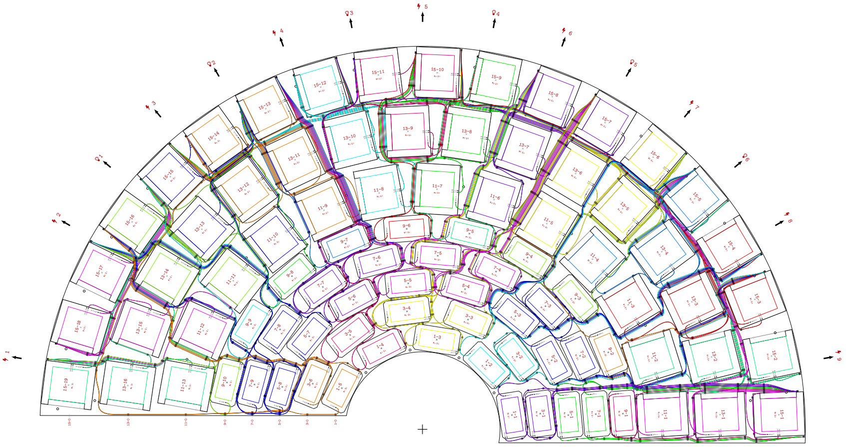

Figure 5.20. | Example of the services' paths on one dee surface (TEDD1, surface 1, top dee). Shown are the locations of the modules and the paths of the optical fibers routed from the modules to the periphery. The locations of the electrical (lightning bolts) and optical PP0s (light bulbs) around the dee is also shown.

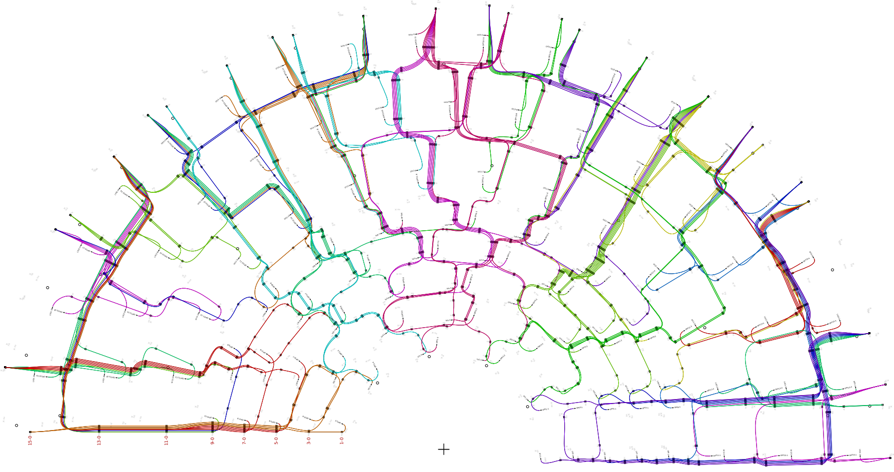

Figure 5.21. | Example svg file with path information to be imported in FreeCAD. The locations of the electrical (lightning bolts) and optical PP0s (light bulbs) around the dee is also shown.

- Checking the length of the fiber to guarantee that it is longer than the module pigtail (minimum length of 20cm (23cm) for 2S (PS) modules when including the VTRX+ and the MT ferrule).

- Measuring the bending radius at every point along the fibers, checking that the maximum curvature allowed for the fibers is never exceeded.
- Measuring the total length of the fibers and the cables.
- Automatically checking some routing rules, and the compliance with the predefined mapping to PP0s.

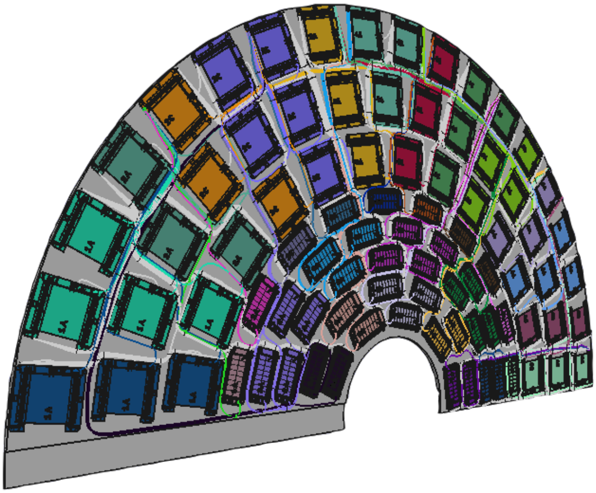

Figure 5.22. | Example of the CAD model of one dee with the transverse services. TEDD1, surface 1, top dee is shown.

It is best to outline the design evolution of the cabling as the process involves learning from studies and imposes updates on the design specifics. The electrical chain described in Section 5.4.2.2 was not the initial design choice. Mockup studies and the module integration considerations showed that the use of a short pigtail (5 cm) would be beneficial and that is why the pigtail choice was adopted. This did not imply a change in power cabling design as the pigtail can be accommodated in the already layed down path for wires.

5.4.2.4. Routing on the dee surface: Analysis

As mentioned in Section 5.4.2.3, dedicated python macros provide a detailed analysis of the routing once they are imported on the FreeCAD models of the corresponding dee surface. For each fiber route, the curvature at every point along the path is measured and plotted. In the cases where the bending radius is smaller than the imposed bending radius, 12 mm, a warning is raised. Figure 5.23 shows one example of curvature plot produced at this step. In the cases where a warning is raised, the curvature is fixed on FreeCAD to allow the minimum bending and this is further on validated with the dee mockup.

Second consideration in cabling analysis is the minimum pigtail length. This is measured for every fiber and some cases have been found to fall short in space to allow the imposed length. In these cases, the routing has been re-routed on LaTeXand the CAD model has been adapted accordingly. One of these cases is shown in Figure 5.29, which will be explained further in Section 5.4.2.5. However, the option to lower naked fanout multiplicity was dropped during the design studies because of manufacturing reasons. This implied that now there will be some slack to be absorbed at the PP0 connection level. This will be studied on the mockup as described in Section 5.4.2.5.

The last step of the analysis is the length measurement of all the fibers and the wires belonging to each dee surface. The length measurement of the fibers yield: the full length of each fiber route from the module to the optical PPO, individual lengths of each branch of an octopus belonging to an optical group (bundle) and the length of the corresponding trunk, and individual lengths of each wire route from the module to the electrical PP0.

The analysis of the services for sixteen dee surfaces of the TEDD was completed on FreeCAD for all three considerations described in this section. The length measurement of the fibers and cables yield the histograms in Figure 5.24 and Figure 5.25 for one full TEDD, respectively.

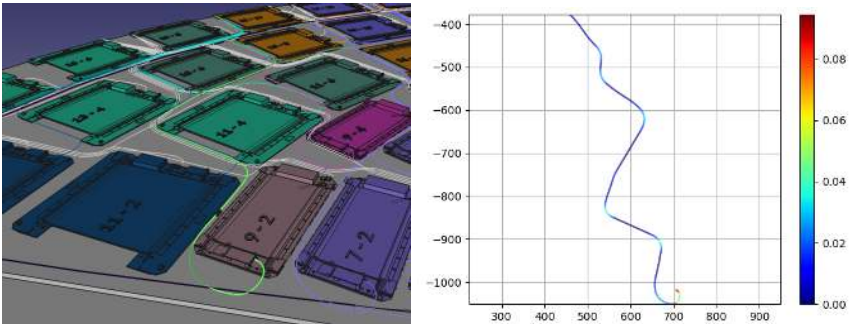

Figure 5.23. | Left: Close-up look on the visualisation of the optical fibers on a dee. The fiber emerging from module 9-2 is highlighted (including the pigtail and MT ferrule). Right: curvature plot produced by the CAD analysis macro, showing the curvature of the highlighted fiber at every point along its path. Large curvatures (red) correspond to small bending radii.

The overall summary of the analysis of all dee surfaces is that re-routing was necessary for a few cases to satisfy the pigtail length condition. The curvature considerations were easily justified for all cases and validated further on the dee mockup (see Section 5.4.2.5).

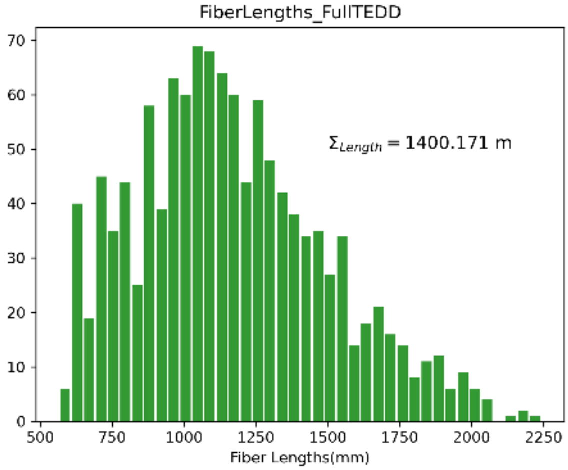

Figure 5.24. | Distribution of the fiber pair lengths (from the module to the PP0) for one complete TEDD.

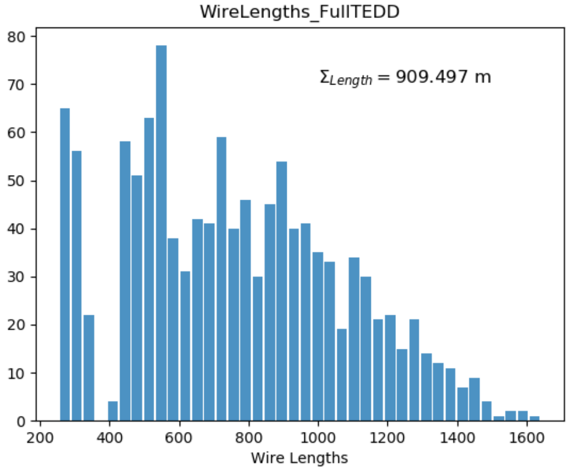

Figure 5.25. | Distribution of the wire lengths (from the module to the PP0) for one complete TEDD. The length presented corresponds to either the length of the twisted pair for LV or the length of the AWG28 HV wire.

5.4.2.5. Routing on the dee surface: Validation studies

The cabling design has been validated with the dee mockup shown in Figure 5.26. The mockup is made of PVC foam with the print of the layout of two first surfaces of first double disk of TEDD1. The modules are 3D printed from the simplified 3D models of the actual module design. The validation considerations are as follows:

- Validate the population of the fibers and cables on busy spots to make sure they can be accommodated without posing a risk to other considerations (inserts, contact with sensors or hybrids),
- Validate the curvatures that are already analyzed on FreeCAD and ensure that the bending is not risky (not smaller than 12 mm),
- Validate the measured lengths by laying down the route with a dummy sample and comparing the measured length in real life with the FreeCAD measurements,
- Validate the fiber and cable holder options in terms of shape, material, performance and location on the dee surface,
- Validate the fiber and cable population at the dee periphery for the connection to PP0s.

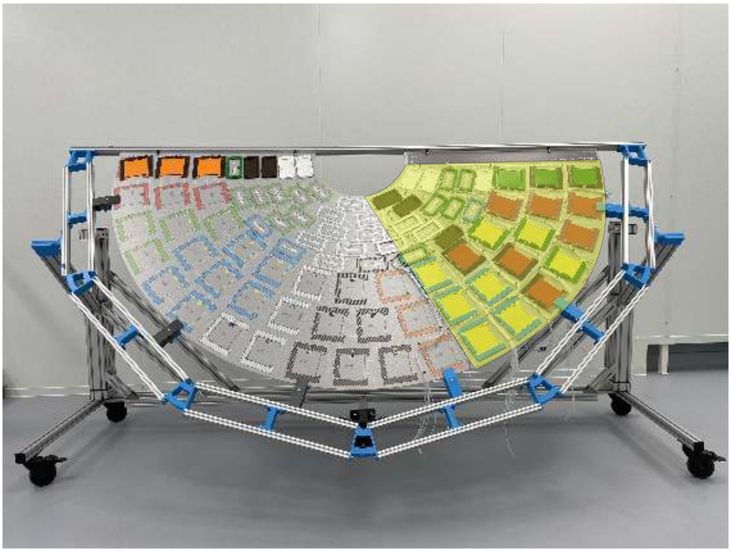

Figure 5.26. | The dee mockup on the dee integration table (the table in the picture is a temporary solution which will be replaced by the final design shown in Figure 5.2).

The mockup[1] shown in Figure 5.26 is installed with modules and services to

---

[1] There is a previous iteration of this mockup study that was done as the first validation

exercise the listed considerations. For the optical services, a spiral tube with an inner diameter of 1.5 mm and an outer diameter of 3 mm is used to replicate the optical fibers (spiral tubes are one of the choices on the table for the protection of the fibers). For the power cables, 24AWG dummy cable is used as a substitute. A close-up look at the installed section of the mockup is shown in Figure 5.27.

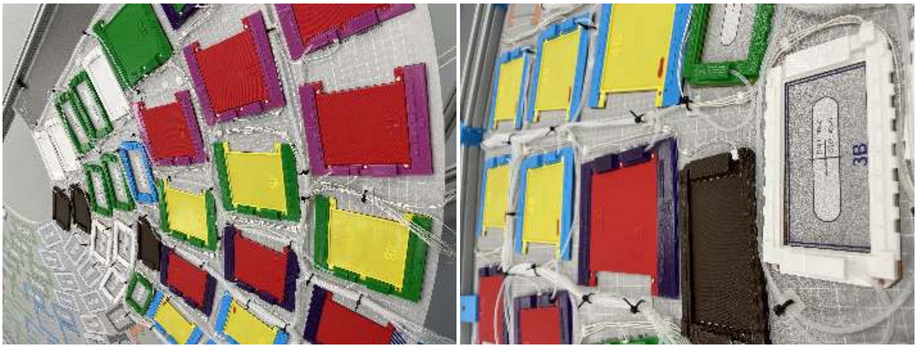

Figure 5.27. | A close-up look on the region of the mockup installed with services.

Cabling proved most challenging with the first two surfaces of TEDD1, as they house the largest number of modules and thus the largest number of cables and fibers to route. Dedicated studies of these areas have been performed on the dee mockup in order to validate the routing. The conclusion of this consideration is that the population can easily be mitigated by the choice of fiber/cable holders. If enough of the fiber/cable load bundled together, the busy spots do not pose a risk for the inserts on the way neither for the hybrids and sensors. This is, however, very closely related to the choice of fiber/cable holders. In total, three fixation options have been tested on the mockup; cable ties, straps and a 3D printed comb-like holder as can be seen in Figure 5.28.

Among the three, the cable tie and the strap were the most performant as both of them can host high cabling load while occupying minimal space on the dee surface. This is very advantageous in highly populated dees such as TEDD1 dees. The third option, comb-like holder, was considered for wires only and was found to be useful in certain areas when it is combined with the either a cable tie or a strap as the comb option can keep the shape of the route more strictly than the strap. Given that the curvature constraints are much looser for wires than fibers, using the comb and keeping the route as close to the cabling design as possible occupies less space on the dee surface. The drawbacks of

---

of the length measurement done on FreeCAD. The dummy fibers and cables were not representative of the final choice, therefore they are replaced. However, that study already showed an agreement between real life length and the FreeCAD measured length.

this custom option are that it is costly, the glue (or tape) needs to be added by hand, and requires additional irradiation tests for performance over time.

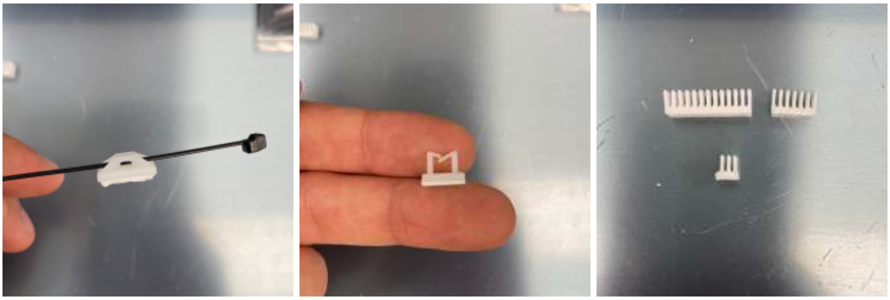

Figure 5.28. | Pictures of the tested cableholders. Left: cabletie used for spiral tubes (fibers). Middle: comb-like holder with variations depending on the cable load of the region. Right: m-shaped plastic strap.

The routing of the fibers belonging to the modules in the outermost ring of the Dees proved challenging due to the fixed length of the pigtails. In several cases the PP0 that the fiber is being routed to is very close to the starting point of the fiber. However, the direct and shortest route is not an option as it does not leave enough length for the pigtail. In these particular cases, the fibers are routed around a neighboring module to make a loop. Figure 5.29 shows two example of such cases.

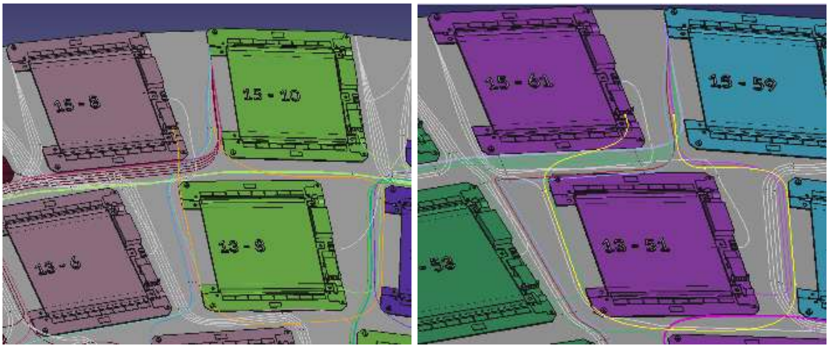

Figure 5.29. | Example of the looped fibers from module 15-8 (left) and module 15-61 (right).

The validation of the curvatures along the fiber paths are performed through 3D printed disks of radii 12 mm to 15 mm. The checks performed on software level showed that the highest concern lies at the module exit, when the fiber is leaving the module with a c-turn or a u-turn. These cases were, in majority of the cases, very easily fixable as the space constraints were still allowing an increase of the bending radius. The studies done on the mockup was focusing mostly on these cases and, including the busiest spots and dee edges, the minimum bending radius of 12 mm was satisfied. Figure 5.30 shows two examples of the checks done.

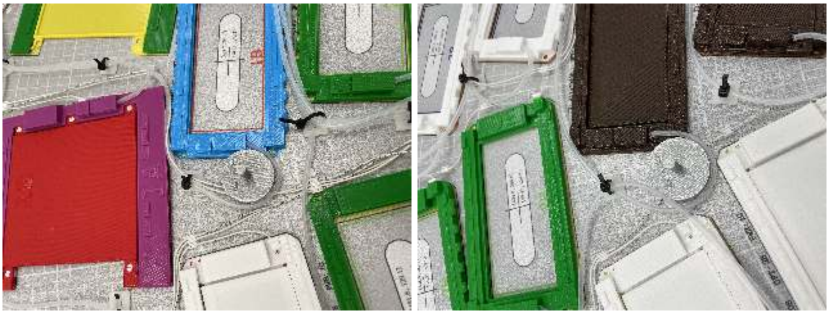

Figure 5.30. | The 3D printed disks are used at the bending points of the fiber path to validate the bending radius. Two examples of these checks are presented; 14 mm (left) and 15 mm (right).

At the time of writing, the validation of the PP0 connection of fibers and cables is being conducted. Yet another 3D printed solution has been designed to replicate the optical and electrical PP0 and mounted on the dee mockup according to the final detector design. The fiber and cable substitutes are connected at their endpoint in the PP0s according to the cabling map. Figure 5.31 shows how the study is performed.

This last study is being performed to validate the following points: length that is required to travel from the dee exit to the PP0 as well as the total length of the fibers and cables from the module to the PP0, the bending of the fiber trunks at the dee periphery, the population of this region and whether it poses any risks for other services, e.g., cooling. The finalization of the fixation options and their locations on the dee is ongoing at the time of writing.

5.4.3. Longitudinal services

Longitudinal services are cables and optical fibers connecting the PP0s to the PP1s outside the TEDD volume. They run longitudinally on the outer side of the TEDD volume and enter dedicated services channels in the bulkhead region (see Figure 5.32). They are maintained in the TEDD service volume by plastic gutters and straps. These gutters will likely by 3D-printed out of Accura 25 plastic, shown to be radiation-hard, which will make for a lightweight structure while allowing for design flexibility and rapid iteration. Each guide will house

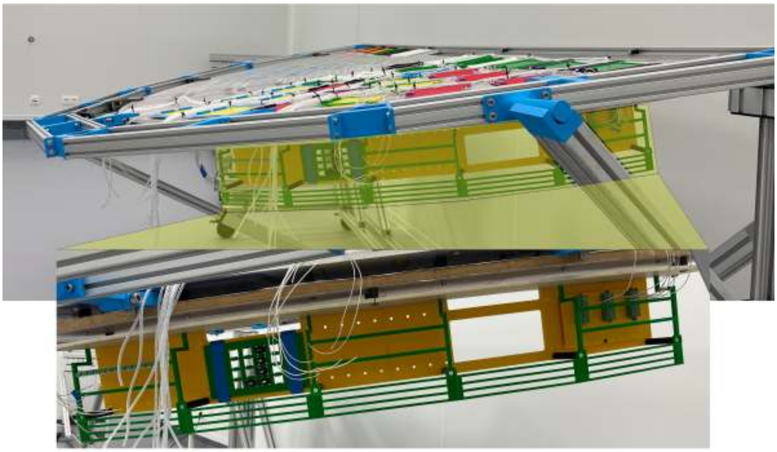

Figure 5.31. | The 3D printed PP0 on the dee mockup. Starting from the right edge, the first one is an electrical PP0, followed by an optical PP0 (fourth slot of the 3D printed structure).

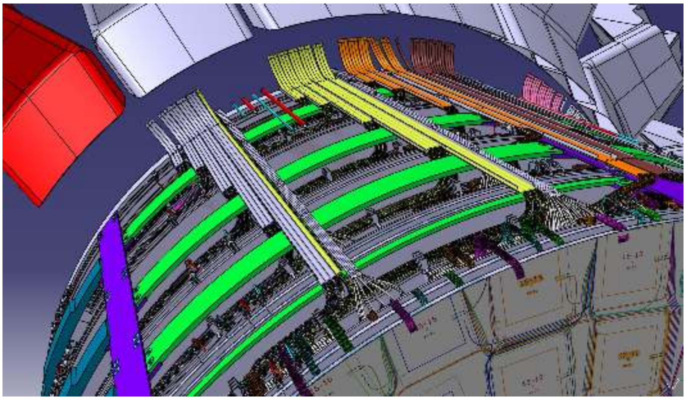

Figure 5.32. | Top: CAD view of the longitudinal services.

three to four cables, maintained using zip ties, and will be clipped or clamped to the beams and straps of the TEDD superstructure.

In the case of optical fibers, the longitudinal sections consist of the rugged fanouts. Rugged fanouts are connected to the PP0 via four MTP connectors. The four branches are quickly merged into one single fiber ribbon that runs towards the service channel. The rugged fanouts are defined by their topology (how the 4x12 input fibers are connected to the 24 output fibers) and by their length (that depends on the double disk). All the variants are listed in Table **??**.

In the case of power cables, these are multi-service cables regrouping LV and

HV for one power group, as well as one temperature sensor and one preheater. Each power cable has an outer diameter of 9.6mm. Part of the cable must be stripped from the outer shell to reduce the radius of curvature when it enters the TEDD volume close to the PP0.

5.5. TEDD Integration

As already mentioned in section 5.3, 16 TEDD1 and 24 TEDD2 Dees will be required for the integration of two endcaps. The production will be under the responsibility of DESY and IP2I Lyon, respectively. Figure 5.33 shows a simplified flow chart of the TEDD integration from Dee production to the TEDD assembly and testing. According to the current scheme eight tested TEDD1 Dees will be shipped to Louvain for integration, whereas eight and four tested TEDD2 Dees will be shipped to DESY and Louvain for integration, respectively. Eight of the TEDD2 Dees integrated at Lyon will be shipped to Louvain and the remaining four TEDD2 Dees will be transported to DESY for the subsequent assembly and integration steps. This way Dee integration is still distributed over all three TEDD institutes while the number of shipments of integrated Dees is reduced to a minimum.

As Louvain will be serving as an integration and testing center for the dees, a test procedure has been developed to ensure the functionality of the dee, its services, and the modules integrated. Section 5.5.2.1 describes this procedure. However, before arriving at dee integration, the modules produced in module centers require a burn-in to ensure reliability and good functionality. In this pursuit, Louvain cleanroom has been prepared for burn-in of the modules and this will be described in the next section.

5.5.1. Module Burn-in

Burn-in of electronics imply the testing of electronic components under the extreme conditions of the envisioned setup aiming to detect early failures as well as ensuring the performance. It is usually conducted in terms of power and temperature cycles (usually elevated values of temperatures and voltages) for a duration of as little as several hours to dozens of hours.

For the p_T modules of the TEDD, a burn-in system has been designed and built. At the time of writing, module production is yet to start and in the Louvain cleanroom there is only one functional module (functional module 7, FM7, registered as 2S_40_6_BEL-00007 in the tracker database). Therefore, this section will describe the design of the box and present the initial results obtained from the system in terms of system behavior and functionality.

The burn-in setup design specifications were such that the system can test 10 modules at the same time that are placed in the system in the final configuration of LV and HV for power and as well as optical readout. The nominal operating temperature of the modules is $-33°$C and the modules are expected to operate unattended going from room temperature to the operating temperature in about 4 to 5 cycles within 24 hours.

Realization of this test system requires the following major components: power

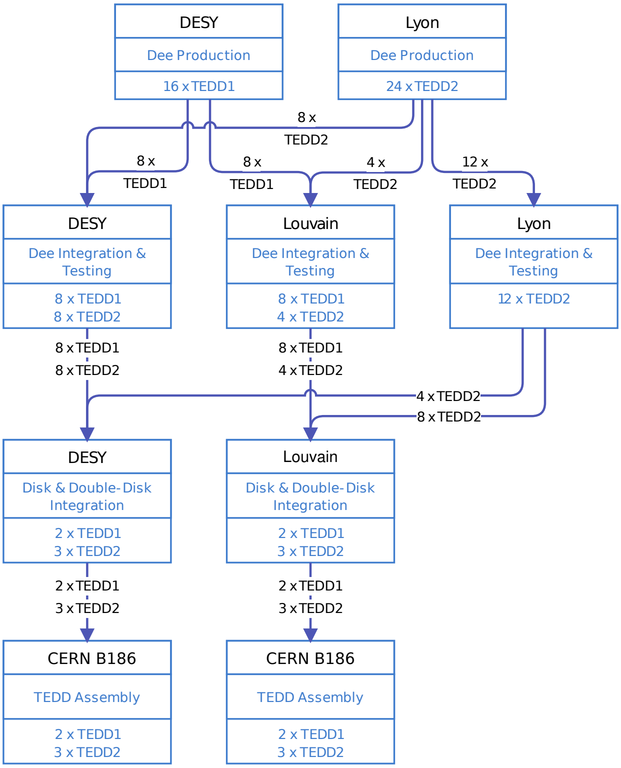

Figure 5.33. | Flow chart of the TEDD integration from Dee production to TEDD assembly.

supply, chiller, module support/frame, an enclosure, a controller board used to control the components of the system and automate safety considerations and sensor readings, and DAQ components. Therefore, the technical equipment listed and described in Section 5.1 (except the MARTA chiller) are benefited to operate this test system. The Louvain burn-in box has been assembled with these design considerations and the full list of components are as follows:

- Commercial EU-size refrigerator as the enclosure and a custom built module shelf hosting 5 modules at each row,
- Julabo FP-52 chiller for cooling,
- Donaldson Ultrapac as the dry air supply,
- CAEN power supply,
- Set of sensors:

  - RTD sensors for the temperature monitoring,
  - Vaisala DMT143 dewpoint transmitter for dewpoint monitoring,
  - BME280 and DS18B20 DiSCo sensors for temperature and humidity monitoring,
- Magnetic lock for the door of the box,
- DAQ equipment:
  - μTCA crate, FC7 and FMC boards, transceivers, fibers,
- Controller box, provided by Fermilab.

Most of the equipment listed above is kept in the technical room of the Louvain cleanroom. Therefore, a feed through between two rooms has been made to fetch the services from technical room to the clean room. This feed through allows in the cleanroom: the CAEN power supply cables, Julabo pipes, MARTA pipes for it to connect to its localbox in the cleanroom, and dry air pipes. These services coming from the technical room are then directed at the box via feed-through for pipes and a cabling hub for the cables. The feed-through and the cable hub is located on the top surface of the enclosure. The controller box is located on the same surface as well. The burn-in setup is shown in Figure 5.34.

At the time of writing the module shelves of the box is occupied by metal pads that carry heating foils aiming to imitate the heat dissipation of the modules. The pads are powered with CAEN LV power supply with 12 V. Figure 5.35 shows a close-up view of the slots of the module shelf. The heating pads are visible on the right surface of the metal pad. Another cable can be seen coming out of the left surface. These are analogue RTD sensors that are taped on the other surface for the monitoring of temperature cycles. Surface attachable RTDs (SA1 RTD) are used on the four corners of the module shelf and is read out by the controller box.

The burn-in system has been tested with several temperature cycles to observe and understand the behavior of the system. The cycle starts from room temperature with the set temperature being -30°C. The temperature of the metal pads, of the air in the box, Julabo internal and external temperatures, as well as dew point in the box is closely observed (along with other metrics like humidity and currents). The box takes about 2 hours to reach the desired cold temperature and then about 30 minutes to reach back the room temperature. These statistics have been achieved with a dry air supply of 20 litres per minute. Other configurations have been tested to see how the system behavior will change. Dropping the dry air supply by even up to 70% showed to have little effect on the cycle timing. Dew point levels never dropped below -50°C. Figure 5.36 shows a summary of temperatures and dew points in three temperature cycles.

The box has been tested with the functional module FM7 as well. The module

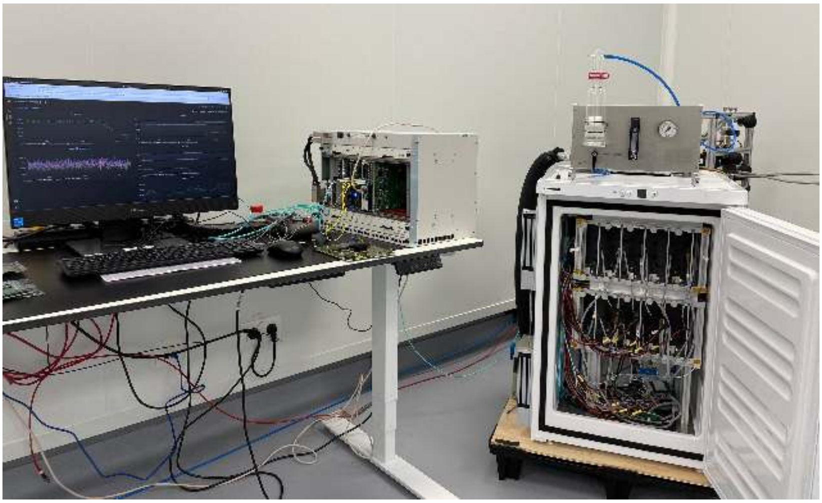

Figure 5.34. | A picture of the Louvain burn-in setup. The desk carries the user PC with the Phase-2 DAQ software, Ph2ACF, and access to the DCS/DSS dashboards. Next to the PC there is the μTCA crate with FC7s. To the right of the desk, the fully assembled burn-in box with the dry air control valve on top of it, shown.

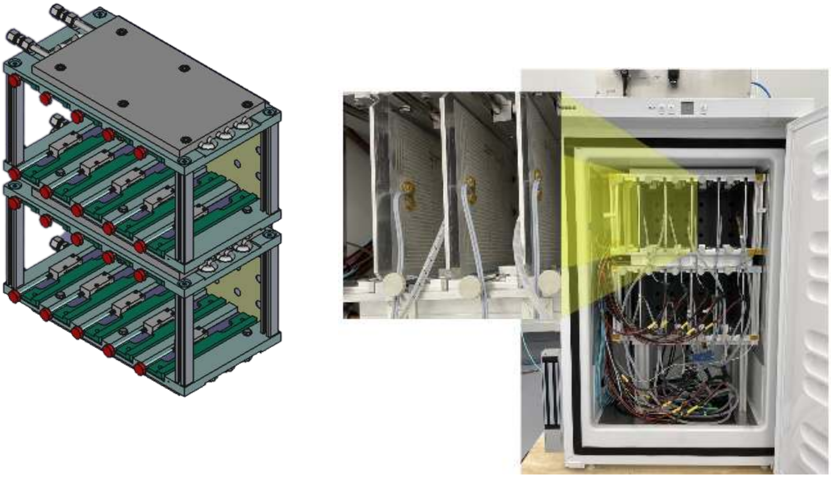

Figure 5.35. | Left: 3D model of the module shelf. Right: A close up picture of the Louvain burn-in box with the metal pads carrying the heating foils highlighted.

can be successfully read out as the full DAQ chain is in place and working.

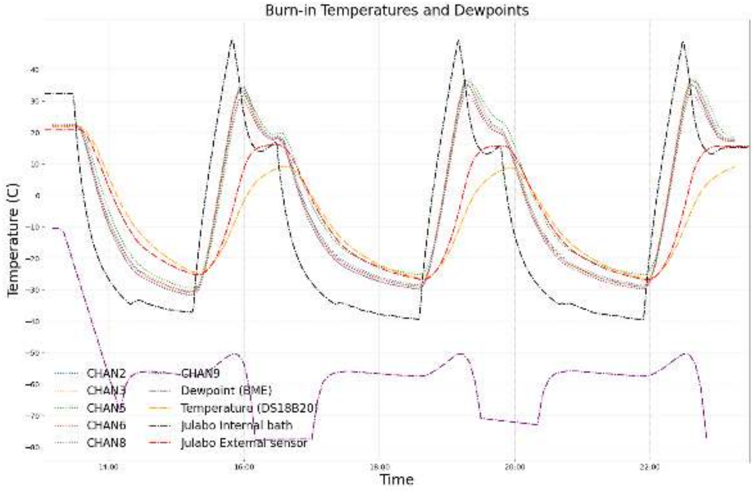

Figure 5.36. Temperatures and dew points during the temperature cycle of the burn-in box. CHAN* are the analogue RTD sensors taped on the metal pads, whereas BME280 and DS18B20 measures the values out of air. Julabo temperatures are measured with the device's own sensors (PT100).

Several noise scans have been performed while the module is in the box and powered with a LV of 12 V and a bias voltage of 300 V. The noise scan from when the box is cold, at -30°C showed a very good noise, ~ 7.5 Vcth. One example noise scan of the strips is shown in Figure 5.37.

5.5.2. Developing Integration Tests for the Dees

Once all modules have been integrated on a given dee, the dee will be subjected to a series of tests in order to verify that the modules still perform as expected. Those tests will require the dees to be actively cooled, thereby also validating the thermal contact between the modules and the dee surface. For that purpose, the dees will be placed into large insulated boxes, whose designs will differ between assembly centres due to varying space constraints in their respective clean rooms. Louvain cold box design will be described in the next section.

5.5.2.1. Sector Test

Sector division Powering a complete dee would require unrealistically large power supply, cooling and DAQ systems to be installed at the assembly centres. Therefore, only a few optical sectors will be tested in parallel, typically one sector. However, as the sector division in few cases leaves modules from the

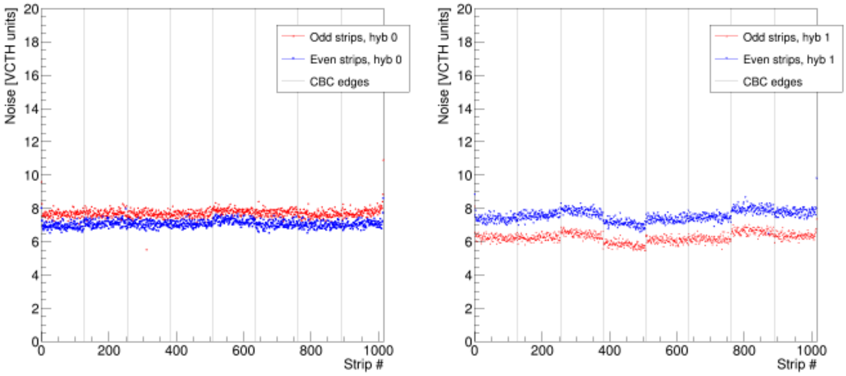

Figure 5.37. | Noise scans of the FM7 2S module. Both hybrids show a good noise of 7.5 Vcth. Odd and even stands for top and bottom strip sensors, where hybrid 0 is left and hybrid 1 is the right hybrid.

same optical group overlap with two cooling loops, cooling down two loops at a time is also foreseen. Regardless, once inside the box, all of the dee's cooling loops, electrical and optical sectors will be connected at the dee's temporary PP0s (tPPO) to respective pipes, cables and fibres emerging from an insulated feed-through. The tested sectors will thus be selected on the outside: for the cooling loops, a manifold and valve system will allow to select the loops to be used; for the electrical and optical services, connections will be configured at the level of temporary patch panels (tPP1s) which will be described later on in this section. This scheme will streamline testing operations as it removes the need to open the box (which requires a full thermal cycle and flushing the box with dry air again) when moving to a different set of sectors.

A division of dees into test sectors has been obtained using the following criteria:

- Only two cooling loops in contact with the selected modules;
- Maximum of 10 LV cables available at the cable plant;
- Total power draw/heat load below 300 W (limited by the power of the cooling plant, see;
- Similar heat load on the two used cooling loops.

The latter constraint takes into account the fact that significantly different heat loads on the two cooling loops could result in an imbalance in the pressure drops across the loops and in differing CO_2 flow rates in the loops, or in a loss of the two-phase condition of the CO_2 in one of the loops.

A prototype division of all dees (16 dees) into test sectors has been obtained by imposing the requirements listed above through a python script. Different MFB selections have been tested and chosen once an agreement with all selection criteria is met. For all dees, the above constraints can be satisfied by dividing the dees into six test sectors. Figure 5.38 shows, for an exemplary dee, how the modules are divided into test sectors. This division results in at most 33 modules powered in parallel (see Fig. 5.39). Figure 5.40 shows the total power consumption for all tests, as well as the absolute difference in heat load, for each test, between the two cooling loops.

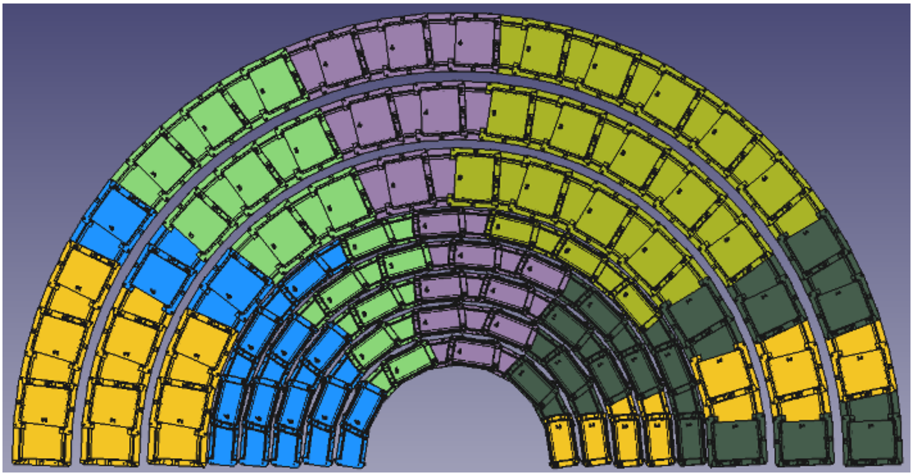

Figure 5.38. | Visualisation of the division of one full dee into six sectors for testing (modules on both front and back surfaces are visible). Each colour corresponds to one tested sector.

The official nomenclature (of the dees) is, as described before, a convention made by odd and evenness of the Dee. However, for this study, the naming chosen is more specific and follows the four surfaces of a double-disk; surface 1 being the closest surface of the odd dee/disk to the IP, surface 2 being the back of surface 1, surface 3 being the closer surface of the even dee/disk to the IP, and surface 4 being the back of surface 3. Figures 5.38, 5.39, 5.40 follow this naming convention.

The Louvain sector test cold box will be assembled on-site from commercially available insulation panels, cut to the required dimensions. The panels consist of a 100mm thick layer of fire-resistant polyurethane foam sandwiched between two steel sheets. Panels will be glued together to ensure proper tightness; in addition, the joints will be rigidified using inside profiles. To facilitate the placement of the dees, the box will feature a removable front panel, secured with magnetic locks, and a support for the dee arc frame at a similar height as the movable dee trolleys. Loading a dee into the box would therefore happen

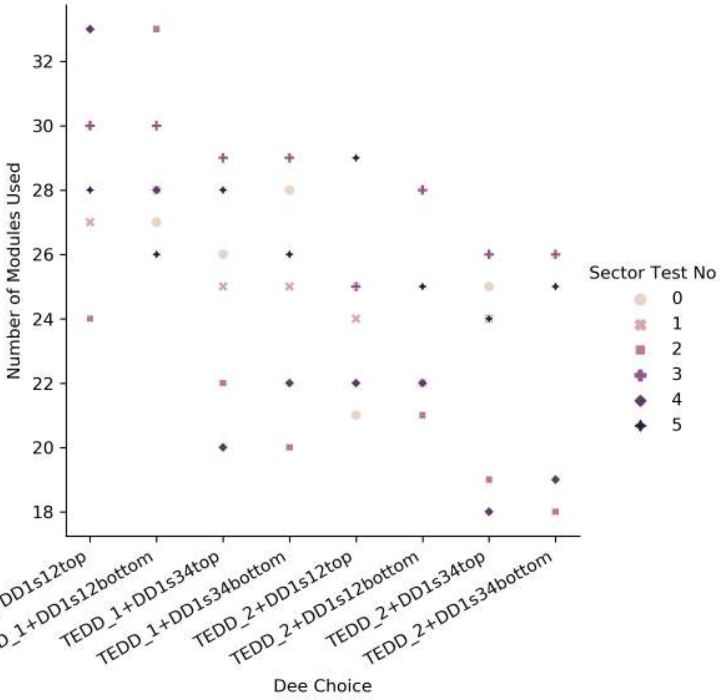

Figure 5.39. | Number of modules used in parallel for all sector tests, for different types of dees. Due to symmetry considerations, other dees inherit the same sector test division as those shown.

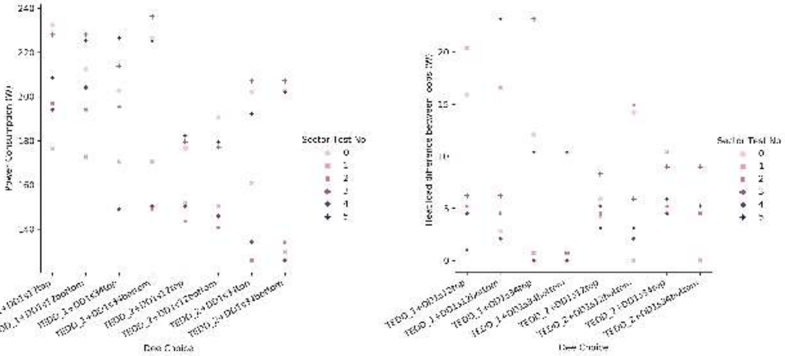

Figure 5.40. | Left: expected power consumption of all sector tests, for different types of dees. Right: differences in the heat load between the two cooling loops for all sector tests. Due to symmetry considerations, other dees inherit the same sector test division as those shown.

as follows: the trolley, with the dee and arc frame in vertical position, is moved in front of the (open) box; two operators then manually remove the arc frame from the trolley and place it onto the support structure inside the box.

A prototype box (Figure 5.41), of dimensions smaller than the final object (100cm × 60cm × 60cm externally), was built to validate the choice of materials, the assembly procedure, and the tightness and thermal insulation performance of the box. The final cold box is being manufactured at the time of writing.

Figure 5.41. | Prototype cold box being assembled in Louvain la Neuve. The door has been removed and is resting on top. The opening will eventually be in the front.

Running the sector tests will require a dedicated infrastructure which is very similar to the one that is used for burn-in setup. In addition to the cold box, the main pieces of equipment supporting the sector tests consists of power supplies (powering the modules), a chiller/heater (cooling down the test box, or heating it in case curing of the thermal interface material of PS modules is needed), a compact two-phase CO_2 cooling plant (MARTA), an air drying unit, and an FC7-based DAQ system. The test setup will feature several temperature and humidity sensors for monitoring the environment inside the cold box, and a hardware interlock system ensuring the safety of equipment and operators.

A solution has been developed for the connectorization between the integrated dees to be tested and the backend equipment. The solution is a rackable patch panel which will serve as the temporary PP1 (tPP1). There is the counterpart, temporary PP0 (tPP0), which will be connectorized inside the cold box. Not all groups will be tested in parallel: the selection of active power groups will be made at the level of the tPP1s.

The electrical tPP1 will consist of six units (1U racks). Each unit corresponds to one power group and is made of three inputs and one output. For the LV inputs, D-Sub 8w8 8-pin connectors (each feeding up to four modules) to be connected directly to the LV PSUs will be used. For the HV inputs, MB1GJN0600 female 6-pin sockets will be used (with max. five active pins, one of which for grounding), therefore allowing a similar grounding scheme to the final detector to be implemented (groups of four modules share a common ground). These HV inputs will be connected to an intermediate HV patch panel, used to fan out these groups of five HV lines to the individual SHV connectors on the HV PSUs. At most 10 out of the total 18 inputs to the tPP1 will be used at any time (therefore 10 HV and 10 LV input electrical cables will be needed). The output of a tPP1 unit will consist of one EDAC516 56-pin plug, cabled to the electrical tPP0s on the dee (DF11 connectors) using custom cables. Figure 5.42 shows a visualization of the electrical tPP1.

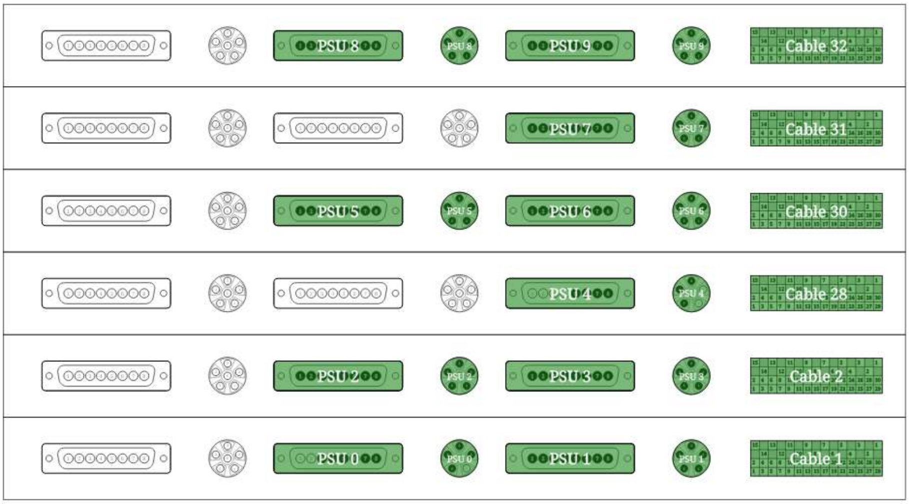

Figure 5.42. | Visualization of the electrical tPP1 for sector tests. Left are the input LV and HV connectors; the rightmost connectors correspond to the outputs to the tPP0s. The labels show an an arrangement for an exemplary sector test: the numbers indicate to which PSUs (for the input) the cables should be connected. Empty or solid pins in the input connectors show how many modules are powered by those cables.

The optical tPP1 will be used to break out the 12-fibre MPO patch cords connected to the tPP0s into the duplex LC fibres accepted by the DAQ backend. Commercial MPO-to-LC rackable adapter cassettes were the initial choice for connectorization. However, a less costly option was adopted where preseries rugged fanouts will be used along with a MTP24-to-LC adapter (from CERN). Figure 1.1 shows a visualization of the optical tPP1.

5.5.2.2. Test procedures

A likely sequence for the sector tests would be as follows:

1. Installation the dee in the cold box; full connectorization; securing the door; vacuum pumping the cooling loops (two out of six loops).
2. Connectorization of one test sector at the level of the tPP1s.
3. Flushing the cold box using dry air.
4. Testing the modules at room temperature.
5. Cooling the cold box and dee to -35°C.
6. Testing the modules.
7. Flushing the liquid CO_2 contained in the cooling loops back into the MARTA tank.
8. Re-cabling at the tPP1s and switching cooling manifold for the next sector.
9. Testing the modules.
10. Once all sectors have been tested, heating the cold box to room temperature.
11. Opening the box and moving the dee into safe storage (if all tests successful), or replacing failed modules and repeating the test.

The tests of the modules themselves would likely involve at the minimum:

- Temperature measurements, to validate the thermal interface between the module and the dee;
- I-V curves;
- Noise measurements. These can reveal issues with the grounding of the modules, the CBCs, the sensors, or the wirebonding.

5.6. TEDD Assembly

This chapter so far covered the details of the TEDD project in terms of design and testing procedures with a focus on the parts where the author had contributions. This section will now provide a summary of how the complete assembly of the TEDD will be conducted as well as the production planning in the assembly centres.

The building blocks of the TEDDs are the dees as already highlighted in this chapter. Therefore, what comes first in the assembly line is the dee production which will take place as summarized in Section 5.5, by DESY and Lyon. This will be followed by dee integration and testing where all three collaborators of the project contribute as can be seen in Figure 5.33.

Once the dees are integrated and tested, next step will be the disk and double-disk assembly. This step of the assembly line will be conducted in parallel between DESY and Louvain where TEDD+ and TEDD- will be assembled, respectively. The disk and double-disk assembly will take place on a dedicated system developed by DESY. Louvain will use the same system and the construction of this system is ongoing at the time of writing. Figure 5.44 shows the 3D model of this system.

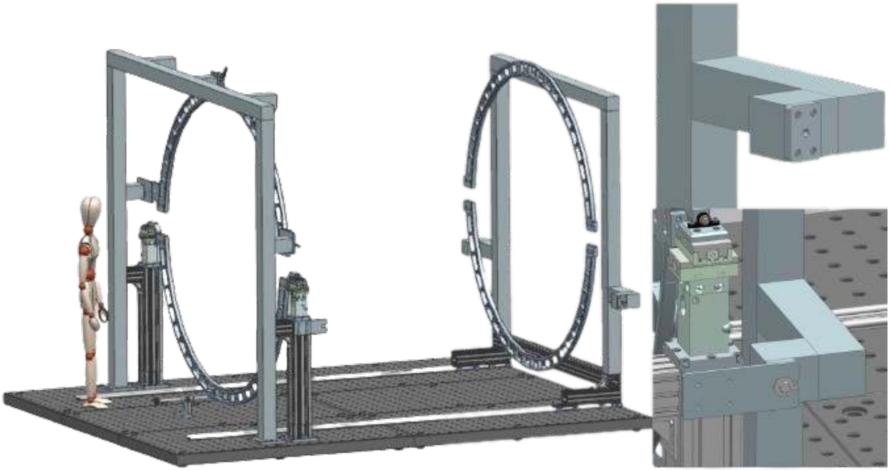

Figure 5.43. | The 3D model of the disk and double-disk assembly platform is shown. The very same system will be used in Louvain cleanroom and can be seen in Figure 5.1, left bottom corner of the room where a disk can be seen.

The disk assembly starts with the assembly of an even disk. The first step is the installation of an integrated and tested upper dee on the stage which is followed by the installation of the lower dee on the fixed portal. At this point a relative alignment is performed. The two dees are put together with the use of dee to dee inserts. The last step of the disk assembly is the connection of the arc frame. Once this is also done, the disk is put on the rail frame and moved into parking position. Same steps are followed for the odd disk of the given double-disk. Once the odd disk is ready with its arc frame, two disks are moved close to each other and the upper arc frame is disconnected while the relative alignment of the disks is done. At this point, disk to disk inserts are put in place to connect two disks to form the double disk. Then, the arc frames are put back to form arc rings around the disks.

To finalize the double disk assembly, the temporary patch panels put in place during integration and testing are removed. A patch panel ring that carries the final patch panels is installed and the module cabling is finalized. The assembled double-disks will be stored until the TEDD assembly. In Louvain, the cleanroom storage area already mentioned in Section 5.1 will be dedicated for this.

The TEDD assembly starts only when 5 double-disks of the TEDD are built and in storage. The procedure is already drawn out and it requires two tooling

Figure 5.44. | A picture of the disk and double-disk assembly platform. The picture is taken during a workshop organized between the TEDD project collaborators hosted by DESY.

setups: the DD alignment setup and the rotation setup for the installation of the services, both designed by DESY. As can be seen in Figure 5.33, both Louvain and DESY will assemble the double disks and assembled double disks will be transported to CERN B186 for TEDD assembly.

The double-disk alignment tooling comprises five sets of manual stages spaced apart by the nominal distances of the DD that allow to move each double-disk in 6 dimensions (X/Y/Z). The system is complemented by a tilt stage with threaded rods that extend inwards form the front and behind the TEDD. The double-disks are aligned with respect to each other by the use of this system. The alignment system can be seen in Figure 5.45.

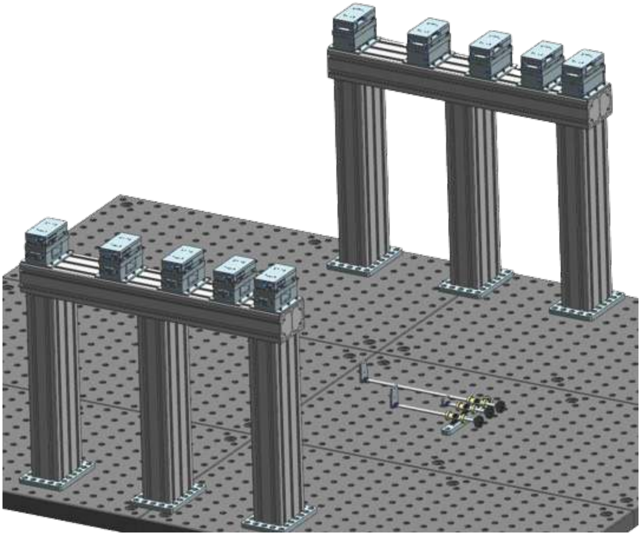

Figure 5.45. | Conceptual design of the DD alignment tooling. The X/Y/Z stages are placed apart by the nominal distance of the DDs. The tilt stages for the first three DDs are shown, the other two DDs will be controlled in the same way from the back side.

After the double-disk alignment, next step is the installation of mechanical superstructure and the longitudinal services. The superstructure and the inner tube will be installed in a fashion not to create any mechanical stress to the disks. The beams of the super structure will be installed while the arc frames are still in place. However, for the longitudinal services, the arc frames have to be removed as the fingers are in the way and a rotation mechanism is needed to be able to provide access to the TEDD without having to work on top or below the TEDD. Therefore, a central bar that supports the TEDD at the location of each double-disk will be inserted into the inner tube. This bar will be able to rotate around the central axis. The bar design can be seen in Figure 5.46.

5.7. Personal Contributions

As the PhD student of the tracker upgrade project in Louvain, I contributed to the upgrade activities in different fronts; the cabling design of the dees, developing a slow-control system, commissioning of test setups, as well as presenting at an international conference, FTDM 2022 and 2023, first a poster and then a plenary talk, respectively.

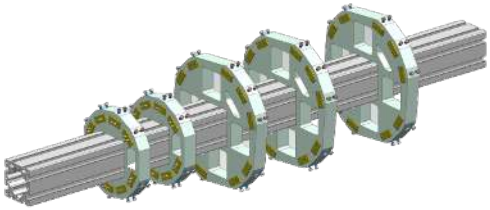

Figure 5.46. | The 3D model of the central bar of the rotation tooling.

I have made significant contributions to the CMS Tracker Phase 2 Upgrade through my work on the services design of the new detector. Specifically, I focused on the cabling design of the Dees which involved both optical and electrical cabling for 16 different Dees that form a complete endcap as well as the validation of this design with a mockup. I contributed to the development of DiSCo project through firmware development of the microcontroller; implementation of the sensor readout, building of the data pipeline to publish data to the database, creating the dashboards for environmental conditions, and the documentation of the system as well as presenting in internal TEDD meetings. My final contribution to the upgrade project is on the development of the test systems and procedures. I was in charge of ordering of the components of the burn-in system, took part in the assembly of the system and obtained the first results through temperature and power cycles. On the same topic, I contributed to the design of the sector test of the integrated Dees: optimization of the back-end equipment used, as well as determining which modules to be tested at the given step of the sector test.

5.8. Discussion & Outlook

In the services design, I utilized tools such as LaTeXand FreeCAD to create a software-level representation of the cabling design and this allowed me to conceptualize and plan the layout of the optical and electrical cables on the Dees. By working at the software level, I was able to make initial considerations and ensure that the design met the necessary requirements and specifications. To validate the design and further assess its feasibility, I moved on to creating a mockup of an actual Dee. This step enabled me to physically visualize and evaluate the implementation of the cabling design, required me to learn new tools such as 3D design and printing. Through this validation process, I have gained confidence that the considerations and decisions I made during the design phase were well-founded and that the overall design is in good shape.

The choice of tools were inherited so their justification will not be very elaborate.

However, as a first year physics PhD student I found the choice quite fitting as LaTeXcompared to any CAD software would be my first choice. Having been able to work on this on an environment that I am very used to have helped me progress faster than I could progress in any other software. The second step of the design was performed with FreeCAD as it is a fairly easy, open source CAD software that is recommended for mechanical design. I personally do no have experience with CAD before this project and I find FreeCAD user friendly and accessible.

At the time of finalizing of this thesis, a pre-integration test is being held at DESY to study the integration with prototype modules. Figure 5.47 shows a partly installed Dee with modules. The first findings are showing that the cabling design holds successful and that following the design guidelines, the operator does not have problems or unexpected issues integrating the module on the dee.

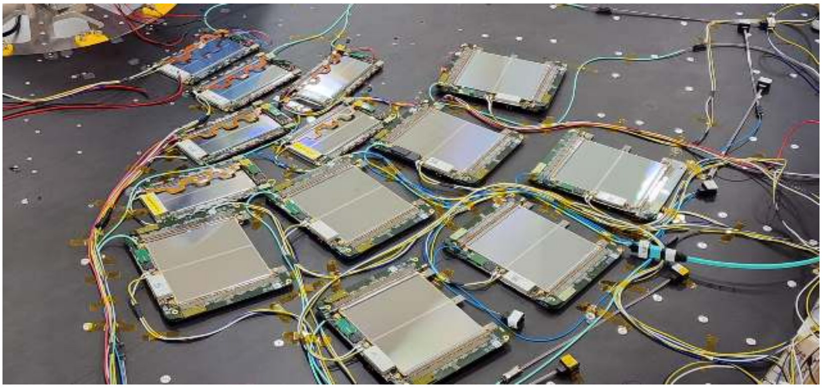

Figure 5.47. | Picture of a partly installed TEDD1 odd top Dee from the pre-integration test at DESY.

The design choices behind the DiSCo project were made such that it's cost-effective and highly customazible. This enables easy production and deployment of the system which is a major advantage for a small-scale laboratory. In comparison to the SCADA systems used in big experiments, e.g. WinCC OA for the CMS DCS system, the DiSCo system lacks reliability as it runs on open source cloud systems that did not necessarily go through rigorous testing and certification procedures as the standard, commercial SCADA systems. The DiSCo system runs on one basic data pipeline where there is no room, at the moment, for redundancy in case of a failure. Over the past year there were two cases where one of the boards deployed at the cleanroom stopped publishing data and we had to restart the module without being able to diagnose what caused the failure. Other advantages of the system are that it provides real time monitoring and visualization and it is scalable; the plan is equipping all test systems with a DiSCo board. The last aspect of the project which can be considered a disadvantage is the safety aspect. The DiSCo chips can be programmed with interlock logic that can kill a running equipment, e.g. in case of observation of unusual environmental conditions. This, in comparison to large scale experiments, lacks reliability once again as it depends on the sensor data with no redundancy. Overall, the system offers cost-effectiveness, ease of deployment, flexibility, and real-time monitoring. However, it may face challenges in robustness, reliability, and security when compared to SCADA systems used in big experiments like CMS.

In the broader context of tracker detectors and the CMS experiment, my work on the services design of the CMS Tracker Phase 2 Upgrade project contributes to the advancement of detector technology and the overall goals of the CMS experiment. My other contributions to the project, test setups, DAQ, and lab commissioning was crucial in facilitating the smooth evolution of the project as well. Efficient and robust cabling designs are crucial for ensuring reliable data transmission, signal quality, and optimal performance of the tracker detectors. Hopefully, my contributions through this channel help pave the way for enhanced data collection, accuracy, and precision in the CMS experiment.

6. Chapter

Higgs Pair Production at the HL-LHC

As described in Chapter 4, one of the main motivations of the HL-LHC upgrade is the search for Higgs pair production. So far, this dissertation covered the details of the design of the upgraded CMS detector and other series of upgrades necessary to accommodate the HL-LHC. This chapter is therefore dedicated to a prospective study exploring the Higgs pair production at the HL-LHC in an effort to validate and motivate the design and performance of the future detector. The first series of analyses performed with the same goal were published in the Yellow Report 2018 [84]. The analysis that will be described in this chapter, however, was conducted within the Snowmass 2021 campaign aiming to improve on the results from the Yellow Report and to validate the expected detector performance further. The analysis searches for Higgs pair production in the $WW\gamma\gamma$ and $\tau\tau\gamma\gamma$ final states with the author as its contact person. Although the analysis strategy was largely inherited from the corresponding run 2 analyses [85] ($\tau\tau\gamma\gamma$ run 2 analysis is not public yet) , the author played a major role in all steps of the analysis from sample production to result extraction making sure that the strategy is aligned with the HL-LHC conditions.

6.1. Prospects for HH measurements at the HL-LHC in the $WW\gamma\gamma$ and $\tau\tau\gamma\gamma$ final states

As described in Chapter 1, the investigation of Higgs pair production is of utmost importance for our current and upcoming physics programme as it plays an important role in the Higgs property and precision measurements. Among these properties, self-coupling (trilinear coupling) λ of the Higgs boson is of even greater interest as it can be a portal to our understanding of a very fundamental question; why the Higgs field acquires a vacuum expectation value, fills the universe, and gives mass to all elementary particles. According to the SM, HH production has a very small production rate (more than one thousand times weaker than the rate of H production), see Table 1.3. However, it can be drastically enhanced in many scenarios of physics beyond the standard model (BSM), making HH an interesting probe of new physics. This enhancement can be due to the existence of new particles produced at the LHC and decaying to HH (resonant production), or to indirect (nonresonant) effects due to new phenomena at energy scales not directly accessible at the LHC. In the latter case, these effects can be parameterized in a model-independent and theoretically consistent way using Effective Field Theories (EFT).

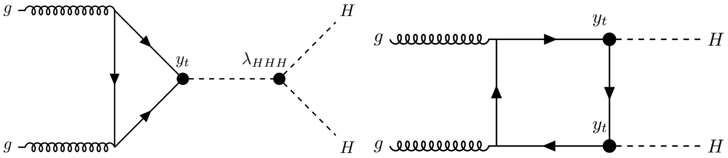

Figure 6.1. | Feynman diagrams for leading order Higgs boson pair production via gluon fusion.

The search for HH is a challenging task given its very small cross section compared to backgrounds with cross sections several order of magnitude larger. Having the highest cross section among all production modes (36.7 fb), the production via gluon fusion (ggF), $gg \rightarrow HH$, is the best motivated mode. See Figure 6.1 for the Feynman diagrams at the leading order (LO). Figure 6.2 shows the branching ratios of all possible HH decays where H → bb and H → WW decays stand out to have the highest and the second highest branching ratios, respectively. The first round of prospective analyses exploring the HL-LHC for Higgs pair production, the Yellow Report 2018 [84], included analyses from five decay channels. Table 6.1 summarizes these searches from both CMS and ATLAS and their combined significance on the HH signal strength.

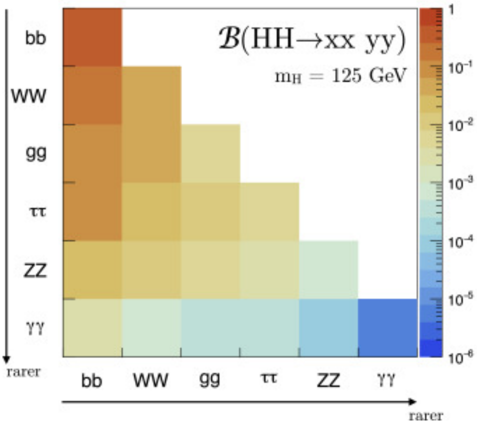

Figure 6.2. | Branching fraction of main HH decays assuming SM H boson [86].

In this analysis, a di-Higgs search in the WW$\gamma\gamma$ and $\tau\tau\gamma\gamma$ channels is performed in an effort to improve on the combined significance reported on [86], 4.0 σ with all systematic uncertainties included. The decay channels benefit from the sensitive $H \rightarrow \gamma\gamma$ decay which provides a clean and distinguishable signature consisting of a narrow peak in the invariant mass distribution of the photon pair

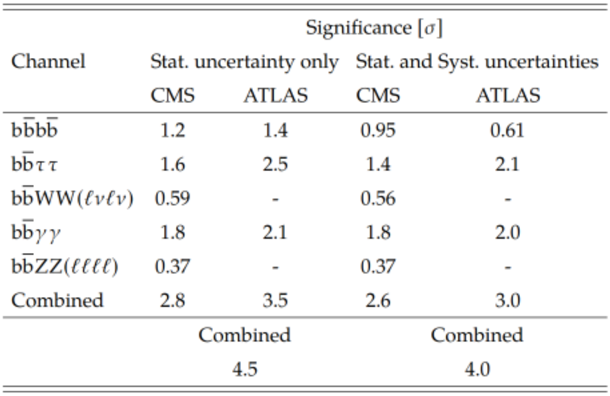

	Significance [σ]			
Channel	Stat. uncertainty only		Stat. and Syst. uncertainties	
	CMS	ATLAS	CMS	ATLAS
$b\bar{b}b\bar{b}$	1.2	1.4	0.95	0.61
$b\bar{b}\tau\tau$	1.6	2.5	1.4	2.1
$b\bar{b}WW(\ell\nu\ell\nu)$	0.59	-	0.56	-
$b\bar{b}\gamma\gamma$	1.8	2.1	1.8	2.0
$b\bar{b}ZZ(\ell\ell\ell\ell)$	0.37	-	0.37	-
Combined	2.8	3.5	2.6	3.0
	Combined		Combined	
	4.5		4.0	

Table 6.1. | Summary of the expected significance of individual decay channels and their combination, with and without systematical uncertainties being for both CMS and ATLAS experiments [86].

over a smoothly falling background. The second leg of the decay, $H \longrightarrow WW$ contributes a large branching ratio of 22%. This is the first study providing the expected significance numbers in these channels at a centre-of-mass energy of 14 TeV with integrated luminosity of 3000 fb^{-1} at the HL-LHC using events simulated with the Delphes [87] package.

In the WW$\gamma\gamma$ process, three final states are possible, as the W boson can decay both leptonically and hadronically: Semi-Leptonic ($WW \longrightarrow qql\nu$), Fully-Leptonic ($WW \longrightarrow l\nu l\nu$) and Fully-Hadronic ($WW \longrightarrow qqqq$) decay modes, where $l = e, \mu$ or τ. For the Fully-Hadronic decay mode, QCD induced processes are a major background and given the limited size of the Monte Carlo samples, this background is not well described. Hence, this final state is not considered in this study. The other two final states are tagged with separate selections and categorization, and their corresponding signal and background estimates are combined with the $\tau\tau\gamma\gamma$ channel to improve the overall analysis sensitivity. Table 6.2 gives a list of different final states that were explored.

Final States
One Lepton (exactly one lepton where lepton refers to an e$^-$ or a μ^-)
Two Leptons (at least two leptons)
One Tau (no electron/muon)
Two Taus (no electron/muon)

Table 6.2. | Final states considered in the analysis.

In order to optimize the sensitivity of the combined channels result, a DNN (Deep Neural Network) is employed for the One-Lepton and One-tau final states as they are expected to be the most sensitive due to the contribution from semileptonic channel where branching ratio is high from the hadronic W decay along with the benefit of maintaining a clean signature due to the presence of a lepton. A multiclass DNN is used to obtain the SM result. For the other final states, only a cut based strategy is followed.

It is imperative to apply orthogonal selections to all the final states mentioned above to avoid including the same events in multiple background categories. This is done via the event's number of leptons, where each lepton must pass a common set of selections applied for all final state tags. The Fully-Hadronic tag must contain exactly zero good leptons, the Semi-Leptonic tag exactly one good lepton, and the Fully-Leptonic tag at least two good leptons. For the final states with taus, two different categories are defined such that the final states include exactly one tau or two taus but no lepton. These background and signal models in different final state categories are combined to obtain the final result which benefits from a combination of the physics signatures of all possible final states.

Signal and background models are constructed independently for all the final states and results are obtained by performing a simultaneous likelihood fit to the invariant diphoton distribution, $m_{\gamma\gamma}$, among all final states.

Di-Higgs production has a predicted NLO gluon gluon fusion cross section of 36.69 fb at 14 TeV. The WW$\gamma\gamma$ and $\tau\tau\gamma\gamma$ channels have branching ratios of about 0.1% and 0.028% respectively. Since these processes have a possibility to be seen at the HL-LHC, the significance of the gluon gluon fusion production mode of the di-Higgs process in WW$\gamma\gamma$ and $\tau\tau\gamma\gamma$ decay modes and also the combination are provided.

6.1.1. Simulated samples

Signal Monte Carlo $gg \rightarrow HH$ samples are generated using Powheg v2 [88–91] at next-to-leading order (NLO) in QCD including the full top quark mass dependence with the SM parameters. Subsequent decays of the Higgs boson pairs into WW or $\tau\tau$ and a pair of photons are implemented using Pythia 8.212 [92]. The signal samples are generated separately for the three possible final states in $WW\gamma\gamma$. For $\tau\tau\gamma\gamma$ signal samples, all possible decays for taus are allowed.

The analysis is affected by backgrounds from single Higgs boson production and by non-resonant backgrounds with continuum $m_{\gamma\gamma}$ spectra. The event generator Madgraph5_amcatnlo [93,94] with the FxFx merging scheme [95] was used for the generation of the background from SM single Higgs boson production, including gluon-gluon fusion (ggH), vector-boson fusion (VBFH), associated production with a Z or W boson (VH) and associated production with a top quark pair (ttH) , while the top quark associated production with a

Higgs boson (tHq) was done using MADGRAPH version-2.7 at LO.

The continuum background contribution comes from various SM processes. Most of the dominant backgrounds across all the final states are due to the $\gamma\gamma$+jets processes that are modeled with the SHERPA v.2.2.1 generator [96]. γ+jets, QCD-induced processes and WW processes are modeled with the PYTHIA 8 [92] generator. Drell Yan and W production processes in association with photons and jets are modeled using MADGRAPH5 version-2.7 at LO. While $t\bar{t}$ are generated using POWHEG v2, $t\bar{t}W$, $t\bar{t}\gamma$, $t\bar{t}\gamma\gamma$, $Z\gamma$ are modeled using MADGRAPH5_AMCATNLO [93–95].

All signal and background samples are simulated with the Phase-2 upgraded CMS detector geometry using DELPHES fast simulation with average pile-up of 200 interactions and at $\sqrt{s} = 14$ TeV.

The complete list of samples used in this study is shown in Table 6.3.

6.1.2. Object selection

Objects are inherited from the DELPHES object collections which have been tuned to full-simulated phase-II reconstruction of the respective objects in CMS. Photons used in this analysis are required to have a transverse momentum (p_T) above 25 GeV with the leading photon above 35 GeV within $|\eta| < 2.5$ excluding the ECAL barrel and endcap transition region ($1.442 < |\eta| < 1.556$). The relative isolation of the photon candidate, defined as sum of the p_T of all the particles within a cone of size 0.3 around the photon and divided the sum by the photon p_T, is required to be less than 0.3 and to pass the loose identification criteria corresponding to 90% signal efficiency.

Electrons are required to have p_T above 10 GeV within $|\eta| < 2.5$ excluding the ECAL transition region and must be isolated from the photons with an angular separation in the $\eta - \phi$ plane greater than 0.4 ($\Delta R = \sqrt{\Delta\eta^2 + \Delta\phi^2} > 0.4$). The transverse momenta of the muons are required to be above 10 GeV and within $|\eta| < 2.5$, and they are required to be isolated from the photons and electrons with an angular separation greater than 0.4. Hadronically decaying taus are required to have $p_T > 20$ GeV within $|\eta| < 2.5$, and are required to be separated from photons, electrons and muons with an angular separation greater than 0.2. The relative isolation of the electrons (muons) is required to be less than 0.3 (0.1). Jets are reconstructed using the anti-k_T clustering method with a distance parameter of 0.4. They are required to have $p_T > 30$ GeV, be within $|\eta| < 5$ and to be well separated from the photon and lepton candidates with an angular separation greater than 0.4. Jets are b-tagged using a deep neural network (DNN) based secondary vertex algorithm, DEEPJET [97,98].

Dataset	Nevents	$\sigma \times BR(fb)$
GluGluToHHTo2G2Tau_node_cHHH1_TuneCP5_14TeV-powheg-pythia8_200PU	1999866	0.00104441
GluGluToHHTo2G2Qlnu_node_cHHH1_TuneCP5_14TeV-powheg-pythia8_200PU	1898894	0.0156981
GluGluToHHTo2G2l2nu_node_cHHH1_TuneCP5_14TeV-powheg-pythia8_200PU	1885835	0.0037234
VHToGG_M125_TuneCP5_14TeV-amcatnloFXFX-madspin-pythia8_200PU	1830426	5.44326
ttHJetToGG_M125_TuneCP5_14TeV-amcatnloFXFX-madspin-pythia8_200PU	5971707	1.393764
GluGluHToGG_M125_TuneCP5_14TeV-amcatnloFXFX-pythia8_200PU	444658	114.798
VBFHToGG_M125_TuneCP5_14TeV-amcatnlo-pythia8_200PU	1712900	9.51216
THQ_ctcvcp_HToGG_M125_TuneCUETP8M1_14TeV-madgraph-pythia8_200PU	789129.0	0.205428
DiPhotonJetsBox_MGG-40to80_14TeV-Sherpa_200PU	20677034.0	332804
DiPhotonJetsBox_MGG-80toInf_14TeV-Sherpa_200PU	19933297	98670
GJet_Pt-20toInf_DoubleEMEnriched_MGG-40to80_TuneCUEP8M2T4_14TeV_pythia8_200PU	19985496	3901000
GJet_Pt-40toInf_DoubleEMEnriched_MGG-80toInf_TuneCUEP8M2T4_14TeV_Pythia8_200PU	20033932	998100
GJet_Pt-20to40_DoubleEMEnriched_MGG-80toInf_TuneCP5_14TeV-pythia8_200PU	14313734	260850
TT_TuneCUETP8M2T4_14TeV-powheg-pythia8_200PU	49398942	864400
TTWJetsToLNu_TuneCUETP8M1_14TeV-amcatnloFXFX-madspin-pythia8_200PU	5040836.0	225.3
TTGamma_Dilept_TuneCUETP8M2T4_14TeV-madgraph-pythia8_200PU	2999843	623.1
TTGamma_Hadronic_TuneCUETP8M2T4_14TeV-madgraph-pythia8_200PU	2999836	799
TTGamma_SingleLeptFromT_TuneCUETP8M2T4_14TeV-madgraph-pythia8_200PU	2939839	770.9
TTGamma_SingleLeptFromTbar_TuneCUETP8M2T4_14TeV-madgraph-pythia8_200PU	2939844	769
TTGG_0Jets_TuneCUETP8M1_14TeV_amcatnlo_madspin_pythia8_200PU	1101895	18.64
DYJets_incl_MLL-50_TuneCUETP8M1_14TeV-madgraphMLM-pythia8_200PU	76952612.0	5711000
W1JetsToLNu_TuneCUETP8M1_14TeV-madgraphMLM-pythia8_200PU	77486992.0	10370000
W2JetsToLNu_TuneCUETP8M1_14TeV-madgraphMLM-pythia8_200PU	43222285.0	2965000
W3JetsToLNu_TuneCUETP8M1_14TeV-madgraphMLM-pythia8_200PU	5674591.0	1268000
WGToLNuG_PtG-40_TuneCUETP8M1_14TeV-madgraphMLM-pythia8_200PU	11776400	18790
ZGTo2LG_TuneCUETP8M1_14TeV-amcatnloFXFX-pythia8_200PU	30301987	145200
WGGJets_TuneCP5_14TeV_madgraphMLM_pythia8_200PU	1981569.0	1884
WGJJToLNu_EWK_QCD_TuneCP5_14TeV-madgraph-pythia8_200PU	1801596.0	6032
WW_TuneCUETP8M1_14TeV-pythia8_200PU	99484471.0	70440

Table 6.3. MC samples used in the analysis: signal composition listed in the first block, single H composition listed in the second block, and continuum background composition listed in the third block.

6.1.3. Event selection and categorization

All events are required to have exactly two photons whose invariant mass verifies $100 < m_{\gamma\gamma} < 180$ GeV, making this the common pre-selection to all final states. The analysis is performed in mutually exclusive final states targeting decays of the vector bosons referred to as 1L and 2L final states for $WW\gamma\gamma$ and 1 τ or 2 τs final states for $\tau\tau\gamma\gamma$. Here, lepton (L) refers to either an $e^{\pm}$ or a $\mu^{\pm}$.

6.1.3.1. One Lepton final state

Events fall into this analysis category if they contain at least one pre-selected diphoton pair, and contain exactly one electron or muon passing the selection criteria described above. This final state is expected to be the most sensitive of the three $WW\gamma\gamma$ channels due to the combination of a relatively large $W \rightarrow qq$ branching ratio, and the presence of a high energy lepton from the $W \rightarrow l\nu$ decay. The di-photon preselection as a cut flow approach already suppresses a great deal of backgrounds. However, in order to further separate the HH signal events from the expected single Higgs boson and continuum backgrounds after the SL preselections, a multi-class DNN is trained to separate the 1L process from backgrounds.

Signal enhancement: Multi-Class Deep Neural Network

Two multiclass deep neural networks (DNNs) are trained to separate the di-Higgs signal from the expected single higgs boson and continuum background. Events used to train the network and events used to evaluate the model are differentiated by choice of a random variable, the fifth decimal of the leading photon ϕ. This implies that two networks are trained on two different sets; even and odd. The DNNs are trained using the skimmed DELPHES signal and background samples and is evaluated on the even/odd events of the full DELPHES samples of the analysis to be used for categorization and background modeling to avoid any bias. The network is trained on a labelled dataset with the diHiggs (HH → 2G2Qlnu, HH → 2G2Tau, HH → 2G2l2nu) process as the *HH*, single higgs backgrounds as *H* and all the other background samples referred as the continuum background.

During the training, events in the signal MC are given a target value of 1 and events in the background MC are given a target value of 0. Due to the class imbalance in the dataset, events are re-weighted such that the learning weight in both classes is the same by normalizing the event weight where what is called event weight is the gen weight that is scaled to expected cross-section. This ensures the network focuses on categorising all classes with equal importance.The network hyper-parameter settings for the trained semi-leptonic channel DNN are as following: categorical_crossentropy as the loss function, Adam optimizer, ReLU and sigmoid hidden and output layer activation functions respectively. Rest of the hyperparameters can be found in 2.1. The full list of variables used as an input to the DNN can be found in Table 2.2. Some of the input variables' distributions are shown in Figure 6.3.

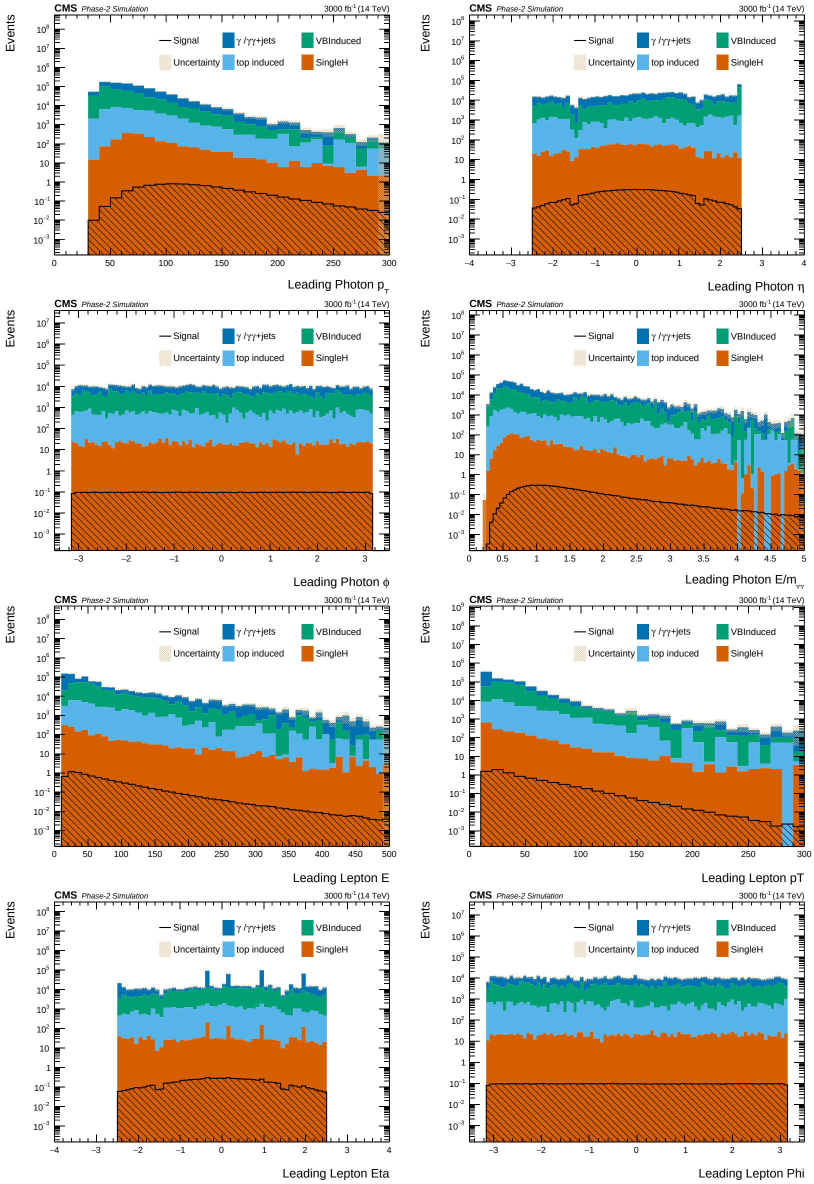

Figure 6.3. | The DNN input distributions of the leading photon and lepton kinematics after applying the One Lepton final state requirements.

The DNN output score distribution is shown in Figure 6.4. One-Lepton final state is further categorized in four categories making use of the DNN score.The categories are shown in Table 6.4. These categories are chosen in order to make use of all available signal events over the backgrounds. The boundaries that are currently imposed are a choice of experience which proved to be optimal. A test has been performed to play around the boundaries to extract the most sensitive significance. The small study showed that the categorization shown in 6.4 is already yielding the highest significance.

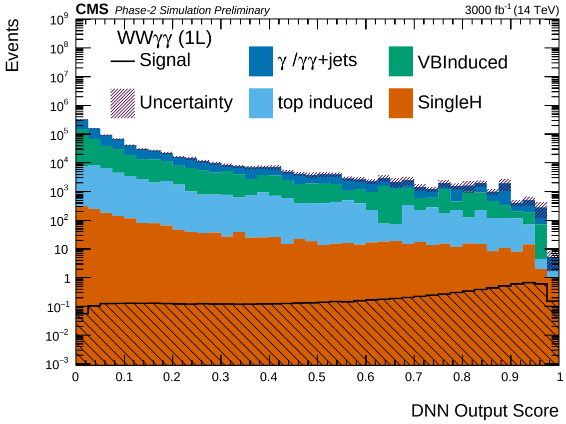

Figure 6.4. | DNN output score distribution for the 1L final state after the model is evaluated on the full samples of the analysis.

Categories	Definition
Category 1 (hasDNNScore)	$0.1 <$ DNN score < 0.6
Category 2 (hasDNNScore2)	$0.6 <$ DNN score < 0.8
Category 3 (hasDNNScore3)	$0.8 <$ DNN score < 0.92
Category 4 (hasDNNScore4)	DNN score > 0.92

Table 6.4. | One Lepton final state DNN score categories

6.1.3.2. Two Lepton final state

A cut-based analysis is performed here. In this final state, events are required to have at least two oppositely charged leptons (e^+e^-, $\mu^+\mu^-$, $e^\pm\mu^\mp$) passing the electron and muon object selections described in Section 6.1.2. Furthermore, the events are required to satisfy the selections listed in Table 6.5, where $\Delta R(l,l)$ is the ΔR between two leptons, m_{ll} is the mass of dilepton system and $m_{e\gamma}$ is the invariant mass of the leading electron and the leading photon in the events that have at least one electron.

Variable	Selection
$\Delta R(l,l)$	> 0.4
p_{T} of leading lepton	$> 20 GeV$
p_{T} of subleading lepton	$> 10 GeV$
E_T^{miss}	$> 20 GeV$
$p_T^{\gamma\gamma}$	$> 91 GeV$
m_{ll}	$< 80 GeV or > 100 GeV$
number of medium-tagged b-jets	$= 0$
$\lvert m_{e\gamma} - m_z \rvert$	$> 5 GeV$

Table 6.5. | Selection criteria of the Two Lepton final state.

6.1.3.3. One Tau lepton final state

Events fall in this category if they contain two photons within the required invariant mass range and contain exactly one hadronically decaying tau lepton and no electron/muon. Here also, two multiclass deep neural networks (DNNs) are trained following the same strategy as in the one lepton final state. In this final state, tau's kinematic variables are replacing the ones of the electron or the muon. Table 2.3 shows the list of input feautures used to train the multi-class DNN. See Figure 6.5 for the output score distribution for this final state.

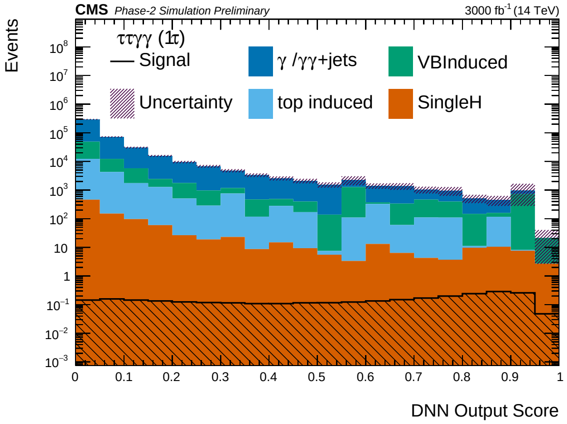

Figure 6.5. | DNN output score distribution for the 1τ final state after the model is evaluated on the full samples of the analysis.

Here, events are partitioned in two categories making use of the DNN score in an effort to maximize the signal purity. Category one corresponds to events where the DNN score lies between 0.1 and 0.65, while events with a DNN score higher than 0.65 are categorized in Category 2.

6.1.3.4. Two Tau leptons final state

A cut-based analysis is performed in this final state. The events end up in this category if they have at least two taus and no lepton. In addition, a Z-veto is applied such that the events with invariant mass of the two leptons in the 80 - 100 GeV interval are rejected. The two taus are required to be oppositely charged. In case of multiple tau lepton pair candidates, the pair having the invariant mass closest to the Higgs mass is chosen.

6.1.4. Signal extraction

Given the presence of high fluctuations in the $m_{\gamma\gamma}$ distribution for the continuum background across different categories, the shape fitted with an exponential function has been used to describe the continuum background. The correlations among different sources of uncertainties are taken into account while the different final states are considered as independent channels in the fit.

The expected Phase-2 $m_{\gamma\gamma}$ distributions are shown in Figure 6.6, 6.7 for all final states and their corresponding categories, where signal along with the single Higgs and continuum background is described using a Gaussian and an exponential function. The (pseudo-)data are generated according to the fitted signal, single Higgs and continuum background contributions. The distributions shown above in Figure 6.6, 6.7 are used for signal extraction as explained in Section 6.1.6.

6.1.5. Systematic uncertainties

The systematic uncertainties detailed below are taken into account in the statistical model via profiling of nuisance parameters according to a frequentist approach. These are expected to be small compared to the statistical uncertainty in this analysis. The following sources are considered as theoretical systematic uncertainties:

- **Theoretical uncertainties on the HH cross section:** The combined uncertainty on the QCD scale and on the top quark mass is taken into account. The combined uncertainty on the PDF modeling is considered.
- **Theoretical uncertainties on the single Higgs cross sections:** Process-dependent uncer- tainties related to the QCD scale, the PDF modeling, and the strong coupling constant are taken into account for the ggH, VBFH, VH, ttH and tHq processes.

The theoretical uncertainties are added on the ggHH signal and single Higgs

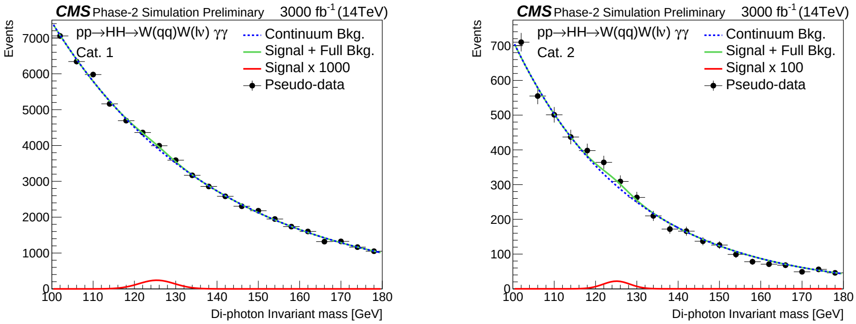

(a) One lepton final state, Category 1 **(b)** One lepton final state, Category 2

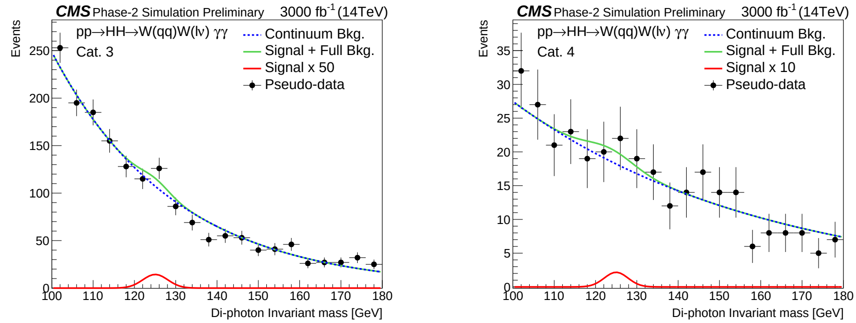

(c) One lepton final state, Category 3 **(d)** One lepton final state, Category 4

Figure 6.6. | $m_{\gamma\gamma}$ distributions in the $WW\gamma\gamma$, 1L final state and its four categories.

boson processes as described in Table 6.6.

Process	Uncertainty Source		
	PDF $+\alpha_s$ (%)	QCD Scale (%)	m_{top} (%)
ggHH	± 3	+2.1/-4.9	+4.0/-18
ggH	+4.6/-6.7	± 3.2	-
VBFH	+0.5/-0.3	± 2.1	-
VH	+0.4/-0.7	± 1.8	-
ttH	+6/-9.2	± 3.5	-
tHq	+6.4/-14.7	± 3.6	-

Table 6.6. | Theoretical uncertainties considered on the ggHH signal and single Higgs processes.

The experimental uncertainties have been added as listed in Table 6.7. These uncertainties have been applied according to the Yellow Report recommendation described in Ref. [99].

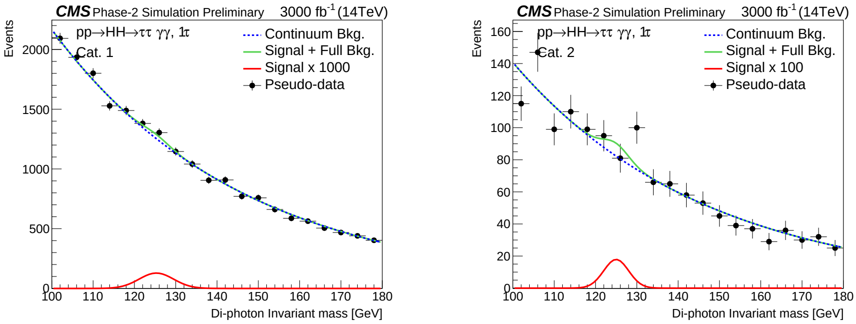

(a) One tau final state, Category 1

(b) One tau final state, Category 2

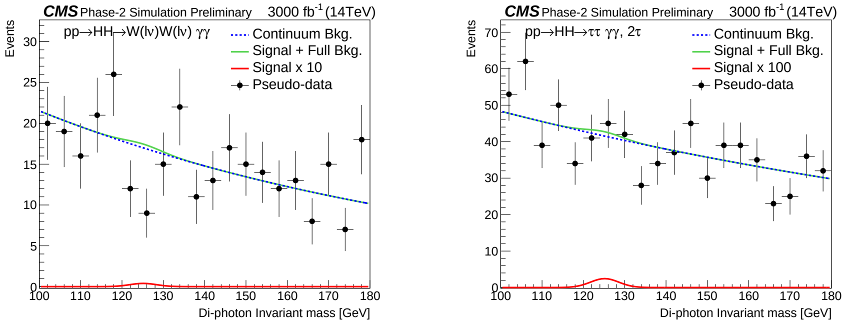

(c) Two lepton final state

(d) Two taus final state

Figure 6.7. | $m_{\gamma\gamma}$ distributions in the $\tau\tau\gamma\gamma$, 1τ and its two categories (top row) and $WW\gamma\gamma$, 2L (bottom left), $\tau\tau\gamma\gamma$ 2 τs (bottom right).

Uncertainty Source	Input (%)
Luminosity	1
Diphoton trigger	2
$m_{\gamma\gamma}$ resolution	5
PhotonID	0.5/photon
electronID	0.5/electron
muonID	0.5/muon
tauID	2.5/tau
Tau energy scale	3
Jet energy Scale	3
b-tagging veto	3

Table 6.7. | Experimental uncertainties considered in this study.

6.1.6. Results

The expected significance is extracted by fitting the $m_{\gamma\gamma}$ distributions (from Figure 6.6 and 6.7) in all the categories using a binned maximum likelihood approach with all systematic uncertainties treated as nuisance parameters with log-normal distributions using the Higgs Combine tool [100].

The significance values obtained are shown in Table 6.8, 6.9, and 6.10 for the WW$\gamma\gamma$ and $\tau\tau\gamma\gamma$ final states along with their combination.

Table 6.8. | Expected HL-LHC significances (σ) of the WW$\gamma\gamma$ categories and their combination.

Categories	Significance (stat+exp+theory)
Category 1	0.0183
Category 2	0.0846
Category 3	0.0982
Category 4	0.1629
One Lepton	0.2038
Two Lepton	0.0294
Combination	**0.2056**

Table 6.9. | Expected HL-LHC significances (σ) of $\tau\tau\gamma\gamma$ categories with their combination.

Categories	Significance (stat+exp+theory)
Category 1	0.0143
Category 2	0.0768
One Tau	0.0782
Two Taus	0.0129
Combination	**0.0792**

Table 6.10. | Expected HL-LHC significances (σ) of the WW$\gamma\gamma$ and $\tau\tau\gamma\gamma$ channels with their combination.

Final State	Significance (stat+exp+theory)
$WW\gamma\gamma$	0.21
$\tau\tau\gamma\gamma$	0.08
Combination	**0.22**

6.2. Personal Contributions

The analysis documented in this chapter was conducted in collaboration with UCLouvain[1], ITU[2], and NU[3].

The analysis inherited the strategy from the corresponding Run-2 analysis where the collaboration with NU emerges as the contact person of the Run-2 analysis was affiliated to NU. The third collaborator joined to provide extra person power for the extension of the analysis to as much final states as we could. Eventually, the extension could reach only one more final state, $\tau\tau\gamma\gamma$, although the initial plan was to include $ZZ\gamma\gamma$ as well.

I was the contact person of the analysis therefore I have contributions at every step of the project from sample production to result extraction. However, the tasks I was responsible for were sample production and gridpack preparation; setting up of the analysis framework and adaptation of the analysis strategy and workflow; performing checks on the selection efficiencies in comparison to Run-2 numbers and validation of these efficiencies; development and training of the DNNs used in the analysis and their implementation in the analysis framework; the writing of the analysis documentation; performing the statistical analysis with Combine tool; and presenting the approval talk on behalf of the team. I also presented the work in one local and two international conferences; Belgium Summer Solstice 2022, ICHEP 2022 and Higgs Hunting 2022, respectively.

6.3. Discussion and Outlook

In this data analysis focused on Higgs pair production at HL-LHC in the decay channels $WW\gamma\gamma$ and $\tau\tau\gamma\gamma$, the obtained significance of the process was determined to be 0.22 sigma where this significance value indicates the level of statistical evidence for the presence of the process. This is the first study conducted on these two decay channels at HL-LHC. The measurement of Higgs self-coupling is a crucial aspect in understanding the behavior of the Higgs boson and confirming the predictions of the Standard Model of particle physics. By investigating the $WW\gamma\gamma$ and $\tau\tau\gamma\gamma$ decay channels, the aim is to probe the interaction between two Higgs bosons, providing insights into the self-interaction strength. While the obtained significance of 0.22 sigma suggests some evidence for the presence of the process, it is important to note that this level of significance is relatively low, indicating that more data or improved analysis techniques may be necessary to establish a robust measurement of the Higgs self-coupling through these two decay channels.

As mentioned earlier in this chapter, the fully hadronic decay of the WW was

---

[1] Université catholique de Louvain, Belgium

[2] Istanbul Technical University, Turkey

[3] Northeastern University, USA

not considered because of the lack of quality QCD samples. Including the fully hadronic decay channel of $WW\gamma\gamma$ in the analysis would add another important final state to the study. The fully hadronic final state, characterized by the decay of both W bosons into quarks, presents unique challenges and opportunities associated with jet reconstruction, background estimation, and mitigating the effects of pile-up. These challenges arise due to the complex nature of hadronic decays, which involve a larger number of particles in the final state. Careful optimization of analysis techniques, event selection criteria, and background modeling would be necessary to effectively analyze the fully hadronic channel.

The contributions of the $WW\gamma\gamma$ and $\tau\tau\gamma\gamma$ decay channels to HH studies are significant but should be considered in the context of other channels as well. Channels such as bb$\gamma\gamma$, bb$\tau\tau$, and four b-quark final states contribute significantly to HH studies, albeit through different aspects. Each channel offers unique sensitivity to specific couplings, cross-sections, or decay modes. Combining information from multiple channels allows for a more comprehensive understanding of HH production and can provide stronger constraints on theoretical models. As for $WW\gamma\gamma$ and $\tau\tau\gamma\gamma$, $\tau\tau\gamma\gamma$ channel is particularly sensitive to the Higgs self-coupling, making it crucial for directly probing the self-interactions of the Higgs boson. This channel provides unique information about the Higgs boson's properties and can help identify potential deviations from the predictions of the Standard Model. Therefore, in terms of studying the Higgs self-coupling, the $\tau\tau\gamma\gamma$ channel plays a significant role. The $WW\gamma\gamma$ channel, while not as sensitive to the Higgs self-coupling as the $\tau\tau\gamma\gamma$ channel, can still contribute significantly to HH studies due to its relatively cleaner signature and good signal-to-background ratio. In summary, while the WW gamma gamma and tau tau gamma gamma decay channels have their unique strengths and contributions to HH studies, it is important to consider the overall combination of channels to achieve a comprehensive understanding of HH production. Each channel brings valuable information and contributes to different aspects of the analysis, such as sensitivity to self-couplings, cross-section measurements, and exploration of new physics phenomena.

Further studies and refinements in experimental techniques, data collection, and analysis methods are essential to enhance the statistical significance of the observed process and improve the precision of the measurement of Higgs self-coupling. These efforts will contribute to our understanding of the fundamental properties of the Higgs boson and potentially shed light on physics beyond the Standard Model.

Conclusion

With Higgs having been discovered, a whole new (scalar) sector to be explored was unlocked as well as the need to improve the machine that made the discovery possible -the LHC. The works reported on this document are heavily invested in these two frontiers. Namely, the Phase 2 Upgrade of the CMS detector designed to make the detector compatible with HL-LHC conditions, and a prospective analysis searching for Higgs pair production in this future scenario with the upgraded detector.

A review of the theory, followed by the experimental apparatus and its upgrade design are provided in the first four chapters. In chapter 5, the upgrade efforts in different aspects are described. First, the infrastructure and the clean-room where the upgrade studies are conducted are illustrated. The services design of the new detector is discussed at length by presenting the methodology of the design, its analysis, and the its validation. The cabling design of the 16 dees of one full endcap have been completed, studied on a dedicated mock-up, and majority of its design considerations are justified. This work is still ongoing at the time of writing. Second, the efforts put on the realization of quality assurance procedures are summarized. To ensure a quality integration, two major test setups are realized: a module burn-in setup to test the functionality of the modules at the experimental conditions before integrating them on their respective dee, and, a sector test to repeat the functionality test while the modules are integrated. The module burn-in setup is completed and first results are discussed. The sector test is completed in terms procedure outline, however, the setup hardware is being finalized on a prototype at the time of writing. Finally, the assembly of one full endcap (TEDD) is described with details on the tooling and workload distribution among the project collaborators.

The final chapter of this document reports on the prospective Higgs pair analysis that was conducted within a campaign that aims at justifying the upgrade needs on our current accelerators and detectors (SNOWMASS). The analysis approach, the samples used, the strategy followed, as well as the findings are presented. Following up from its previous counterpart (the Yellow Report 2018), these analyses improved on the significances reported back in 2018. The analysis of focus for this document provided the first significance on the likelihood of observing HH in the final states of WW$\gamma\gamma$ and $\tau\tau\gamma\gamma$ at the center of mass energy of 14 TeV. Once combined with other analyses within and outside CMS, there is a strong indication that the symbolic threshold of 5σ

significance is within reach. In that regard, the importance and the necessity of the HL-LHC upgrade is highlighted and justified.

The author of this document has started their scientific career within yet another upgrade project and has contributed to two major upgrades of the CMS detector so far. Considering the fact that our field has entered a period of precision studies in pursuit of finding new physics by scrutinizing the interactions of the known particles, the upgrade of the experimental apparatus poses quite an importance. In this context, the upgrade studies such as the one reported in this document provide valuable insights and guidance to the ultimate goal of perfecting our understanding of the world around us.

A. Appendix

Additional Material on the TEDD

The convention adopted for module numbering follows that of CMSSW. They can be designated either by their detid, which is unique in the whole tracker, or by their position on the dee, as `<ring idx>-<phi idx>`.

Table 1.1. Description of the fields in the TEDD detid (from CMSSW)

Field name	Start bit	Hex mask	Number of bits	Comment
Detector	28	0xF	4	Tracker = 1
Subdetector	25	0x7	3	TEDD = 2
Side	23	0x3	2	TEDD- = 1, TEDD+ = 2
Unused	22	0x1	1	always 0
Double Disk	18	0xF	4	increasing abs(z)
Ring	12	0x3F	6	increasing r
Unused	10	0x3	2	always 1
Phi	2	0xFF	8	increasing phi
Sensor	0	0x3	2	always 0 for modules

Figure 1.1 shows a visualization of the optical tPP1.

Tables 1.2, 1.3 show the different types of naked fanouts used in the TEDD. The columns labelled “Lf” indicate the lengths of each individual branch (up to five per fanout, depending on the type). The total length (“L”) corresponds to length of the longest branch, plus the length of the common trunk at the PP0 side. The number of variants can be reduced to 22 if we accept to use variants with more branches than needed and to cut unused fibers close to the PP0.

Table **??** shows all variants of rugged fanouts.

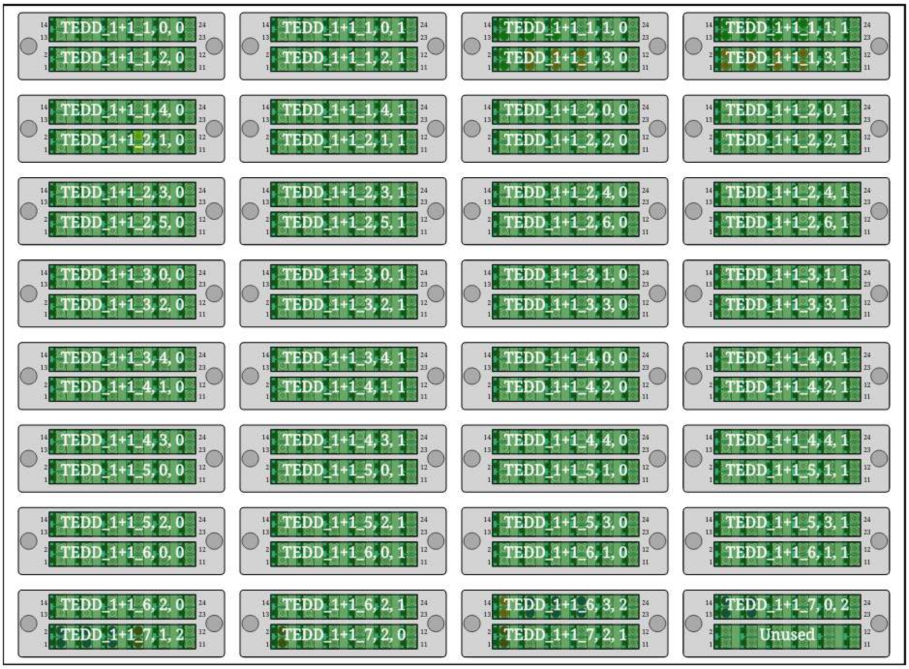

Figure 1.1. | Visualization of the optical tPP1 for sector tests, showing the MPO-to-LC adapter cassettes. The labels indicate which optical sectors correspond to which cassettes, for an exemplary sector test of a TEDD1+ odd top dee.

Table 1.2. | The 57 different types of naked fanouts used in the TEDD.

Item	Nb of connectors	Lf (cm)	Lf (cm)	Lf (cm)	Lf (cm)	Lf (cm)	L (cm)	Quantity
0	1	190	0	0	0	0	200	12
1	1	160	0	0	0	0	170	26
2	1	130	0	0	0	0	140	84
3	1	100	0	0	0	0	110	94
4	2	220	220	0	0	0	230	4
5	2	220	190	0	0	0	230	4
6	2	190	190	0	0	0	200	20
7	2	190	160	0	0	0	200	62
8	2	160	160	0	0	0	170	66
9	2	160	130	0	0	0	170	86
10	2	130	130	0	0	0	140	176
11	2	130	100	0	0	0	140	176
12	2	130	70	0	0	0	140	36
13	2	100	100	0	0	0	110	230
14	2	100	70	0	0	0	110	64
15	2	70	70	0	0	0	80	56
16	3	220	190	190	0	0	230	4
17	3	190	190	190	0	0	200	8
18	3	190	190	160	0	0	200	8
19	3	190	160	160	0	0	200	30
20	3	190	160	130	0	0	200	6
21	3	160	160	160	0	0	170	42
22	3	160	160	130	0	0	170	12
23	3	160	130	130	0	0	170	36
24	3	130	130	130	0	0	140	64
25	3	130	130	100	0	0	140	76
26	3	130	100	100	0	0	140	86
27	3	130	100	70	0	0	140	36

Table 1.3. | The 57 different types of naked fanouts used in the TEDD.

Item	Nb of connectors	Lf (cm)	Lf (cm)	Lf (cm)	Lf (cm)	Lf (cm)	L (cm)	Quantity
28	3	130	70	70	0	0	140	48
29	3	100	100	100	0	0	110	86
30	3	100	100	70	0	0	110	72
31	3	100	70	70	0	0	110	98
32	3	70	70	70	0	0	80	4
33	4	220	220	190	190	0	230	6
34	4	190	190	190	190	0	200	16
35	4	190	190	160	160	0	200	6
36	4	190	160	160	160	0	200	20
37	4	190	160	160	130	0	200	14
38	4	160	160	160	160	0	170	4
39	4	160	160	160	130	0	170	16
40	4	160	160	130	130	0	170	18
41	4	160	130	130	130	0	170	8
42	4	160	130	130	100	0	170	14
43	4	130	130	130	130	0	140	12
44	4	130	130	130	100	0	140	22
45	4	130	130	100	100	0	140	28
46	4	130	100	100	100	0	140	10
47	4	130	100	100	70	0	140	46
48	4	130	100	70	70	0	140	28
49	4	130	70	70	70	0	140	6
50	4	100	100	100	100	0	110	6
51	4	100	100	100	70	0	110	18
52	4	100	100	70	70	0	110	58
53	4	100	70	70	70	0	110	10
54	4	70	70	70	70	0	80	6
55	5	130	130	130	100	100	140	6
56	5	100	100	70	70	70	110	14

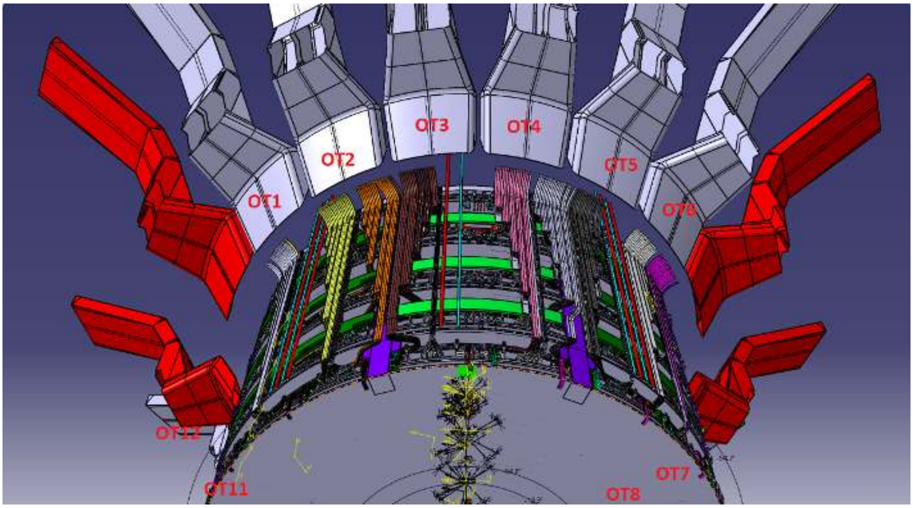

Figure 1.2. | 3D model of the TEDD and the tracker bulkhead showing the service channels.

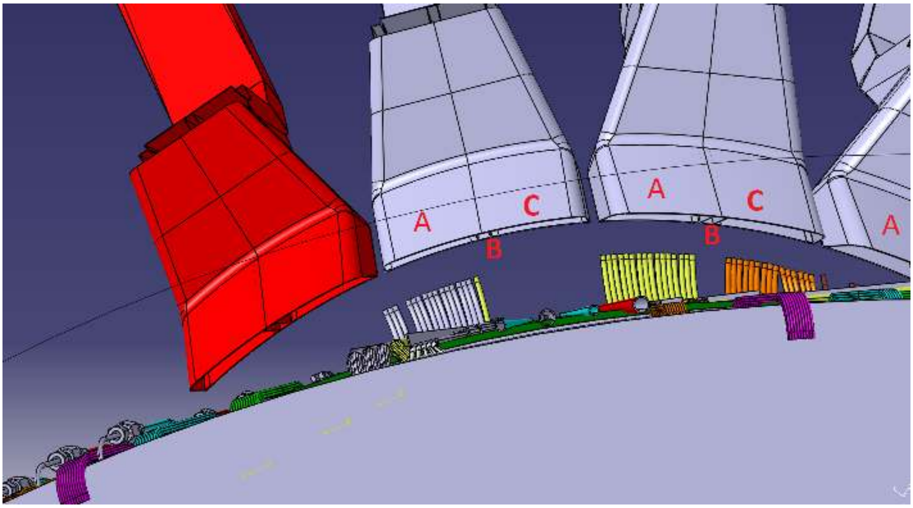

Figure 1.3. | 3D model of the TEDD and the tracker bulkhead showing the service channels, highlighting channels A, B, and C.

B. Appendix

Additional Material on the HH analysis

The two photons invariant mass distributions for the one-leptonic and one tau final states, inclusive of all categories are shown.

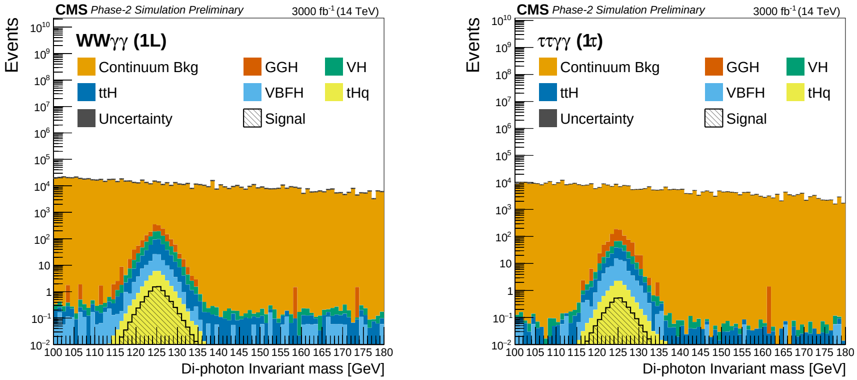

(a) One lepton final state

(b) One tau final state

Figure 2.1. $m_{\gamma\gamma}$ distributions in the $WW\gamma\gamma$, 1L (left) and $\tau\tau\gamma\gamma$, 1τ (right) final states.

The DNN input variables' distributions for the One Lepton final state are shown in Figure 2.2.

Hyperparameter settings for the One Lepton final state DNN can be found in Table 2.1.

The variables used as an input to the One Lepton final state DNN can be found in Table 2.2.

The variables used as an input to the One Tau final state DNN can be found in Table 2.2.

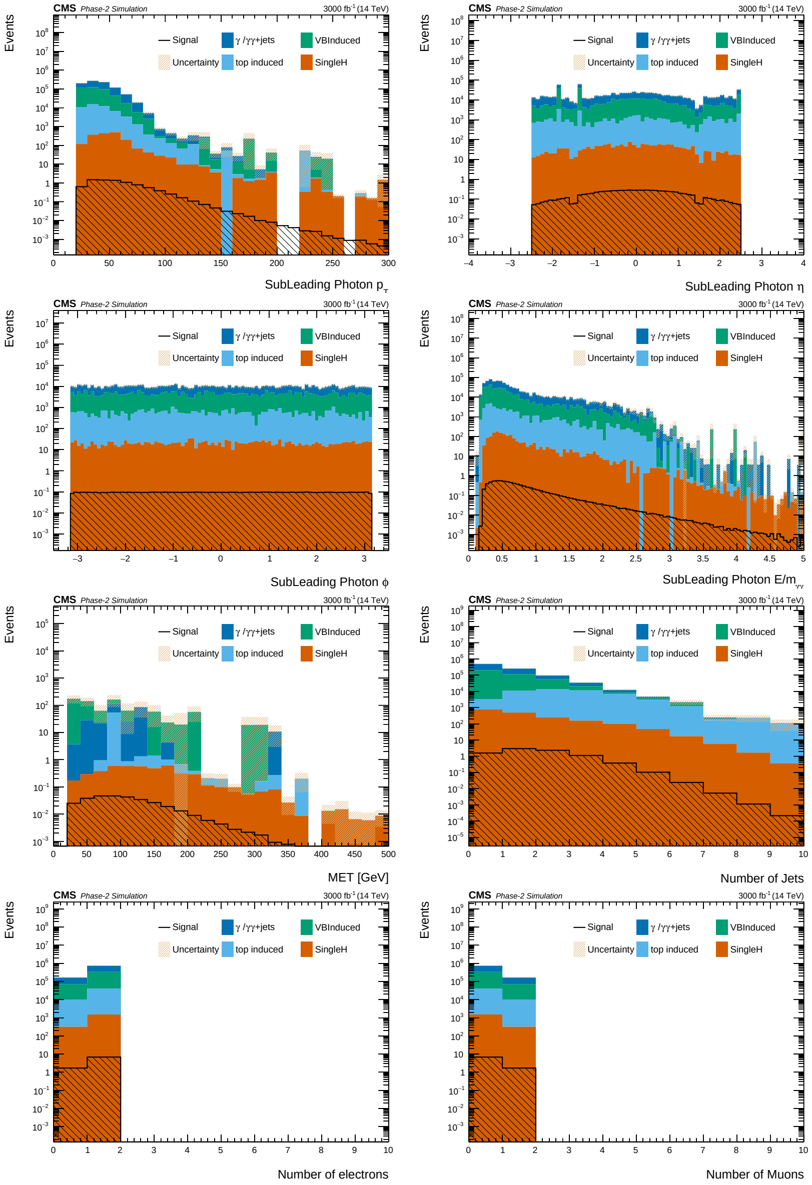

Figure 2.2. sub-leading photon kinematics after applying the One Lepton final state requirements.

Hyper-parameter	Setting
Epochs	200
Batch size	256
Learning rate	0.001
Optimiser	Adam
Loss function	categorical_crossentropy
Hidden layer activation functions	ReLU
Output layer activation function	sigmoid

Table 2.1. Hyper-parameter settings for 1L channel DNN.

Feature	Description
Leading Photon p_T / $m_{\gamma\gamma}$	Transverse momentum of the photon with the highest transverse momentum out of the selected photons, scaled to diphoton mass.
Leading Photon η	Pseudorapidity of the photon with the highest transverse momentum out of the selected photons
Leading Photon ϕ	Direction in the transverse plane of the photon with the highest transverse momentum out of the selected photons
Leading Photon E / $m_{\gamma\gamma}$	Energy of the photon with the highest transverse momentum out of the selected photons, scaled to diphoton mass.
Subleading Photon p_T / $m_{\gamma\gamma}$	Transverse momentum of the photon with the second highest transverse momentum out of the selected photons, scaled to diphoton mass.
Subleading Photon η	Pseudorapidity of the photon with the second highest transverse momentum out of the selected photons
Subleading Photon ϕ	Direction in the transverse plane of the photon with the second highest transverse momentum out of the selected photons
Subleading Photon E / $m_{\gamma\gamma}$	Energy of the photon with the second highest transverse momentum out of the selected photons, scaled to diphoton mass.
Jet Multiplicity	Number of selected jets in the event (flavour inclusive)
Leading Jet p_T	Transverse momentum of the jet with the highest transverse momentum out of the selected jets
Leading Jet η	Pseudorapidity of the jet with the highest transverse momentum out of the selected jets
Leading Jet ϕ	Direction in the transverse plane of the jet with the highest transverse momentum out of the selected jets
Leading Jet E	Energy of the jet with the highest transverse momentum out of the selected jets
Subleading Jet p_T	Transverse momentum of the jet with the second highest transverse momentum out of the selected jets
Subleading Jet η	Pseudorapidity of the jet with the second highest transverse momentum out of the selected jets
Subleading Jet ϕ	Direction in the transverse plane of the jet with the second highest transverse momentum out of the selected jets
Subleading Jet E	Energy of the jet with the second highest transverse momentum out of the selected jets
Electron p_T	Transverse momentum of the selected electron
Electron η	Pseudorapidity of the selected electron
Electron ϕ	Direction in the transverse plane of the selected electron
Electron E	Energy of the selected electron
Muon p_T	Transverse momentum of the selected Muon
Muon η	Pseudorapidity of the selected Muon
Muon ϕ	Direction in the transverse plane of the selected Muon
Muon E	Energy of the selected lepton
MET	The missing transverse energy
m_{j_0,j_1}	The invariant mass of the leading and subleading jets

Table 2.2. Input features used to train semi-leptonic channel DNN.

Feature	Description
Leading Photon p_T / $m_{\gamma\gamma}$	Transverse momentum of the photon with the highest transverse momentum out of the selected photons, scaled to diphoton mass.
Leading Photon η	Pseudorapidity of the photon with the highest transverse momentum out of the selected photons
Leading Photon ϕ	Direction in the transverse plane of the photon with the highest transverse momentum out of the selected photons
Leading Photon E / $m_{\gamma\gamma}$	Energy of the photon with the highest transverse momentum out of the selected photons, scaled to diphoton mass.
Subleading Photon p_T / $m_{\gamma\gamma}$	Transverse momentum of the photon with the second highest transverse momentum out of the selected photons, scaled to diphoton mass.
Subleading Photon η	Pseudorapidity of the photon with the second highest transverse momentum out of the selected photons
Subleading Photon ϕ	Direction in the transverse plane of the photon with the second highest transverse momentum out of the selected photons
Subleading Photon E / $m_{\gamma\gamma}$	Energy of the photon with the second highest transverse momentum out of the selected photons, scaled to diphoton mass.
Jet Multiplicity	Number of selected jets in the event (flavour inclusive)
Leading Jet p_T	Transverse momentum of the jet with the highest transverse momentum out of the selected jets
Leading Jet η	Pseudorapidity of the jet with the highest transverse momentum out of the selected jets
Subleading Jet p_T	Transverse momentum of the jet with the second highest transverse momentum out of the selected jets
Subleading Jet η	Pseudorapidity of the jet with the second highest transverse momentum out of the selected jets
Leading Tau p_T	Transverse momentum of the selected tau
Leading Tau η	Pseudorapidity of the selected tau
Leading Tau ϕ	Direction in the transverse plane of the selected tau
Leading Tau E	Energy of the selected tau
MET	The missing transverse energy

Table 2.3. | Input features used to train one-tau channel DNN.

References

[1] D. H. Perkins, “"Introduction to High Energy Physics"”. Cambridge University Press, 3rd edition, `https://cds.cern.ch/record/396126`.

[2] R. Mann, “An Introduction to Particle Physics and the Standard Model”. CRC Press,

[3] T. Plehn, “Lectures on LHC Physics”, volume 844.

[4] Particle Data Group Collaboration, “Review of Particle Physics”, *Phys. Rev. D* **98** (Aug, 2018) 030001. `doi:10.1103/PhysRevD.98.030001`.

[5] R. Leone, “On the wonderfulness of Noether’s theorems, 100 years later, and Routh reduction”, 2018. `arXiv:1804.01714`.

[6] F. Englert et al., “Broken Symmetry and the Mass of Gauge Vector Mesons”, *Phys. Rev. Lett.* **13** (Aug, 1964) 321–323. `doi:10.1103/PhysRevLett.13.321`.

[7] P. W. Higgs, “Broken symmetries, massless particles and gauge fields”, *Phys. Lett.* **12** (1964) 132–133. `doi:10.1016/0031-9163(64)91136-9`.

[8] P. W. Higgs, “Broken Symmetries and the Masses of Gauge Bosons”, *Phys. Rev. Lett.* **13** (Oct, 1964) 508–509. `doi:10.1103/PhysRevLett.13.508`.

[9] ATLAS & CMS Collaboration, “Combined Measurement of the Higgs Boson Mass in pp Collisions at $\sqrt{s} = 7$ and 8 TeV with the ATLAS and CMS Experiments”,. `arXiv:1503.07589`.

[10] CMS Collaboration, “Combined measurements of Higgs boson couplings in proton-proton collisions at $\sqrt{s}$ = 13 TeV”, *arXiv e-prints* (September, 2018) arXiv:1809.10733. `arXiv:1809.10733`.

[11] B. Di Micco et al., “Higgs boson potential at colliders: status and perspectives”, *arXiv e-prints* (September, 2019). `arXiv:1910.00012`.

[12] L. Evans et al., “LHC Machine”, *Journal of Instrumentation* **3** (aug, 2008) S08001. `doi:10.1088/1748-0221/3/08/S08001`.

[13] O. S. Brüning et al., “LHC Design Report”. CERN Yellow Reports: Monographs. CERN, Geneva, `http://cds.cern.ch/record/782076`.

[14] LHC Study Group CollaborationT. S. Pettersson, et al., eds., “The Large Hadron Collider: Conceptual design”. 10, 1995.

[15] CMS Collaboration, “CMS Physics Technical Design Report, Vol. I: Detector Per- formance and Software,”, technical report, 2006. `https://cds.cern.ch/record/922757/`.

[16] E. Mobs, "The CERN accelerator complex. Complexe des accélérateurs du CERN", Jul, 2016. `https://cds.cern.ch/record/2197559`. General Photo.

[17] P. Grafström et al., "Luminosity determination at proton colliders", *Progress in Particle and Nuclear Physics* **81** (2015) 97–148. `doi:https://doi.org/10.1016/j.ppnp.2014.11.002`.

[18] CMS Collaboration, "CMS Luminosity - Public results". `https://twiki.cern.ch/twiki/bin/view/CMSPublic/LumiPublicResults`, 2022.

[19] CMS Collaboration, "Pileup mitigation at CMS in 13 TeV data", *Journal of Instrumentation* **15** (September, 2020) P09018. `doi:10.1088/1748-0221/15/09/P09018`, `arXiv:2003.00503`.

[20] CMS Collaboration, "The CMS Experiment at the CERN LHC", *JINST* **3** (2008) S08004. `doi:10.1088/1748-0221/3/08/S08004`.

[21] CMS Collaboration, "The Phase-2 Upgrade of the CMS Tracker", technical report, Jun, 2017. `https://cds.cern.ch/record/2272264`.

[22] CMS Collaboration, "Performance of the CMS Hadron Calorimeter with Cosmic Ray Muons and LHC Beam Data", *Journal of Instrumentation* **05** (2010). `doi:10.1088/1748-0221/5/03/T03012`.

[23] CMS Collaboration, "Performance of the CMS muon detector and muon reconstruction with proton-proton collisions at $\sqrt{s} = 13$ TeV", *JINST* **13** (Apr, 2018) P06015. 53 p. `doi:10.1088/1748-0221/13/06/P06015`, `arXiv:1804.04528`.

[24] CMS Collaboration, "CMS Technical Design Report for the Level-1 Trigger Upgrade", technical report, Jun, 2013. `https://cds.cern.ch/record/1556311`. Additional contacts: Jeffrey Spalding, Fermilab, Jeffrey.Spalding@cern.ch Didier Contardo, Universite Claude Bernard-Lyon I, didier.claude.contardo@cern.ch.

[25] CMS Collaboration, "The Phase-2 Upgrade of the CMS DAQ Interim Technical Design Report", technical report, Sep, 2017. `https://cds.cern.ch/record/2283193`.

[26] CMS Collaboration, "Particle-flow reconstruction and global event description with the CMS detector", *Journal of Instrumentation* **12** (oct, 2017) P10003–P10003. `doi:10.1088/1748-0221/12/10/p10003`.

[27] CMS Collaboration, "Commissioning and performance of the CMS silicon strip tracker with cosmic ray muons", *Journal of Instrumentation* **5** (mar, 2010). `doi:10.1088/1748-0221/5/03/t03008`.

[28] T. Speer et al., "Track reconstruction in the CMS tracker", *Nuclear Instruments and Methods in Physics Research Section A: Accelerators, Spectrometers, Detectors and Associated Equipment* **559** (04, 2006) 143–147. `doi:10.1016/j.nima.2005.11.207`.

[29] R. E. Kalman, "A New Approach to Linear Filtering and Prediction Problems", *Journal of Basic Engineering* **82** (03, 1960) 35–45. `doi:10.1115/1.3662552`.

[30] W. Adam et al., "Reconstruction of electrons with the Gaussian-sum filter in the CMS tracker at the LHC", *Journal of Physics G: Nuclear and Particle Physics* **31** (jul, 2005) N9–N20. `doi:10.1088/0954-3899/31/9/n01`.

[31] CMS Collaboration, "Description and performance of track and primary-vertex reconstruction with the CMS tracker", *JINST* **9** (2014), no. 10, P10009. `doi:10.1088/1748-0221/9/10/P10009`, `arXiv:1405.6569`.

[32] CMS Collaboration, "Muon Reconstruction and Identification Performance with Run-2 data", 2020. `https://cds.cern.ch/record/2727091`.

[33] CMS Collaboration, "Performance of electron and photon reconstruction in Run 2 with the CMS experiment",.

[34] M. Cacciari et al., "The anti-ik/isubit/i /subjet clustering algorithm", *Journal of High Energy Physics* **2008** (apr, 2008) 063–063. `doi:10.1088/1126-6708/2008/04/063`.

[35] CMS Collaboration, "Identification of heavy-flavour jets with the CMS detector in pp collisions at 13 TeV", *JINST* **13** (2018), no. 05, P05011. `doi:10.1088/1748-0221/13/05/P05011`, `arXiv:1712.07158`.

[36] E. Bols et al., "Jet flavour classification using DeepJet", *Journal of Instrumentation* **15** (dec, 2020) P12012. `doi:10.1088/1748-0221/15/12/P12012`.

[37] J. Alwall et al., "The automated computation of tree-level and next-to-leading order differential cross sections, and their matching to parton shower simulations", *Journal of High Energy Physics* **2014** (jul, 2014). `doi:10.1007/jhep07(2014)079`.

[38] P. Nason, "A New method for combining NLO QCD with shower Monte Carlo algorithms", *JHEP* **11** (2004) 040. `doi:10.1088/1126-6708/2004/11/040`, `arXiv:hep-ph/0409146`.

[39] S. Frixione et al., "Matching NLO QCD computations with Parton Shower simulations: the POWHEG method", *JHEP* **11** (2007) 070. `doi:10.1088/1126-6708/2007/11/070`, `arXiv:0709.2092`.

[40] S. Alioli et al., "A general framework for implementing NLO calculations in shower Monte Carlo programs: the POWHEG BOX", *JHEP* **06** (2010) 043. `doi:10.1007/JHEP06(2010)043`, `arXiv:1002.2581`.

[41] T. Sjöstrand et al., "An introduction to PYTHIA 8.2", *Computer Physics Communications* **191** (June, 2015) 159–177. `doi:10.1016/j.cpc.2015.01.024`, `arXiv:1410.3012`.

[42] T. Sjöstrand et al., "PYTHIA 6.4 physics and manual", *Journal of High Energy Physics* **2006** (May, 2006) 026. `doi:10.1088/1126-6708/2006/05/026`, `arXiv:hep-ph/0603175`.

[43] S. Agostinelli et al., "Geant4—a simulation toolkit", *Nuclear Instruments and Methods in Physics Research Section A: Accelerators, Spectrometers, Detectors and Associated Equipment* **506** (2003), no. 3, 250–303. `doi:https://doi.org/10.1016/S0168-9002(03)01368-8`.

[44] J. de Favereau et al., "DELPHES 3: a modular framework for fast simulation of a generic collider experiment", *Journal of High Energy Physics* **2014** (February, 2014) 57. `doi:10.1007/JHEP02(2014)057`, `arXiv:1307.6346`.

[45] T. Junk, "Confidence level computation for combining searches with small statistics", *Nuclear Instruments and Methods in Physics Research Section A: Accelerators, Spectrometers, Detectors and Associated Equipment* **434** (1999), no. 2, 435–443. `doi:https://doi.org/10.1016/S0168-9002(99)00498-2`.

[46] K. Cranmer, "Practical Statistics for the LHC", *arXiv e-prints* (March, 2015) arXiv:1503.07622. `arXiv:1503.07622`.

[47] CMS Collaboration, "Operational experience with the Silicon Strip Tracker at the CMS experiment", technical report, `http://cds.cern.ch/record/2689274`.

[48] M. French et al., "Design and results from the APV25, a deep sub-micron CMOS front-end chip for the CMS tracker", *Nuclear Instruments and Methods in Physics Research Section A: Accelerators, Spectrometers, Detectors and Associated Equipment* **466** (2001), no. 2, 359–365. `doi:https://doi.org/10.1016/S0168-9002(01)00589-7`. 4th Int. Symp. on Development and Application of Semiconductor Tracking Detectors.

[49] B. Schmidt, "The High-Luminosity upgrade of the LHC: Physics and Technology Challenges for the Accelerator and the Experiments", *Journal of Physics: Conference Series* **706** (apr, 2016) 022002. `doi:10.1088/1742-6596/706/2/022002`.

[50] W. Barletta et al., "Future hadron colliders: From physics perspectives to technology RD", *Nuclear Instruments and Methods in Physics Research Section A Accelerators Spectrometers Detectors and Associated Equipment* **764** (11, 2014) 352–368. `doi:10.1016/j.nima.2014.07.010`.

[51] G. Apollinari et al., "High Luminosity Large Hadron Collider HL-LHC". CERN, `https://cds.cern.ch/record/2120673`.

[52] H. Damerau et al., "LHC Injectors Upgrade, Technical Design Report". `http://cds.cern.ch/record/1976692`.

[53] J. Coupard et al., "LHC Injectors Upgrade, Technical Design Report", technical report, `http://cds.cern.ch/record/2153863`.

[54] H. Bartosik et al., "Performance of the LHC injector chain after the upgrade and potential development", `https://arxiv.org/abs/2203.09202`.

[55] L. Arnaudon et al., "Linac4 Technical Design Report", technical report, 2006. `https://cds.cern.ch/record/1004186`. revised version submitted on 2006-12-14 09:00:40.

[56] CMS Collaboration, "The Phase-2 Upgrade of the CMS L1 Trigger Interim Technical Design Report", technical report, `https://cds.cern.ch/record/2283192`. This is the CMS Interim TDR devoted to the upgrade of the CMS L1 trigger in view of the HL-LHC running, as approved by the LHCC.

[57] CMS Collaboration, "A MIP Timing Detector for the CMS Phase-2 Upgrade", technical report, 2019. `https://cds.cern.ch/record/2667167`.

[58] CMS Collaboration, "The Phase-2 Upgrade of the CMS Endcap Calorimeter", technical report, `https://cds.cern.ch/record/2293646`.

[59] CMS Collaboration, "The Phase-2 Upgrade of the CMS Barrel Calorimeters", technical report, 2017. `https://cds.cern.ch/record/2283187`. This is the final version, approved by the LHCC.

[60] CMS Collaboration, "The Phase-2 Upgrade of the CMS Muon Detectors", technical report, 2017. `https://cds.cern.ch/record/2283189`. This is the final version, approved by the LHCC.

[61] J. Mans et al., "CMS Technical Design Report for the Phase 1 Upgrade of the Hadron Calorimeter", technical report, 2012. `https://cds.cern.ch/record/1481837`. Additional contact persons: Jeffrey Spalding, Fermilab, spalding@cern.ch, Didier Contardo, Universite Claude Bernard-Lyon I, contardo@cern.ch.

[62] CMS Collaboration, "Upgrade of the CMS Barrel Electromagnetic Calorimeter for the High Luminosity LHC", Technical Report 3, `http://cds.cern.ch/record/2826785`.

[63] CMS Collaboration, "CMS Phase II Upgrade Scope Document", technical report, 2015. `https://cds.cern.ch/record/2055167`.

[64] S. Mersi, "Phase-2 Upgrade of the CMS Tracker", *Nuclear and Particle Physics Proceedings* **273-275** (2016) 1034–1041. `doi:https://doi.org/10.1016/j.nuclphysbps.2015.09.162`. 37th International Conference on High Energy Physics (ICHEP).

[65] J. C. Chistiansen et al., "RD Collaboration Proposal: Development of pixel readout integrated circuits for extreme rate and radiation", technical report, 2013. `http://cds.cern.ch/record/1553467`. The authors are editors on behalf of the participating institutes. the participating institutes are listed in the proposal.

[66] CMS Collaboration, "Towards Radiation Hard Sensor Materials for the CMS Tracker Upgrade", technical report, `http://cds.cern.ch/record/1494648`.

[67] CMS Collaboration, "Characterisation of silicon sensor materials and designs for the CMS Tracker Upgrade", *PoS* **Vertex2012** (2013) 016. `doi:10.22323/1.167.0016`.

[68] E. Conti et al., "Pixel chip architecture optimization based on a simplified statistical and analytical model", *JINST* **9** (2014) C03011. `doi:10.1088/1748-0221/9/03/C03011`.

[69] S. Bonacini et al., "Characterization of a commercial 65 nm CMOS technology for SLHC applications", *Journal of Instrumentation* **7** (jan, 2012) P01015. `doi:10.1088/1748-0221/7/01/P01015`.

[70] M. Bubna et al., "Testbeam and laboratory characterization of CMS 3D pixel sensors", *Journal of Instrumentation* **9** (jul, 2014) C07019–C07019. `doi:10.1088/1748-0221/9/07/c07019`.

[71] CERN, "lpGBT specification document". `https://espace.cern.ch/GBT-Project/LpGBT/Specifications/LpGbtxSpecifications.pdf/`.

[72] S. Meroli et al., "Development and prototyping of the Versatile Link + optical fibre cabling plants for the HL-LHC upgrades of the ATLAS and CMS experiments at CERN", *Journal of Instrumentation* **17** (dec, 2022) C12012. `doi:10.1088/1748-0221/17/12/C12012`.

[73] CMS Collaboration, "The Level-1 Track Finder for the CMS High-Luminosity LHC Upgrade", technical report, 2022. `https://cds.cern.ch/record/2844896`.

[74] D. Cieri et al., "An FPGA-based Track Finder for the L1 Trigger of the CMS Experiment at the HL-LHC", *PoS* **TWEPP-17** (2018) 131. `doi:10.22323/1.313.0131`.

[75] Bartz, Edward et al., "FPGA-Based Tracklet Approach to Level-1 Track Finding at CMS for the HL-LHC", *EPJ Web Conf.* **150** (2017) 00016. `doi:10.1051/epjconf/201715000016`.

[76] A. Albert et al., "The Apollo ATCA design for the CMS track finder and the pixel readout at the HL-LHC", *Journal of Instrumentation* **17** (apr, 2022) C04033. `doi:10.1088/1748-0221/17/04/C04033`.

[77] A. Ryd et al., "Tracking Triggers for the HL-LHC", *Annual Review of Nuclear and Particle Science* **70** (oct, 2020) 171–195. `doi:10.1146/annurev-nucl-020420-093547`.

[78] G. Bianchi, "tkLayout: a design tool for innovative silicon tracking detectors", *Journal of Instrumentation* **9** (mar, 2014) C03054. `doi:10.1088/1748-0221/9/03/C03054`.

[79] CERN, "Outer tracker cabling map". `https://cms-tklayout.web.cern.ch/cms-tklayout/layouts-work/recent-layouts/OT616_200_IT404/cablingOuter.html`.

[80] J. Gubbi et al., "Internet of Things (IoT): A vision, architectural elements, and future directions", *Future Generation Computer Systems* **29** (2013), no. 7, 1645–1660. `doi:https://doi.org/10.1016/j.future.2013.01.010`. Including Special sections: Cyber-enabled Distributed Computing for Ubiquitous Cloud and Network Services Cloud Computing and Scientific Applications — Big Data, Scalable Analytics, and Beyond.

[81] V. K. Pandey et al., "A Review Paper on I2C Communication Protocol", *International Journal of Advance Research, Ideas and Innovations in Technology* **4** (2018) 340–343.

[82] L. Macekova, "1-Wire - The Technology for Sensor Networks", *Acta Electrotechnica et Informatica* **12** (01, 2012). `doi:10.2478/v10198-012-0045-z`.

[83] T. pandas development team, "pandas-dev/pandas: Pandas", `https://doi.org/10.5281/zenodo.7658911`. If you use this software, please cite it as below.

[84] A. Dainese et al., "Report on the Physics at the HL-LHC, and Perspectives for the HE-LHC", technical report, `https://cds.cern.ch/record/2703572`.

[85] CMS Collaboration, "Search for nonresonant Higgs boson pair production in the WW$\gamma\gamma$ channel in pp collisions at $\sqrt{s} = 13$ TeV", technical report, 2022. `http://cds.cern.ch/record/2840773`.

[86] M. Gouzevitch et al., "A review of Higgs boson pair production", *Reviews in Physics* **5** (2020) 100039. `doi:https://doi.org/10.1016/j.revip.2020.100039`.

[87] DELPHES 3 Collaboration, "DELPHES 3, A modular framework for fast simulation of a generic collider experiment", *JHEP* **02** (2014) 057. `doi:10.1007/JHEP02(2014)057`, `arXiv:1307.6346`.

[88] P. Nason, "A New method for combining NLO QCD with shower Monte Carlo algorithms", *JHEP* **11** (2004) 040. `doi:10.1088/1126-6708/2004/11/040`, `arXiv:hep-ph/0409146`.

[89] S. Frixione et al., "Matching NLO QCD computations with Parton Shower simulations: the POWHEG method", *JHEP* **11** (2007) 070. `doi:10.1088/1126-6708/2007/11/070`, `arXiv:0709.2092`.

[90] S. Alioli et al., "A general framework for implementing NLO calculations in shower Monte Carlo programs: the POWHEG BOX", *JHEP* **06** (2010) 043. `doi:10.1007/JHEP06(2010)043`, `arXiv:1002.2581`.

[91] G. Heinrich et al., "Probing the trilinear Higgs boson coupling in di-Higgs production at NLO QCD including parton shower effects", *JHEP* **06** (2019) 066. `doi:10.1007/JHEP06(2019)066`, `arXiv:1903.08137`.

[92] T. Sjostrand et al., "An Introduction to PYTHIA 8.2", *Comput. Phys. Commun.* **191** (2015) 159. `doi:10.1016/j.cpc.2015.01.024`, `arXiv:1410.3012`.

[93] J. Alwall et al., "The automated computation of tree-level and next-to-leading order differential cross sections, and their matching to parton shower simulations", *JHEP* **07** (2014) 079. `doi:10.1007/JHEP07(2014)079`, `arXiv:1405.0301`.

[94] P. Artoisenet et al., "Automatic spin-entangled decays of heavy resonances in Monte Carlo simulations", *JHEP* **03** (2013) 015. `doi:10.1007/JHEP03(2013)015`, `arXiv:1212.3460`.

[95] R. Frederix et al., "Merging meets matching in MC@NLO", *JHEP* **12** (2012) 061. `doi:10.1007/JHEP12(2012)061`, `arXiv:1209.6215`.

[96] Sherpa Collaboration, "Event Generation with Sherpa 2.2", *SciPost Phys.* **7** (2019), no. 3, 034. `doi:10.21468/SciPostPhys.7.3.034`, `arXiv:1905.09127`.

[97] CMS Collaboration, "Performance of the DeepJet b tagging algorithm using 41.9/fb of data from proton-proton collisions at 13TeV with Phase 1 CMS detector", Technical Report CMS-DP-2018-058, Nov, 2018. `https://cds.cern.ch/record/2646773`.

[98] E. Bols et al., "Jet Flavour Classification Using DeepJet", *JINST* **15** (2020), no. 12, P12012. `doi:10.1088/1748-0221/15/12/P12012`, `arXiv:2008.10519`.

[99] A. Dainese et al., "Report on the Physics at the HL-LHC, and Perspectives for the HE-LHC", technical report, `https://cds.cern.ch/record/2703572`.

[100] The ATLAS Collaboration, The CMS Collaboration, The LHC Higgs Combination Group Collaboration, "Procedure for the LHC Higgs boson search combination in Summer 2011", technical report, Aug, 2011. `https://cds.cern.ch/record/1379837`.